



Characterising CE-65 monolithic sensors towards FCC-ee vertex detectors

Master Thesis

Supervised by

Dr. Armin Ilg

Dr. Anna Macchiolo

Prof. Dr. Florencia Canelli

Alessandra Lorenzetti

June 2025

Acknowledgements

I want to thank Armin Ilg, Anna Macchiolo and Florencia Canelli from the University of Zurich for navigating my academic journey throughout this last year. I am deeply grateful for your unwavering patience, support and your invaluable wisdom, which I could count on in every situation. Thank you very much for making this journey not only possible but also instructive and enjoyable.

To my beloved family and friends, your constant support and belief in me were the cornerstone of this master thesis. I thank you all for making it so easy for me to present my work to you by getting up and being motivated listeners on the 5th of June. I would like to express special thanks to my grandma, who travelled a long way to listen to a presentation in a language she does not even speak.

Contents

Acknowledgements	iii
Introduction	1
1 The Standard Model of particle physics	3
1.1 Electroweak unification	4
1.2 CKM matrix	5
1.3 Colliders	5
1.4 Hadron versus lepton colliders	6
1.5 Particles generated in collisions	7
1.6 Particle physics in 2040 and beyond	8
2 The Future Circular Collider project	13
2.1 The two phases of FCC	13
2.2 FCC in numbers	13
2.3 What distinguishes the FCC-ee?	14
2.4 Detector concepts for FCC-ee	15
3 Tracking and vertexing	19
3.1 Interaction and detection of charged particles with matter	19
3.2 Introduction to vertexing and parameters	25
4 Monolithic active pixel sensors and the CE-65 prototype chip	31
4.1 CMOS technology	31
4.2 ALPIDE sensors	34
4.3 ALICE ITS3	35
4.4 The CE-65 v2 prototype chip	38
5 Lab measurements	41
5.1 Setup	41
5.2 Method	42
5.3 Results	44
5.3.1 Global spectrum measurements	44
5.3.2 Comparison of calibration factors	45
5.3.3 K-beta peak fitting	47
6 Test beam measurements	53
6.1 Setup	53
6.2 Collected datasets	55
6.3 Analysis	56
6.4 Results	59

6.4.1	Global efficiency and spatial resolution	60
6.4.2	In-pixel efficiency and spatial resolution	64
6.5	Summary	68
Conclusions		71
Appendix		81

Introduction

The beginning of particle physics can be traced back to 1895 when, in a cathode ray tube experiment, Röntgen accidentally discovered X-rays. Since then, many new particles have been discovered, some before and others after they were theoretically explained. In the 1960s, with the development of the first accelerator machines accelerating particles to probe higher energies, many new particles were found in a short time, and physicists sought to bring order to this “particle zoo”, as this mass of new particles and the resulting difficulties in finding their inner structure, was called. A theoretical model was required to organise the mass of composite particles found with these first accelerators. This model includes the fundamental building blocks of hadrons (quarks) and became the Standard Model (SM) of particle physics. It is one of the most precise and, at the same time, elegant theoretical descriptions. It includes only two different kinds of particles - fermions, of which matter consists, and bosons, the fundamental force carrier particles - and explains three of the four fundamental forces: The weak force, the strong force and the electromagnetic force, only leaving out the gravitational force. The SM was completed in 2012 by the experimental finding of the last of its predicted particles, the Higgs boson, at the Large Hadron Collider (LHC) at CERN [1, 2].

The fermions in the SM are grouped into three “generations” of particles, which are physically similar, although the particles differ in their masses. In this context, the SM’s first unanswered question can be posed: why are there three generations and not four or two? Furthermore, the Higgs field gives mass to the massive particles of the SM through the Higgs mechanism. But why are the masses as they are? Why is the coupling of the Higgs particle different for each particle? Might the Higgs particle be composite?

For these and many more open questions concerning the newest particle, it is important to do further precision measurements on the Higgs boson and trace the limits of the SM. Especially for these measurements, it is necessary to probe the fundamental laws of nature using higher energies and greater precision. Thus, the particle physics community is evaluating different concepts for the successor of the LHC, aiming to push the energy and intensity frontier. The most prominent successor of the LHC is the proposed Future Circular Collider (FCC). In its first phase, the FCC-ee will accelerate electrons and their antiparticles, the positrons, and collide them to produce very clean collisions for precision measurements of the properties of the SM. It is designed to enable such precision measurements in connection with, for example, the Higgs boson, the top quark, the electroweak sector, and flavour physics. Especially for flavour physics at the Z pole, it will be important to have an

excellent reconstruction of the primary, secondary and tertiary vertices, as hadrons containing heavy quarks typically have short lifetimes and need to be reconstructed for these measurements. A precise vertex reconstruction necessitates high-precision, light inner tracking layers; the vertex detector. The investigation of this detector and its sensor candidates with regard to the FCC-ee requirements is the central point of this thesis. In the scope of this work, sensor prototypes are characterised following the requirements of vertex detectors at future electron-positron colliders like the FCC-ee. This includes the question of whether a resolution of $3\text{ }\mu\text{m}$ can be reached in 65 nm CMOS Imaging Process (CIS) technology. This characterisation aims to compare different chip variants to guide the development of the next generation of sensors that eventually would instrument FCC-ee vertex detectors.

This work consists of six chapters: Firstly, the reader is equipped with the underlying physics motivation for future collider experiments. This includes an overview of the SM, a discussion of its open questions, and an introduction to the FCC and its physics programme, especially of the FCC-ee. Next, an outline of the techniques used in the innermost detector layers, tracking and vertexing, is given, before the historical and technological evolution of Monolithic Active Pixel Sensors (MAPS) is discussed. This chapter also includes an introduction to the CE-65 prototype structure, its technical specifications and the motivation for its characterisation in this thesis. The following chapters discuss the experiments and analyses done to characterise the sensors, and the results are presented. The thesis then closes with conclusions and provides an outlook on the future of MAPS for FCC-ee vertex detectors.

Chapter 1

The Standard Model of particle physics

Humanity has long been pursuing the philosophy that the whole Universe, including all matter, could probably be described by only a small number of indivisible components. In ancient Greece, the earliest concept of “atomos” (indivisible) particles was debated philosophically. This theory was followed thoroughly throughout the evolution of science in the strong belief that one day, humanity could find proof for it. Since then, the fundamental building blocks of the Universe were suspected to have been found some times before, among others, the word “atom” is derived from “atomos”. Likewise, the fascination with the laws that govern the motion and interaction of matter has a long history. Researchers investigated different forces on Earth and beyond to shed light on one of the biggest questions we can pose: *What is the Universe made of, and which laws govern the way nature evolves?*

These endeavours to find the fundamental building blocks are now gathered together in the Standard Model of particle physics (SM), whose structure is represented in Figure 1.1.

The SM is grouping the particles into two different kinds: the fermions (matter particles), which are divided again into quarks and leptons, and the bosons (force carrier particles). According to the SM, all matter consists of these twelve particles and their corresponding antiparticles. They interact by exchanging force carrier particles, corresponding to one of the three forces present in the SM; the gluon corresponding to the strong force, the photon to the electromagnetic force and the W and Z bosons to the weak force.

While the theory was developed in the early 1970s [4–13], the experimental proof of the last particle, predicted by the SM, was only found in 2012. Then, the ATLAS and CMS collaborations at CERN announced the finding of the last predicted particle of the SM, the Higgs boson [1, 2]. The Higgs boson is the quantum excitation of the Higgs field that gives mass to other SM particles via the Yukawa coupling and spontaneous symmetry breaking [14]. Apart from whether the Higgs is composite and the differences in coupling of the Higgs field to the quarks and charged leptons, there are more open questions concerning the newest fundamental particle. Precision measurements and very high collision energies would be needed to answer the questions regarding the Higgs boson and the SM at large.

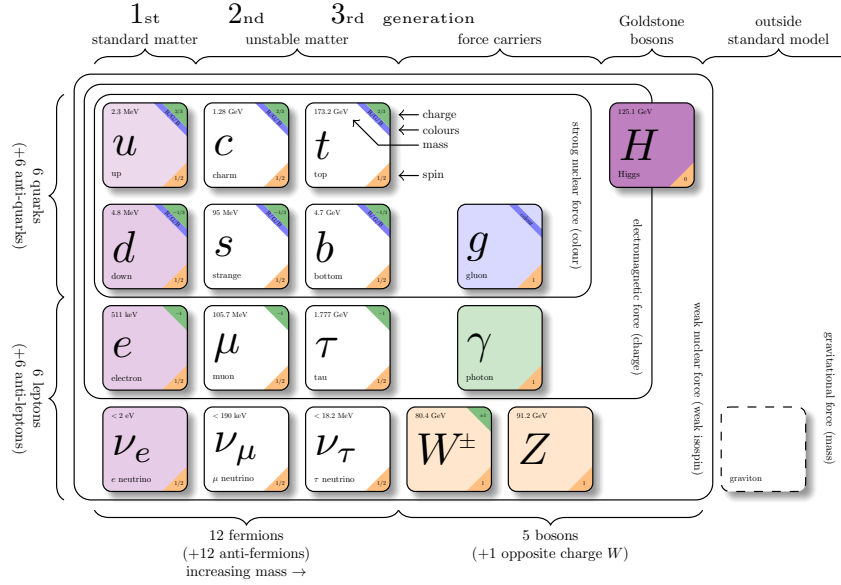


Figure 1.1: The Standard Model of particle physics, including all known and experimentally observed elementary particles divided into fermions (leptons and quarks) on the left-hand side, Gauge bosons in the middle and the Higgs boson on the right-hand side. From Reference [3].

In the following, specific topics where further progress in HEP is needed are picked out and explained in more detail. Thereafter, colliders are introduced generally, and a comparison between hadron and lepton colliders is made. At the end of this chapter, the current status of research on these open questions is summarised.

1.1 Electroweak unification

Another effect the SM describes is the electroweak unification. At the energy scale corresponding to the mass of the vector bosons W and Z (~ 100 GeV) [14], the electromagnetic and the weak interactions unify and are described by the electroweak interaction [6]. In this unification, the electromagnetic and neutral currents corresponding to these two interactions act as a superposition and are mathematically described by a combined Lagrangian. The observables, sensitive to electroweak corrections, need to be predicted more and more precisely as the experiments measuring them get better and better. If a measurement showed a deviating result from the theoretical predictions, it would hint towards the existence of new, weakly interacting particles at higher scales. Precision measurements on these electroweak observables, like the W and Z boson masses and decay widths, are thus an essential tool for constraining theories describing physics beyond the SM. [15]

1.2 CKM matrix

Another example of a precision measurement is the study of the Cabibbo-Kobayashi-Maskawa [16, 17] matrix parameters. According to the SM, quarks can be ordered in three flavour doublets of an up- and a down-type quark. The structure of the electroweak charged current interactions, involving the W^+ and W^- bosons, allows only transitions within the doublet, but no transitions between families are permitted. This would, however, imply that the lightest particle of each doublet should be stable since the strong and electromagnetic interactions do not carry flavour quantum numbers and can, therefore, not mediate flavour-changing processes. What we observe contradicts this assumption, as the Universe is almost exclusively composed of particles of the first family and not only of the lightest particle per family. Correspondingly, the interfamilial mixing probability of quarks can not be zero. It can be described by assuming that the quarks, when interacting weakly, are in their weak eigenstates, which are combinations of their observable eigenstates. Mathematically, these mixed states are linear combinations of the mass eigenstates we observe when particles travel. With this assumption, the observed phenomenology can be reproduced. The weak isospin doublets would then look like this:

$$\begin{pmatrix} u \\ d' \end{pmatrix} \quad \begin{pmatrix} c \\ s' \end{pmatrix} \quad \begin{pmatrix} t \\ b' \end{pmatrix} \quad (1.1)$$

Where $|d'\rangle$ is assumed to be a linear combination of the mass eigenstates $|d\rangle$, $|s\rangle$ and $|b\rangle$. The connection between the three families can be described by introducing mixing angles and a complex phase, which can be seen as rotations in flavour space. The matrix describing these rotations has to be a unitary 3×3 matrix acting on the mass states:

$$\begin{pmatrix} d' \\ s' \\ b' \end{pmatrix} = \begin{bmatrix} V_{ud} & V_{us} & V_{ub} \\ V_{cd} & V_{cs} & V_{cb} \\ V_{td} & V_{ts} & V_{tb} \end{bmatrix} \begin{pmatrix} d \\ s \\ b \end{pmatrix}. \quad (1.2)$$

This matrix, the CKM matrix, is the connection between the mass eigenstates and the flavour eigenstates. With dedicated precision measurements, its parameters could further be characterised to discover more about CP violation and, hence, about the striking imbalance between matter and antimatter in our Universe. [14, 18–20].

1.3 Colliders

The precision with which we know the Higgs boson couplings and, hence, can understand the mechanisms leading charged fermions to have mass, is constrained by high-energy collider experiments. In a collider, charged particles are accelerated before colliding at specific interaction points (IP). Around these interaction points (IPs) are experiments in which the particles resulting from the collisions are observed. For example, the LHC at CERN hosts four experiments along its nearly 27 km long ring [21]. It is a hadron-hadron collider using particles accelerated to nearly the speed of light.

In a collider, the energy in the centre of mass frame defines the experiments which are possible to conduct. This energy, given by the square root of the Lorentz invariant quantity s , is greater than the sum of the masses of the particles being produced. In natural units with $c = 1$, it is given by

$$\sqrt{s} = \sqrt{\left(\sum_i E_i\right)^2 - \left(\sum_i \mathbf{p}_i\right)^2}, \quad (1.3)$$

where E_i is the initial energy and \mathbf{p}_i is the initial momentum of the collided particle in three dimensions. For a collision of two particles inside a collider, the energy is typically high, leading the mass of the particles to be negligible. In this case, the centre of mass energy simplifies to $\sqrt{s} = E_1 + E_2$, which in the case of the LHC corresponds to 6.799 TeV for the two stable beams and a centre of mass energy of $\sqrt{s} = 13.598$ TeV. [22]

The lifetime of a particle is given by the inverse of its transition rate, which is the probability per unit time that the particle will decay. Fermi's golden rule states that the decay rate depends on the transition matrix element, $|M_{fi}|^2$, giving the transition probabilities between different quantum states and the density of kinematically accessible final states for the decay.

The luminosity is given by the ratio of the number of particles produced, dN , in a certain period of time, dt , to the cross section, σ , which is a measure of the probability that a specific process will take place in an interaction of two particles. It is given by

$$L = \frac{1}{\sigma} \frac{dN}{dt}. \quad (1.4)$$

In non-relativistic quantum mechanics, the transition rates of decaying particles are obtained using Fermi's golden rule, which is the transition rate Γ_{fi} from an initial state $\langle i|$ to a final state $\langle f|$. It is usually expressed as

$$\Gamma_{fi} = 2\pi |T_{fi}|^2 \rho(E_i), \quad (1.5)$$

where T_{fi} is the transition matrix element and $\rho(E_i)$ is the density of states. If a process is rare, its cross-section, σ , given by the matrix element, T_{fi} , is small. As the luminosity is inversely proportional to the cross section, processes that happen rarely can be measured more precisely with a high luminosity.

1.4 Hadron versus lepton colliders

The LHC is a powerful machine in high-energy particle physics research, very well suited to probe high energies and potentially discover new particles. It was constructed for the purpose of discovering the Higgs boson and for the study of rare events at high energies [21]. However, precision measurements are difficult to perform at the LHC because it is a hadron collider. Hadrons are composite particles consisting of two or more quarks. When they interact, various effects have to be

accounted for.

Due to the nature of hadron collisions at the LHC, the most interesting processes are buried under a large background of well-understood, uninteresting processes. Another unwanted effect comes from the fact that quarks evolve in groups, connected by gluons. The further they are away from each other, the stronger the force between them pulls them back together, as the particles mediating the strong force between the quarks, the gluons, interact with each other. This feature is called confinement and makes it more challenging to study, for example, effects where the quark flavour is a relevant quantity. Due to confinement, in a proton-proton collider like the LHC, it is unclear which of the partons (quarks or gluons) inside the proton interacts with which of the partons of the other proton, and the momentum carried by the partons is also unknown. If either has to be known, calculations are done using so-called parton distribution functions (PDFs). These give the probability of the interacting parton (whichever this might have been) to have carried a momentum fraction of the total momentum of the hadron at this moment [14]. Using PDFs is highly impractical for precise calculations, as it increases the resulting uncertainties due to not knowing the parameters of the interactions precisely. Luckily, there is an easy solution to this problem: don't accelerate composite particles, but elementary particles like, for example, electrons and/or positrons. However, other challenges arise for highly energetic electrons in a circular collider. One difficulty encountered when accelerating electrons along a curved path is that the electrons can lose a significant fraction of their energy via bremsstrahlung. To minimise bremsstrahlung, a circular collider has to have a large radius, such that the trajectories of the particles have to be bent as little as possible.

Generally, in an e^+e^- collider, the systematic uncertainty and the number of particles are reduced compared to a hadron-hadron collider. Having fewer particles in general and less total energy coming out per bunch collision also reduces radiation levels. All of this contributes to having cleaner and, hence, better analysable data samples in an e^+e^- collider. [23]

1.5 Particles generated in collisions

Not all the particles produced in colliders are stable, so many are not detectable: Only the electron, the proton, their antiparticles and the photon are stable *and* detectable in standard detectors. For specialised searches, detectors can be extended by instruments designed to detect the fourth stable particle, the neutrino. Some unstable particles are detectable, as these particles travel long enough distances to reach the detector before decaying. The distance travelled is of order $\gamma v \tau$, where τ is the mean lifetime in the rest frame of the particle, v is its possibly relativistic velocity, and $\gamma = 1/\sqrt{1 - v^2/c^2}$ is the Lorentz factor, which accounts for the relativistic time dilation. Unstable particles with a rest frame lifetime of approximately 10^{-10} s or more will, therefore, propagate several meters before decaying. In this case, detecting them directly in the detector should be possible if they are produced at high enough energies. These relatively long-lived particles usually decay mainly via the weak

force. This includes the muon, decaying to the electron in a leptonic weak decay, conserving the lepton number by including the corresponding neutrinos, which only couple to the weak force ($\mu \rightarrow e^+ + \bar{\nu}_\mu + \nu_e$). For unstable particles, which can not be directly detected, the decay products are observed. These short-lived particles include heavy fermions, like B and C hadrons, which have lifetimes of $\mathcal{O}(\text{ps})$ and thus travel $\mathcal{O}(50 \mu\text{m})$. But also the Higgs boson, the gluon, and the W and Z bosons, can not be observed directly. The tracks of the final state particles have to be measured with very high resolution to see that they came from a secondary vertex, which is sometimes only a few μm beside the collision vertex.

1.6 Particle physics in 2040 and beyond

The experiments, which have already started or will start data taking now and run until the 2040s, can not answer all the open questions introduced in this chapter. Some parameters are essential to be measured with more statistics, using higher energy or in different channels to reduce uncertainties. For example, the Higgs boson coupling constants to SM particles are expected to be measured to the uncertainties shown in Figure 1.2 until the 2040s. These uncertainties could be improved significantly by using measurements from a high-energy electron-positron collider, like the FCC-ee (see next chapter). In Table 1.1, the expected relative uncertainties at 68% CL of the κ coupling constants, denoting the Higgs boson coupling strength to other SM particles, are shown. Here, a comparison is made between the expected uncertainties of the HL-LHC measurements and the FCC-ee measurements. Particularly for the measurements which can not be done at HL-LHC, the results gained at FCC are vital. But also, measurements like the κ_Z , which can be improved by a factor of 13, can provide valuable new insights into the SM. [23]

Using an electron-positron collider, the top quark's mass can be more accurately determined than with a hadron collider. This measurement is in various ways important for predicting electroweak precise observables (EWPO), like the width of the W and Z bosons, $\Gamma_{W/Z}$. Only if the top mass is measured with the highest possible precision, the FCC-ee EWPO measurements give their best sensitivity. Shown in Table 1.2 are some examples of electroweak parameters, which would benefit from a precisely measured top mass. [23]

For flavour studies, a high-energy lepton collider is very well suited. The pileup, which makes measurements in a hadron collider more complicated, is negligible, and the high energies allow studies of heavy quarks and their couplings. Today's research on one of the heavy quark couplings, $|V_{ts}|$, can only be made by studying loop diagrams. It is determined in studies of the $B_s^0 - \bar{B}_s^0$ mixing and is mediated via t-W box diagrams shown in Figure 1.3.

Due to pileup effects and the nature of hadron collisions, flavour tagging is generally very difficult at a hadron collider. For a precision measurement of the CKM parameter $|V_{ts}|$, a collider like the FCC-ee is desired, where this parameter could be measured with comparable precision but model independently. [27, 28]

Another example of a study, which is limited by today's collider performance,

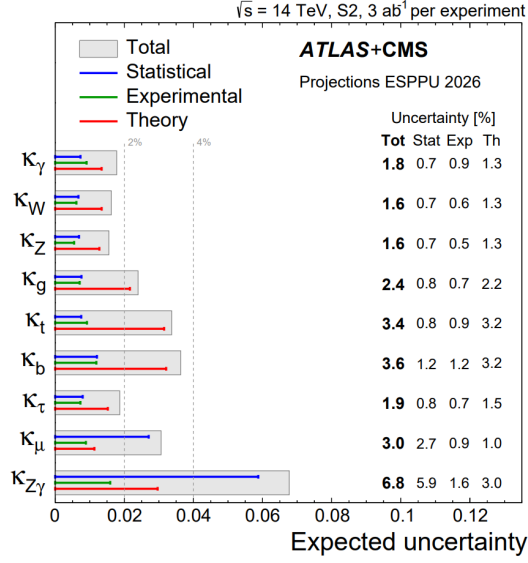


Figure 1.2: Expected coupling constant uncertainty after HL-LHC measurements of Higgs boson to SM particles, assuming that the Higgs boson decays only to final states predicted by the SM. From Reference [24].

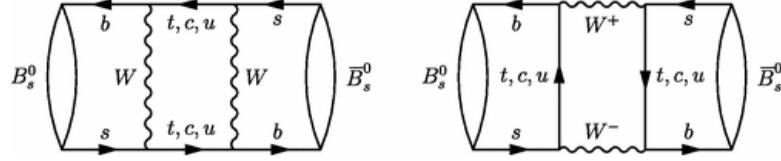


Figure 1.3: Box diagrams of B_s^0 mixing. This channel is used to measure the CKM parameter $|V_{ts}|$, assuming no new physics in the loop. From Reference [26].

is the unitarity triangle. The unitarity triangle is a graphical representation of the parameters of the CKM matrix. Requiring the matrix to be unitary, a SM assumption, constrains the individual parameters. The triangle representation emphasises the dependencies of the different parameters on one another. In such a graphical representation, the state of the art of CKM parameter measurements can be displayed, as shown in Figure 1.4a. After the Belle II and the upgraded LHCb runs are fully analysed, the research landscape will change, as especially $|V_{ub}|$ can be measured to higher precision. For further information on the measurements of Belle II and LHCb on the CKM matrix, see [29–31].

Using the FCC-ee, the physics landscape could change drastically. Precision measurements of the heavy quarks make it possible to determine parameters like $|V_{ub}|$ to an uncertainty of $\mathcal{O}(\%)$. For an overview of the improvement in two measurements today and after FCC-ee, see Figure 1.4

The FCC-ee would be an ideal candidate for studying the unsolved questions outlined in this chapter in an optimal setting. As a high-energy electron-positron collider, it can study SM parameters to much greater detail and follow new physics

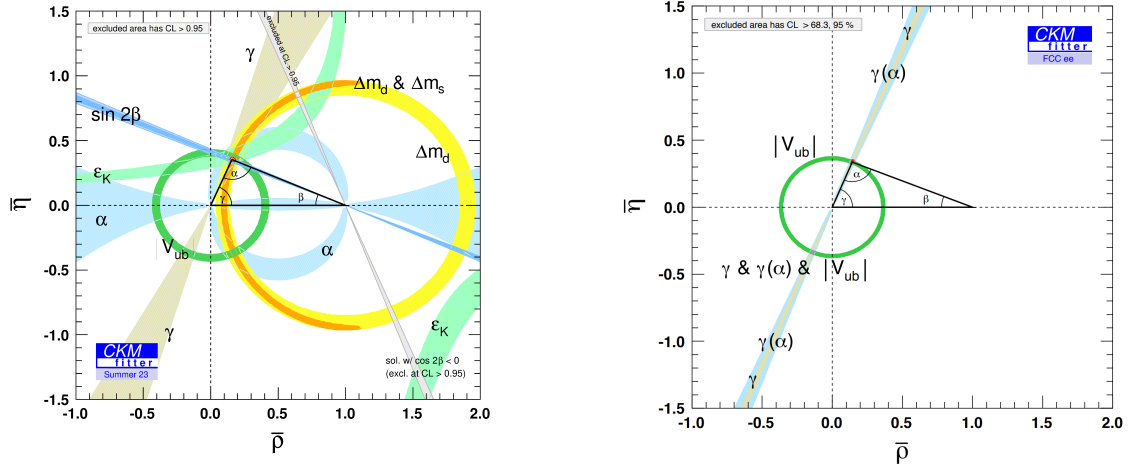
Coupling (%)	HL-LHC	FCC-ee
κ_Z	1.3	0.10
κ_W	1.5	0.29
κ_b	2.5	0.38/0.49
κ_g	2	0.49/0.54
κ_τ	1.6	0.46
κ_c	-	0.70/0.87
κ_γ	1.6	1.1
$\kappa_{Z\gamma}$	10	4.3
κ_t	3.2	3.1
κ_μ	4.4	3.3
$ \kappa_s $	-	+29 -67
Γ_H	-	0.78

Table 1.1: Expected relative precision of the κ parameters (Higgs couplings to SM) evaluated at 68% CL and of the Higgs boson total decay width Γ_H . Comparison between uncertainties as expected to be measured at HL-LHC and FCC-ee. For some of the entries, the κ precision starts being limited by the projected SM parametric uncertainties. For these entries, the precision obtained by neglecting such parametric uncertainties is also reported (separated by a /). From Reference [23].

hints wherever they lead. In the following chapter, this project is further introduced, showing a preliminary run plan, as well as a description of how experiments at FCC-ee could look like.

Observable	value	present	uncertainty	FCC-ee Stat. UC	FCC-ee Syst. UC
m_Z (keV)	91 187 600	\pm	2 000	4	100
Γ_Z (keV)	2 495 500	\pm	2 300	4	12
m_W (MeV)	80 360.2	\pm	9.9	0.18	0.16
Γ_W (MeV)	2 085	\pm	42	0.27	0.2

Table 1.2: Comparison of a selection of observables connected to EWK precision measurements. The *present* world-average precision value is taken from Reference [25], the experimental systematic uncertainty (UC) value at FCC-ee was determined in the scope of the feasibility studies for the FCC-ee in Reference [23]. The goal is to improve the systematic UC further to match the statistical UC.



(a) State of the art CKM matrix triangle. From Reference [32].

(b) Expected unitarity triangle after FCC-ee. From Reference [33].

Figure 1.4: Comparison between the unitarity triangle now and after FCC-ee.

Chapter 2

The Future Circular Collider project

The future of experimental particle physics after the discovery of the last proposed particle lies in precision measurements. In 2020, the European Strategy for Particle Physics Update recommended building a machine that is best suited to do precision measurements on the Higgs boson as first priority [23]. For this Higgs factory, different accelerator concepts are proposed. One of them is the International Linear Collider (ILC), which is based on mature technology and therefore contains the lowest risk. It consists of two linear accelerators of approximately 11 km length [34]. Another proposed accelerator is the Compact Linear Collider (CLIC). CLIC is an e^+e^- collider operated in centre-of-mass energy stages from a few hundred GeV up to a few TeV [35, 36]. However, the only collider, which also includes a hadron-colliding phase, is the Future Circular Collider (FCC), which will in this section be discussed in detail [23, 37].

2.1 The two phases of FCC

The FCC is planned to consist of two main phases. The first phase, FCC-ee, would start data-taking in the mid-2040s and should run for approximately 15 years. The second phase, FCC-hh, is planned to succeed FCC-ee and start taking data around 2070 (FCC [38]). First, it was considered to create a high-luminosity machine inside the tunnel that is now used by the LHC. However, to be a Higgs Factory, the collider has to be operated at very high centre-of-mass energies, for which it is much more convenient to have a smaller curvature. Therefore, the FCC-ee is chosen to be built in a new tunnel with a circumference of 90.7 km, which could subsequently be used to host also the FCC-hh (see Figure 2.1 for a comparison in size between the LHC tunnel and the planned FCC tunnel).

2.2 FCC in numbers

The FCC-ee is intended to reach successively different centre-of-mass energies, ranging between $\sqrt{s} \sim 88$ GeV and 365 GeV. This energy range includes e^+e^- collision centre-of-mass energies around the Z pole, the WW threshold, the ZH production

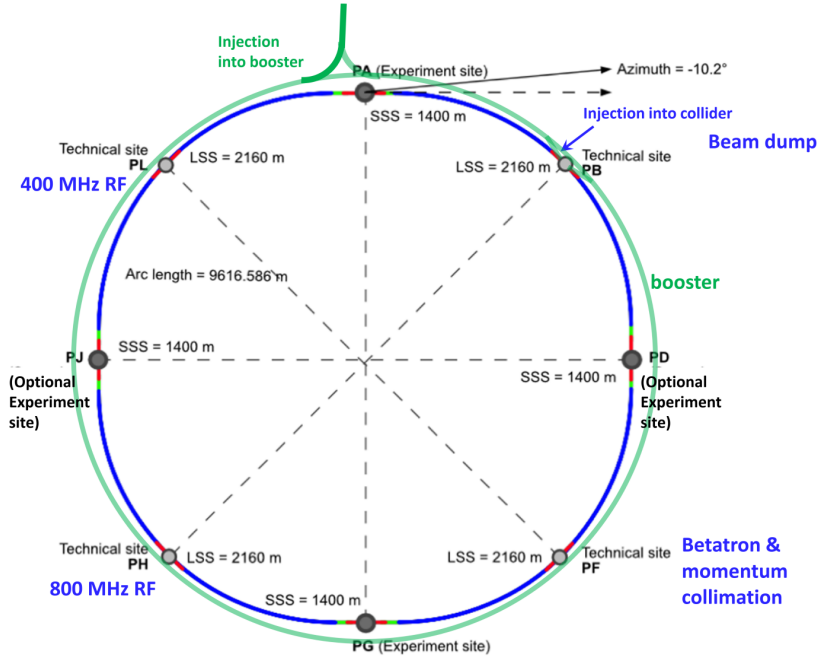


Figure 2.1: Schematic representation of the FCC with 4 IPs and its booster. From Reference [39].

maximum, up to the $t\bar{t}$ threshold and just above. Examples of which measurements could be taken at these energies include the masses and decay widths of three of the heaviest particles in the SM at their respective production energies: the Z boson at the Z-pole, the W boson at the WW threshold and the top quark at the $t\bar{t}$ threshold. Moreover, as a Higgs factory, the FCC-ee has many advantages, especially when running at the ZH production maximum. At this energy, the measurement of the Higgs coupling constant to the Z boson can be determined precisely and model independently. The absolute measurement can later be used as crucial input to Higgs self-coupling measurements, including those at hadron or muon colliders.

The FCC-ee will feature four IPs, for which the currently expected luminosity values at the energies mentioned above are shown in Figure 2.2.

For an example of how the integrated luminosities of the FCC-ee could be chronologically ordered, see Figure 2.3, where the integrated luminosities for each run are shown. The hatched area stands for a long shutdown time, needed for the preparation of the runs at the $t\bar{t}$ threshold. Note, however, that the currently intended overall sequence of the centre of mass energies and the duration of each step will be changed and adjusted in the coming years. [23, 40]

2.3 What distinguishes the FCC-ee?

Initially, the idea for the successor of the LHC at CERN was to create a high-luminosity e^+e^- circular collider, Higgs Factory, inside the LEP/LHC tunnel. This

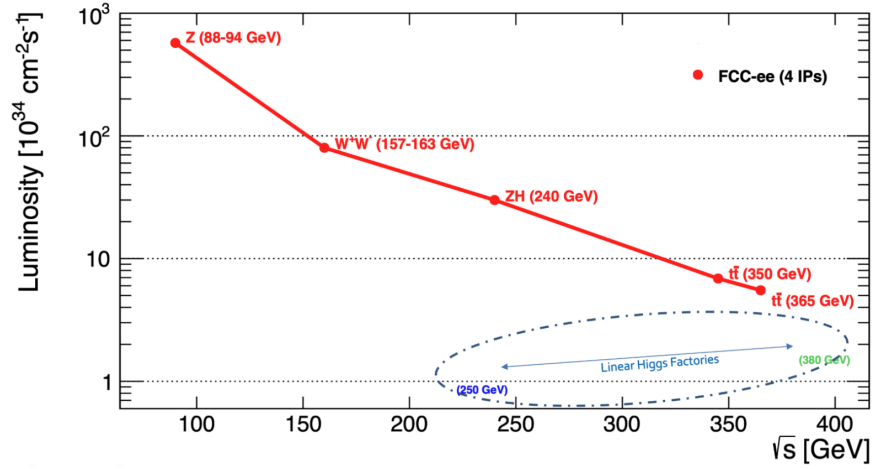


Figure 2.2: Currently expected luminosity values at FCC-ee at the centre of mass energies around the Z pole, the WW threshold, the ZH production maximum and up to the $t\bar{t}$ threshold and above. For comparison, the luminosity typically achievable by linear collider Higgs factories is indicated in the dash-dotted oval. It holds for linear colliders with one IP in their design and between 250 and 380 GeV centre-of-mass energy. From Reference [23].

collider would have been planned to operate at $\sqrt{s} = 240$ GeV. The advantage of choosing a 90.7 km circumferenced ring instead, which would also be hosting the second phase of the FCC, the FCC-hh, was an important decision to make the FCC-ee unique among the Higgs factory plans worldwide. The larger ring size enables, for the first time in e^+e^- collisions, measurements at the $t\bar{t}$ threshold and beyond, essential for the overall FCC electroweak and Higgs precision physics programme. Moreover, the construction of an external second tunnel reduces the time gap between HL-LHC and the next collider and enables higher instantaneous luminosity than having LEP3 in the LEP/LHC tunnel. In the 15 years, the FCC-ee is planned to be operated, 2×10^6 top pairs are expected to be collected, making the FCC-ee the top factory project with the highest luminosity proposed to date [23].

2.4 Detector concepts for FCC-ee

In a particle detector at a collider, the particles' trajectories are usually traced using different layers of detectors, which are traversed by particles from the collisions. The signal that particles leave in the sensors in the single detector layers is then extrapolated to form traces of particles, so-called tracks. If a particle track is observed to decay inside the detector, the point to which the decay products can be traced back, to the decay point, the vertex. In a particle physics detector, the innermost detector part is usually a vertex detector, designed to reconstruct vertices as precisely as possible from the data taken in these detector parts.

Generally, complete coverage, such that no particle escapes undetected, and the

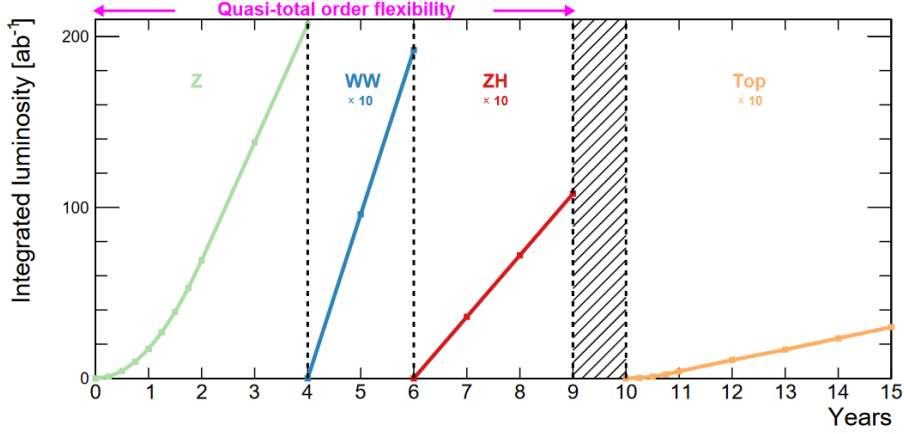


Figure 2.3: Baseline operation model for FCC-ee. Assuming four interaction points, this figure shows the integrated luminosity at the Z-pole (green), the WW production energy (blue), the ZH threshold (red) and the top-pair production threshold (sand) as a function of time. From Reference [23].

smallest possible inner radius, helping to ensure an exquisite vertex resolution, are desired in a detector. Additionally, to improve, for example, the momentum resolution of the particles in the calorimeters, an effective and lightweight vertex detector is required, which ideally can be air-cooled and does not use heavy supporting material. [19, 20]

Four experimental interaction points are planned for the FCC-ee, hosting four unique, general-purpose experiments [40]. So far, there are four proposed detector concepts: (i) IDEA [41], (ii) ALLEGRO [42], (iii) CLD [43], which is a detector concept originating from the Compact Linear Collider (CLIC) [36], and (iv) ILD@FCC-ee [44], a detector concept which is adapted from the International Linear Collider (ILC) [34]. IDEA is a detector featuring a light drift chamber tracking system surrounded by a silicon tracking layer, a solenoid outside the tracker or the ECAL, an ECAL and HCAL system, and an outer muon detector system. CLD features a silicon pixel vertex detector and a silicon tracker, followed by high-granularity calorimeters (ECAL and HCAL). A superconducting solenoid follows the calorimeters, and a steel yoke interleaved with muon chambers closes the field. The special feature of ALLEGRO is its noble-liquid ECAL, which surrounds the tracker. It could be made of lead (or tungsten) and liquid argon or, alternatively, of tungsten and liquid krypton. It would be encapsulated by a solenoid, separating the ECAL from the HCAL. The outermost layer is, as usual, the muon system. The ILD detector concept has a very similar structure to the CLD but uses a time projection chamber. [23]

Currently, only two FCC-ee vertex detector concepts exist. The sensors must perform exceptionally well for both inner vertex detector designs to ensure the best possible vertex reconstruction. The only technology considered for FCC-ee vertex detector sensors are Monolithic Active Pixel Sensors (MAPS). There is still much R&D necessary towards the FCC-ee vertex detectors. This thesis is a part of the ongoing studies to characterise MAPS for a potential use at FCC-ee vertex detectors.

In the following chapter, vertex detectors are discussed in detail, outlining how they work and what parameters influence their performance, before a detailed overview of the development of MAPS themselves is given in Chapter 4. [[23](#), [45](#), [46](#)]

Chapter 3

Tracking and vertexing

The experiments, located at a particle collider, are designed to detect and, if possible, identify the known particles produced in these collisions. The experiments are optimised to detect and track particles as precisely as possible using different subdetectors and specifically developed components. These subdetectors are generally based on a few fundamental concepts of the interaction of particles with matter, which are introduced in the following.

3.1 Interaction and detection of charged particles with matter

The innermost layers of a typical particle detector, the vertex detector, are primarily used for the precise reconstruction of charged particle tracks. In general, the techniques employed to detect and identify various particles in collider experiments are based on the specific ways in which these particles interact with matter. Three fundamental types of interactions are typically distinguished and will be discussed in the following: interactions of charged particles in general, electromagnetic interactions involving electrons and photons, and strong interactions of both charged and neutral hadrons.^[47]

Ionisation The Bethe-Bloch equation describes the mean energy loss per unit distance of a charged particle as it traverses matter, primarily due to ionisation of the atoms in the medium. At low velocities, the energy loss increases approximately as $(1/\beta^2)$, where $(\beta = v/c)$, meaning slower particles lose more energy. However, in high-energy physics, particles are typically highly relativistic, with $(\beta \approx 1)$. In this regime, the energy loss reaches a minimum and then gradually increases due to a logarithmic dependence on the relativistic factor $(\beta\gamma)$, where $(\gamma = 1/\sqrt{1 - \beta^2})$. This so-called relativistic rise in ionisation energy loss is a characteristic feature of the Bethe-Bloch formula and is illustrated in Figure 3.1.

Particles entering the material at a momentum corresponding to $\beta\gamma \approx 3$ (the minima of the curves) are referred to as minimum ionising particles.

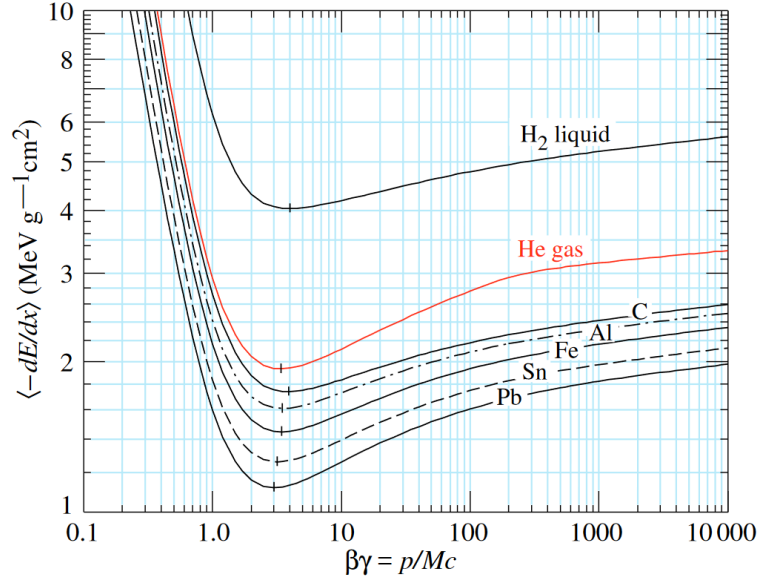


Figure 3.1: Ionisation energy loss curves for a charged particle with momentum/mass ratio normalised by the speed of light. The different curves show the particle’s energy loss in different materials. Note the steep fall of the ionisation energy for low-momentum particles, which ends at a minimum before rising again. From Reference [48].

Although other energy-loss processes also play a role for some particles, all charged particles leave ionisation traces, trails of ionised atoms and ionisation electrons in the medium they propagate. For muons with energies below 100 GeV, ionisation is the dominant process; this is why muons can travel significant distances even through very dense materials. As this is a special feature no other charged particle has, the muons produced in particle accelerator collisions are usually very penetrating. They can be detected and identified even after several meters of solid detector material. This property is used to identify muons in particle detectors; the muon system usually belongs to the outermost detector parts, which only muons and neutrinos can reach. As neutrinos can’t easily be detected, the muons, which have penetrated all the foregoing detector material, are identified by their presence alone. This is why muon systems usually form the outermost detector parts, for example, Figure 3.4. For an overview of how the energy of a muon is lost in copper (Mass stopping power), see Figure 3.2. [47]

Bremsstrahlung For electrons, the energy loss when traversing matter is dominated by ionisation only at low energies. The ionisation loss rates rise logarithmically with energy. Above a critical value, the energy loss is not described by the Bethe-Bloch curve any more but by a radiative effect called bremsstrahlung. In this process, the electron radiates a photon in the electrostatic field of a nucleus. Any charged particle can be affected by bremsstrahlung, but the intensity is inversely proportional to the square of the particle’s mass. Consequently, it happens more

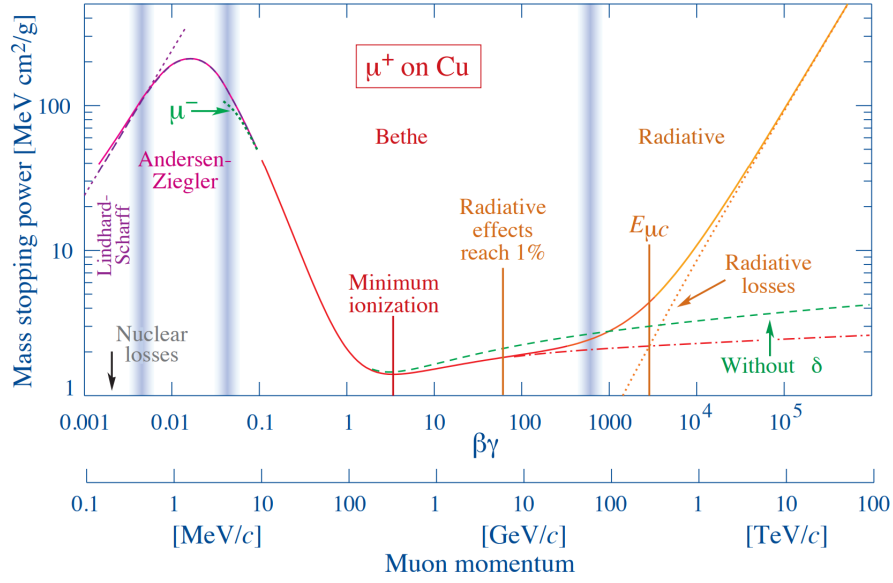


Figure 3.2: Mass stopping power (dE/dx) for anti-muons in copper as a function of the muon momentum. On the left-hand side of the plot, the energy loss of low-momentum muons is shown; in the middle, the energy loss follows the Bethe-Bloch equation, and on the right-hand side of the spectrum, radiative effects make the particle lose much energy. From Reference [48].

rarely for muons than for electrons. This is why for electrons, bremsstrahlung is the dominant energy-loss process, while for muons, ionisation energy loss dominates except at very high energies (muon energy larger than 100 GeV).

Multiple Scattering When a charged particle traverses matter, it not only interacts with the electrons inside the matter but also with the nuclei themselves. This electromagnetic interaction results in directional changes along the particle's trajectory, called multiple scattering. The magnitude of this effect depends on the material thickness x , which was traversed by the particle, the velocity of the particle $v = \beta c$ and the radiation length of the material X_0 . The radiation length is a quantity that characterises how charged particles interact inside a material. It depends on the atomic number Z and atomic mass A of the elements composing the material. The angle by which a particle is deflected from its trajectory by multiple scattering is measured by the particle's root mean square direction deviation. For small angles of deviation, it can be approximated by

$$\sqrt{\langle \Theta^2 \rangle} = \frac{z}{\beta c p} (20 \text{ MeV}) \sqrt{\frac{x}{X_0}}. \quad (3.1)$$

Where z is the particle's charge divided by the proton charge, and p is the momentum of the incoming particle. The radiation lengths for some common materials can be found in Table 3.1. [49]

The traversing particles will, on average, scatter over a large angle in one radiation length. Therefore, after one radiation length, the information about the

Material	Radiation length
Air	304 m
Water	36 cm
Carbon Fiber	237 mm
Silicon	9.36 cm

Table 3.1: Radiation lengths for different materials. Adapted from References [49, 50].

original trajectory of the scattered particle is smeared out considerably, which is why minimising the total radiation length of a tracking detector enables to measure the tracks more accurately.

Stopping power Furthermore, depending on the particle and the material, there is the possibility of complete absorption of the scattered particle inside the material. A particle can enter a material with very low momentum, and rather than being scattered over a large angle, it can be stopped completely by the material. In this case, the “range” of the particle, which is the distance travelled, might only have been a small fraction of one radiation length before the particle came to rest. The energy deposited inside the material can be measured to determine the particle’s energy when entering the material. Measuring the energy in this way is done by the second layer in a typical detector: the calorimeters. Generally, two different calorimeters are used: one for the heavier hadrons and one for the lighter electrons, which have a higher mass stopping power (dE/dx) and therefore travel a few cm in the heavy materials of the calorimeter before being stopped. [49]

Detection of charged particles In particle detectors, usually, one of the most interesting characteristics to know about a particle is its momentum. The ionisation trace a charged particle leaves in the detector can be measured in different layers, and the hits along its path can be used to reconstruct its trajectory. Different techniques can be used to detect charged particles. For this thesis, semiconductor sensors are used, which is why in the following, the focus lies on the material used for the CE-65: Silicon.

There are two ways of adjusting the properties of semiconductor materials by inserting foreign atoms into the semiconductor crystal, in a process called doping. For example, silicon is an atom with four valence electrons. One can insert a few atoms with five valence electrons, like phosphorus, into the silicon crystal to increase the number of conduction electrons over the number of holes. This process is called n-doping (negative doping, as the charge of the electrons, which become primary carriers). The second doping process is called p-doping (positive, as the charge of the imagined “holes”, where the electrons are missing). Here, an atom with three valence electrons, like Boron, is inserted into the silicon crystal to increase the number of holes over the number of electrons.

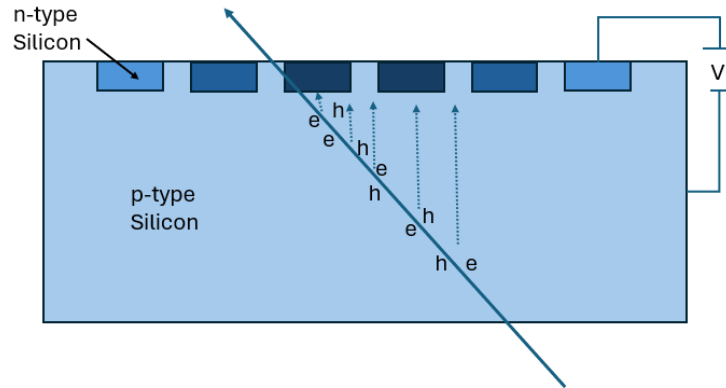


Figure 3.3: Sketch of the production and collection of charge carriers in a silicon sensor. Adapted from Reference [47].

In semiconductor sensors, one uses appropriately doped semiconductor materials, where from the charged particle traversing the material, the ionisation electrons and/or the ionised atoms (holes) are detected, see Figure 3.3.

In a semiconductor material, charge carriers move by diffusion, a process resulting from the thermally induced random motion of molecules. Diffusion generally makes the charge carriers move from a region of high concentration to a region of low concentration. A potential difference (indicated by V in Figure 3.3) across the semiconductor slice is applied for the detection, such that the charge carriers drift in the electric field, in addition to the movement induced by diffusion. This makes the charge collection in the n-type silicon faster, as the charge carriers don't move randomly but are more targeted. At one end of the semiconductor, collection electrodes collect the charge carriers. The sensors can be segmented in one dimension (strip sensors) or in two (pixel sensors), which provide a measure of the charged particle's passage through the sensor in two dimensions. After the charge carriers are detected, the signal is amplified and can be precisely assigned to the pixel/strip where the charge was collected. [47, 49]. The advantage of the semiconductor detector compared to, for example, gaseous detectors is mainly the amount of energy needed to produce one pair of free charge carriers. In a semiconductor, producing an electron-hole pair is about a factor of ten less than in a gas-based detector. However, the advantage of gas detectors is that they are lighter and that it is easier to build detectors, which cover large volumes. These two characteristics make the gas detector very well suited for an outer tracker part in addition to a silicon vertex detector, which is more precise. [51]. [49] [52]

Tracking detectors usually consist of multiple layers of sensitive elements, such that a charged particle produced in a collision will leave a hit in each of them to have enough information on the particle's trajectory to reconstruct a track. The tracker is usually placed inside a large solenoid, which spans a magnetic field over the detector in the direction of the colliding beams, making it possible to measure the particle's momentum: Due to the Lorentz force, the particle's trajectory leading away from

the IP is deviated in the direction $\vec{v} \times \vec{B}$, leading to a curved trajectory with radius R . From this radius and the angle between the particle and the beam pipe (λ), the particle's momentum can be determined using

$$p \cos \lambda = 0.3BR. \quad (3.2)$$

Where the momentum is given in GeV/c, the magnetic flux density B in Tesla and the radius R in meters [49]. For high-momentum particles, the radius can be in the range of 100 meters or more, which makes the trajectory look like a nearly straight line. A very precise spatial resolution is necessary for the vertex detector to deduce the momentum of such particles. [47]

Detection of photons In the tracker, the detection usually happens by ionisation of charged particles. Neutral particles are not detected in the tracker but only in the detector layers further downstream. An overview of the typical arrangement of the detector parts is shown using the example of the CMS detector in Figure 3.4

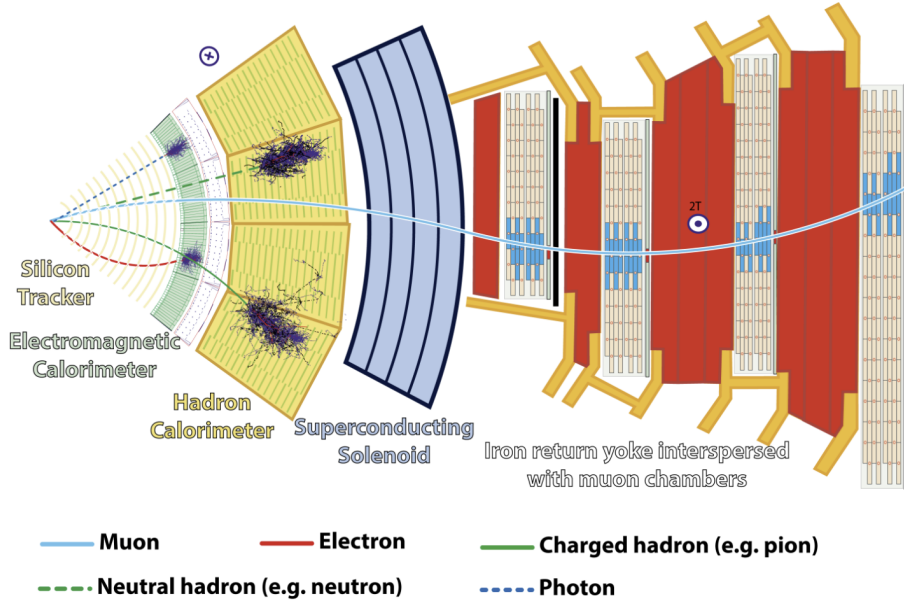


Figure 3.4: Overview of the arrangements of subdetectors in CMS. The innermost detector is the tracker, in which only charged particles leave hits. It is followed by the electromagnetic and hadronic calorimeters, which are encased by the magnet, and lastly, the return-yoke and the muon system are depicted. From Reference [53].

For photons, there are three interactions possible in matter. At low energies, the dominant process is the photoelectric effect, where the photon is absorbed by an atomic electron, which is thus ejected from the atom. This is the interaction which happens in a Silicon sensor if a measurement is taken using a radioactive source, like the ^{55}Fe source, used for calibration of the CE-65 sensors (see Chapter 5). At higher energies of $E_\gamma \sim 1 \text{ MeV}$, Compton scattering becomes significant. Here, the photon scatters in a two-by-two process off an atomic electron. At even higher energies

from $E_\gamma \sim 10 \text{ MeV}$ onwards, interactions of photons are dominated by e^+e^- -pair production in the field of the nucleus. When a high-energy electron traverses a medium, it loses energy by bremsstrahlung. It radiates a photon, which, in turn, is highly energetic and produces an e^+e^- -pair, which can interact with matter again. The radiation length of a material is defined as the average distance travelled by particles between the interactions. Accordingly, the number of particles roughly doubles after each radiation length. This process continues as long as the energy of the particles is above the critical energy. If the particle energy falls below it, the electrons and positrons start losing energy through ionisation. This process is called an electromagnetic shower and is used in particle detectors, usually in the detector after the tracker: the electromagnetic calorimeter (see Figure 3.4). Most of the electromagnetic shower originating from the electron is contained in the detector, and the energy can be determined. [49] [47]

3.2 Introduction to vertexing and parameters

For the calorimetry to be as accurate as possible, the innermost detector shown in Figure 3.4, the tracker has to be as light as possible. Also, it is desired to have the first detection layer as close to the beam pipe as possible, to detect the vertices of particles with short lifetimes. For particles with lifetimes of the order of picoseconds, like heavy quark hadrons, for example, the length travelled is about a millimetre or lower, depending on their momentum. If such a particle is produced in a collision, it can usually not reach the first detector layer and, hence, can not be measured directly. In such cases, its decay products can be measured instead, and their tracks extrapolated back to where they meet – reconstructing the decay vertex of the original particle. To reconstruct this secondary vertex efficiently and precisely, the resolution of the vertex detector has to be precise enough to distinguish the secondary vertex from the primary vertex. This distinction is the cornerstone for an essential parameter for vertex detectors, the resolution of the impact parameter; the closest distance from the track to the primary vertex of the collision is determined. [52]

Parameters for the silicon vertex detector A simplified two-layer detector is studied to see which parameters are important for a silicon vertex detector, where the sensor is segmented in two dimensions. The detector lies outside the beam pipe, close to the IP of an experiment. The two layers are at radii r_1 and r_2 and have spatial resolutions of σ_1 and σ_2 respectively. Assume that the tracks of the charged particles are straight lines and that negligible multiple scattering is involved in the vertex detector itself. To get the impact parameter resolution σ_b , consider the two extreme cases schematically represented in Figure 3.5.

If the first detector has a resolution of $\sigma_1 > 0$ and the second detector's resolution

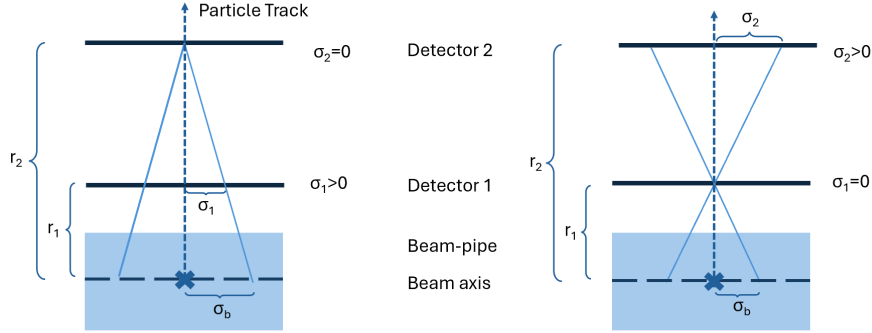


Figure 3.5: Simplified schematic of a 2-layer vertex detector. On the left, detector two is assumed to be ideal ($\sigma_2 = 0$), while on the right, it is detector one ($\sigma_1 = 0$). The X marks the IP, and σ_b denotes the extrapolated error in the measurement of the trace at the IP. Adapted from Reference [52].

is perfect, $\sigma_2 = 0$, the resolution of the impact parameter is given by

$$\sigma_b = \frac{r_2}{r_2 - r_1} \cdot \sigma_1 \quad . \quad (3.3)$$

If, on the other hand, detector 2 has a resolution of $\sigma_2 > 0$ and detector 1 has a perfect resolution, we find

$$\sigma_b = \frac{r_1}{r_2 - r_1} \cdot \sigma_2 \quad . \quad (3.4)$$

Altogether, from quadratically adding the two resolutions and including another term corresponding to the multiple scattering inside the material before the detector, i.e. the beam pipe and the detector material itself, σ_{ms} , we get

$$\sigma_b^2 = \left(\frac{r_1}{r_2 - r_1} \sigma_2 \right)^2 + \left(\frac{r_2}{r_2 - r_1} \sigma_1 \right)^2 + \sigma_{\text{ms}}^2 \quad . \quad (3.5)$$

From this formula, the following consequences for an ideal vertex detector arise:

- As the prefactor of σ_1 in the second term is dominant, the resolution of the first detector layer should be as good (small) as possible.
- The difference in distance of the two detector layers $r_2 - r_1$ should be as large as possible. In a real detector, there are more than two layers. In this case, the outermost layer should be as far away from the beam pipe as possible.
- As mentioned before, r_1 should be as close as possible to the IP.
- To minimise the multiple scattering in the beam pipe and the vertex detector, both should use materials with a long radiation length and be as thin as possible to minimise the material budget. Like this, particle tracks do not suffer from smeared-out directional information.

[52]

These are some of the most important considerations to keep in mind for the design and requirements of vertex detectors. They are also reflected in the requirements for possible FCC-ee vertex detectors.

Requirements on FCC-ee detectors In a real (not simplified) experiment, measuring the impact parameters of charged particle tracks is the task of the vertex detector and, as such, largely dependent on its performance. The resolution on these parameters usually scales with the transverse impact parameter, d_0 , defined as the shortest perpendicular distance from a track to the primary vertex. The transverse impact parameter is given by

$$\sigma(d_0) = a \oplus \frac{b}{p \sin^{3/2} \theta}. \quad (3.6)$$

Where a is dominated by the resolution on the hits, as the first two terms in our example above were dominated by the resolution the detector had on the single hits. The second term represents the contribution of multiple scattering, which was in our simplified example σ_{ms} . This term depends on the material budget of the vertex detector layers and the beam pipe. For the FCC-ee vertex detectors, a beam pipe radius of 11.7 mm is assumed, which allows for the vertex detector to be placed approximately two millimetres away, which influences the asymptotic variable a . Currently, the assumed required resolution on the transverse impact parameter is $3 \mu\text{m} \oplus 15 \mu\text{m GeV} / (p \sin^{3/2} \theta)$ [23]. The physics programme for FCC focuses more on the lower centre-of-mass regime than linear collider projects. To reconstruct particles with comparatively low momenta, a low material budget in the detector material of the vertex detector and the beam pipe is even more important than usual, as the inverse of the particle's momentum influences the second parameter of d_0 . The planned beam pipe has only a radiation length of 0.7 % X_0 and the baseline vertex detector designs aim for 0.3 % X_0 per detector layer. Such a low material budget can only be achieved if the detector uses air cooling, but requiring the sensors to be air-cooled means also that the power consumption of the sensors can not go over $\gtrsim 50 \text{ mW cm}^{-2}$. The sensor thickness should also be minimised, and lightweight support structures should be developed and used. The support of the detector inside the rest of the machine is a central part of the design for achieving such a low resolution. Consequently, the precise knowledge of the detector position inside the rest of the detector and the accelerator is an integral part of improving the resolution. In addition to these requirements for the impact parameters, the vertex reconstruction efficiency must be high. The vertex reconstruction efficiency is determined by two components: firstly, the angular coverage should be maximal, such that as few particles as possible escape the vertex detector unnoticed. A large forward coverage is thus envisioned for FCC-ee, going up to $|\cos \theta| = 0.99$, which means that a long barrel and forward disks are desirable. Secondly, the hit efficiency of the sensors themselves has to be high, such that no track is missed because the

hit is not seen. The efficiency is therefore required to be more than 99 % for a resolution of $3\text{ }\mu\text{m}$ [45]. See Table 3.2 for an overview of the requirements.

Physics challenges	Requirement
Coverage up to $ \cos(\theta) = 0.99$	Long barrel, forward disks
High reconstruction efficiency	Hermeticity, small peripheries, $>99\%$ hit eff., many layers
Asymptotic resolution of a $\approx 3\text{ }\mu\text{m}$	$3\text{ }\mu\text{m}$ single-hit resolution, first layer close to int. point
Multiple scattering: $b \approx 15\text{ }\mu\text{m GeV}$	Light beam pipe $\leq 0.3\% X_0/\text{layer} \rightarrow$ thin sensors, light support Air-cooling \rightarrow Power consumption $\lesssim 50\text{ mW cm}^{-2}$

Table 3.2: Overview of the physics challenges leading to the requirements for FCC-ee vertex detectors. From Reference [45].

Radiation tolerance Vertex detectors are usually exposed to a constant flux of charged and neutral particles and radioactivity. Being the closest detector to the beam pipe, they are most affected by the traversing particles' energy deposits. These energy deposits can damage the detector material depending on the amount of particle flux. The damage caused by radiation in silicon can roughly be divided into two parts:

- Damage to the sensor's surface. These kinds of radiation damage usually happen through ionising energy loss
- Damage of the silicon crystal volume itself by energy deposition. This damage is not dominated by ionising energy loss but by hits with the lattice atoms (non-ionising energy loss, NIEL). These lead, among others, to displacements of atoms in the lattice.

Substrate damage inside the crystal volume has a negative effect on the charge collection. Surface damage mainly results in the malfunction of CMOS electronics and the appearance of unwanted currents between the transistors. Damage to the crystal volume is the limiting factor for using silicon detectors in HEP experiments, so the sensors have to be tested to determine their radiation hardness. The NIEL damage caused by particle radiation is usually converted into the damaging effect that 1 MeV neutrons would have. The number of particles that traversed the material per cm^2 is therefore given in $1\text{ MeV}n_{\text{eq}}/\text{cm}^2$ (*1 MeV neutron equivalent per square centimetre*). [52, 54]

FCC-ee detector concepts The four proposed detector concepts for the FCC-ee, which were introduced at the end of Chapter 2 have significant differences, there are

large similarities between them in the general structure. They all include a tracking system, an ECAL, an HCAL and a solenoid magnet. Some groups also consider the use of specialised detectors like possible RICH detectors (CLD) or a drift chamber as part of the tracking system (IDEA). Still, all detector concepts plan to use Silicon pixels for their vertex detectors. There are only two proposed vertex detector layouts, as ALLEGRO and ILD currently use the vertex detector concepts of IDEA and CLD. The first layer of the CLD vertex detector is foreseen at a radius of only 12.5 mm from the IP. The CLD includes three double-sided barrel layers and three disks per side to ensure full coverage. For the IDEA vertex detector, the first layer would be at 13.7 mm radius and the outer barrel layer would be up to 315 mm in radius and three disks per side are planned at distances of up to 960 mm in the direction of the beam pipe [45].

Both vertex detector concepts foresee the usage of Monolithic Active Pixel sensors (MAPS), which unite a small pixel pitch, a low material budget and are cost-effective. The next chapter gives an introduction to this technology, as the CE-65 is a MAPS. [23, 41–45]

Chapter 4

Monolithic active pixel sensors and the CE-65 prototype chip

A pixel detector chip typically comprises two main components: a pixelated semiconductor sensor and front-end electronics. The sensor is responsible for detecting incoming particles or radiation, while the front-end electronics provide power, control signals, and handle data readout from the sensor. In hybrid pixel detectors, these two components are fabricated as separate silicon dies and interconnected using bump-bonding technology. This detector technology is beneficial for measuring large particle fluxes close to the IP and for very high radiation environments. The active sensor and the front-end chip can be developed and optimised separately for radiation hardness and rate capability in the case of hybrid detectors, which is an advantage of this structure. The disadvantages are the complex construction and costly assembly of the chip. Also, the pixel size of these sensors can not be below a certain threshold related to the diameter of the bump bonds. Furthermore, the hybrid structure of the chip also results in a comparably high material budget, which not only comes from the two-fold silicon usage in the two parts of the chip but also from the higher power consumption necessary for this type of detector. The hybrid pixel detectors in ATLAS and CMS have, for example, a material budget of more than 3 % X_0 /layer, which is an order of magnitude higher than what is acceptable for the requirements of FCC-ee. Monolithic structures in commercial CMOS processes should be used for detectors at future colliders. [52]

4.1 CMOS technology

A MOS (Metal-Oxide-Semiconductor) structure traditionally consists of a double interface formed between three distinct materials: a metal, an oxide layer, and a semiconductor. When using the MOS structure, two types of doping are distinguished. In the p-doped semiconductor, the holes dominate, while in the n-type, the electrons dominate. Many chip electronics used to read out detectors use a combination of NMOS and PMOS transistors on the same substrate (CMOS process). Each type of transistor is embedded in a well of opposite doping to enable

the integration of both n-type and p-type devices on the same substrate, as shown in Figure 4.1. [52]

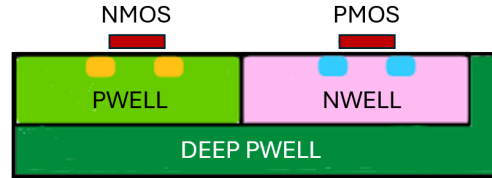


Figure 4.1: Schematic cross-section of a triple-well CMOS process. NMOS transistors are implemented in a P-Well, while PMOS transistors are placed in an N-Well, both of which are isolated within a Deep P-Well. This configuration allows NMOS and PMOS devices to be integrated on the same substrate, enabling the realisation of complementary CMOS logic used in complex switching circuits. From Reference [52].

Nowadays, in MOS structures, the metal part is generally replaced by strongly doped polysilicon, which can withstand higher temperatures without reacting with the oxide part. In the case of the CE-65 sensors, which are TPSCo 65 nm CMOS process chips, the MOS transistors are used to amplify the signal charge from the sensor. [52]

Another way to improve charge collection is by applying a bias voltage, creating a suitable electric field at the sensor. The silicon sensors used for this thesis consist of an epitaxial layer on top of a p-type substrate, and the collection electrode is n-type silicon. Between the collection electrode and the substrate, there is a p-n-junction, which collects the holes. A schematic of a p-n-junction is shown in Figure 4.2.

A bias voltage can be applied across a p-n junction to control the width of the depletion zone within the epitaxial layer, allowing it to be adjusted for a specific purpose. When a positive voltage is applied to the substrate relative to the collection electrode, the built-in potential of the p-n junction is reduced. This is known as **forward bias**. Under forward bias, more electrons diffuse from the n-type region to the p-type region, narrowing the depletion zone and increasing the conductivity of the semiconductor.

However, for semiconductor detectors, the **reversed bias** configuration is used. In this case, a negative voltage is applied to the p-type substrate and a positive voltage to the n-type collection electrode (i.e. $V_{\text{ext}} < 0$). This increases the built-in potential of the junction, thereby expanding the depletion region. Within this region, charge carriers generated by incident radiation drift under the influence of the electric field toward the collection electrode, where they can be read out. See Figure 4.3 for a schematic illustration of these processes. [52]

MAPS usually use an epitaxial silicon layer as the active part of the sensor, where the doping profile of the silicon can be controlled very precisely and independently of the substrate. Additionally, the epitaxial layer can be produced with exceptional purity, minimising the contamination from elements as oxygen and carbon. One of the longstanding challenges with MAPS was the limited size of the depletion zone.

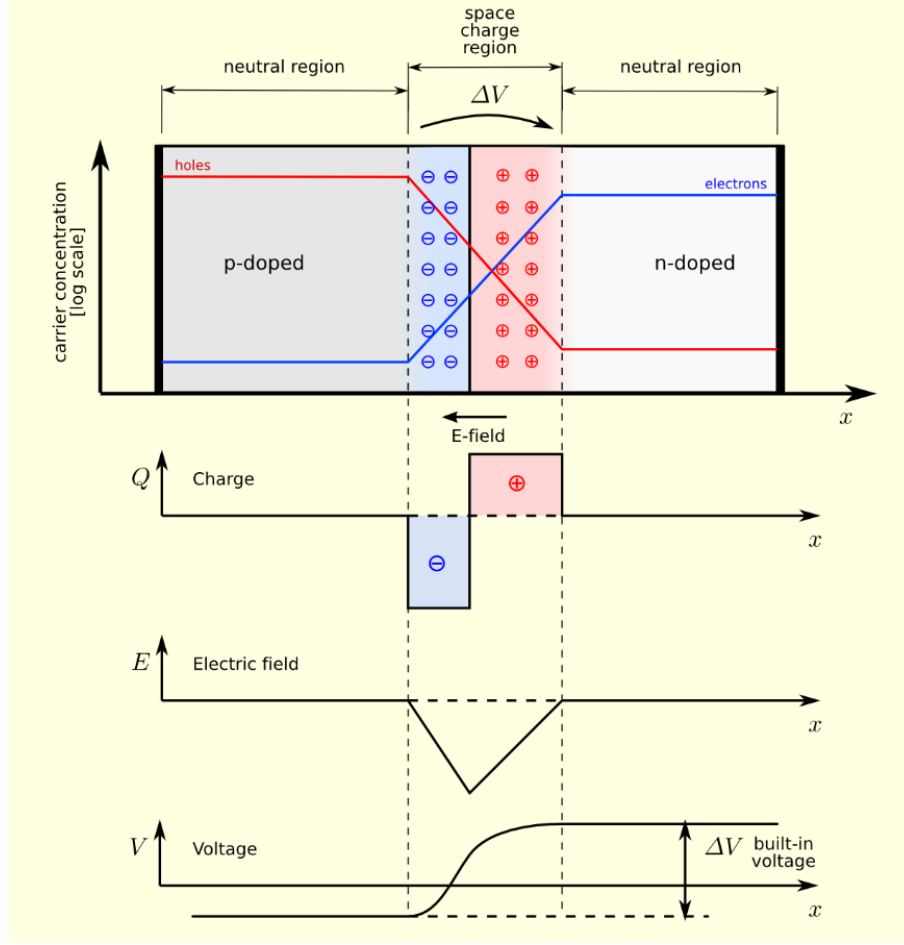


Figure 4.2: Schematic of a p-n-junction in thermal equilibrium, when no bias voltage is applied. From Reference [55].

Outside this zone, the charges liberated by the traversing particles move in the epitaxial layer by diffusion towards the depleted zone around the collection electrode, close to where the readout electronics are located. Only the particles generated in the depletion zone move by drift-dominated motion towards the electrode. Increasing the volume of the depleted zone makes the particles move faster, reducing the likelihood of charge loss due to recombination during diffusion. This improvement significantly enhances the timing performance and detection efficiency of the sensor. As a result of this advancement, MAPS technology has become suitable for use in high-performance particle physics experiments. [52]

The first MAPS-based vertex detector in particle physics was developed for the STAR experiment at Brookhaven's Relativistic Heavy Ion Collider. It used MI-MOSA pixels, where only the basic readout electronics could be implemented to complement the sensing part. The STAR experiment studied the extremely hot form of matter that formed at the beginning of our Universe, shortly after the Big Bang. During three years of data taking, the choice of CMOS monolithic detectors enhanced the capability to look into the quark-gluon plasma.

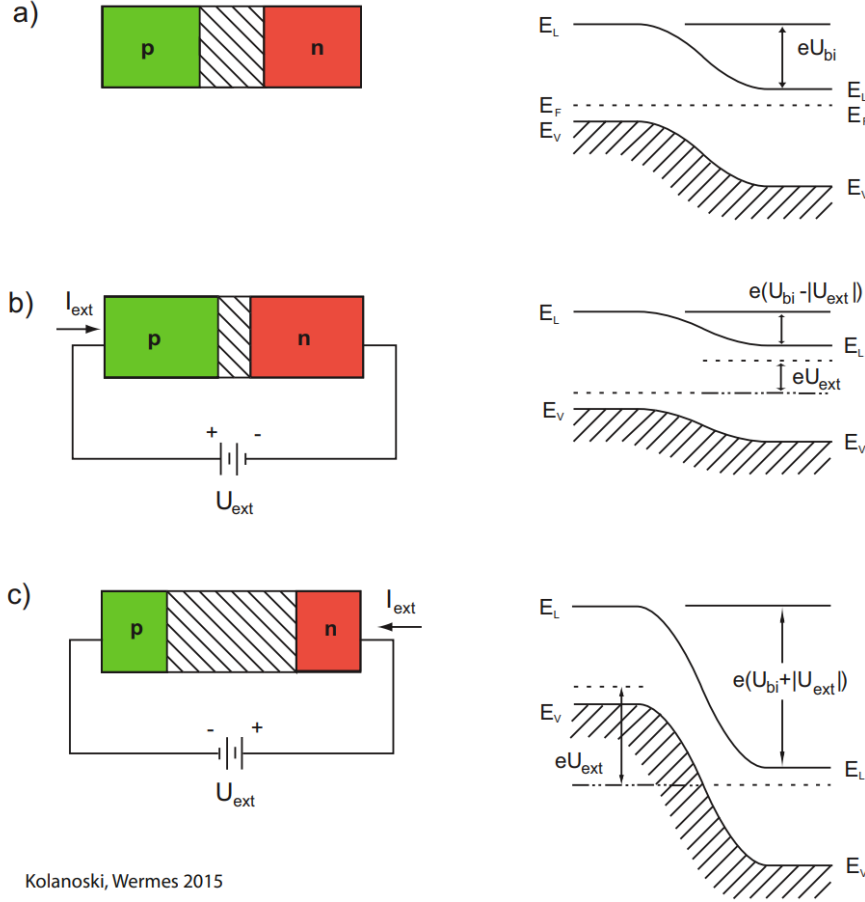


Figure 4.3: Schematic overview of the different kinds of bias voltage and their effect inside the semiconductor compared to no bias voltage. From Reference [52].

4.2 ALPIDE sensors

Another heavy ion collider experiment designed to study the physics of strongly interacting matter at extreme densities (where the quark-gluon plasma forms) is ALICE (A Large Ion Collider Experiment) at CERN. The whole detector was upgraded during the second Long Shutdown (LS2) at LHC to improve its physics reach. An essential part of this upgrade concerned the vertex detector, the so-called Inner Tracking System (ITS). This was replaced entirely with a new detector (ITS2) to improve, among other things, the tracking efficiency, the impact parameter resolution, and the readout capabilities. A significant step in this upgrade was the reduction of the size of the beam pipe to be only 18 mm in diameter instead of the former 28 mm, allowing the innermost layer of the vertex detector to be much closer to the interaction point. The ITS2 comprises seven cylindrical layers of MAPS, of which the first layer is located at a radius of 2.4 cm from the centre of the beam pipe. The MAPS in use in the ITS2 are named ALPIDE (ALice Pixel DEtector) [56], and a total of 24120 chips are used in the detector, covering an active area of 10 m^2 . They were the first MAPS to be used by an LHC experiment. [57]

ALPIDE MAPS has been developed explicitly for the ITS2 upgrade using the TowerJazz 180 nm CMOS Imaging Sensor process. Every chip measures $1.5 \text{ cm} \times 3 \text{ cm}$ and includes a matrix of 512-pixel rows and 1024-pixel columns. As seen in the schematic pixel cross-section of the ALPIDE in Figure 4.4, the collection electrodes in the chip are n-well diodes and have an area of ~ 100 times smaller than the pixel cell, which has a pitch of $\sim 29 \mu\text{m} \times 27 \mu\text{m}$.

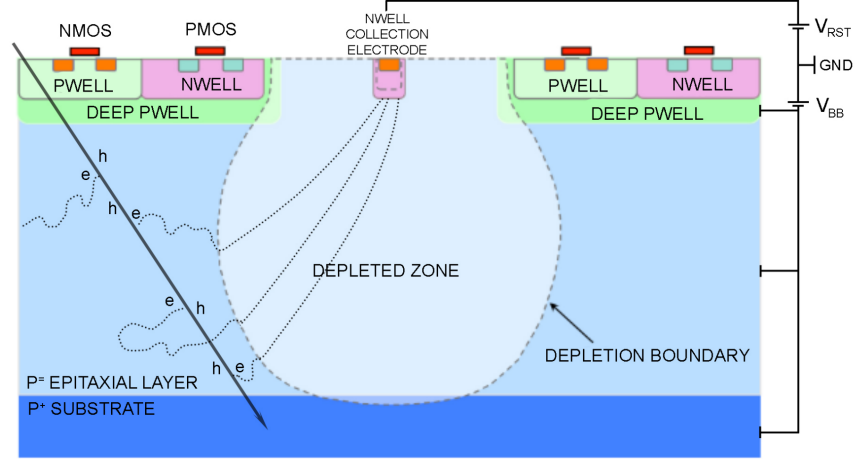


Figure 4.4: schematic cross-section of an ALPIDE MAPS. From Reference [57].

The signal is amplified and discriminated for each pixel separately. Test beam results have shown that the sensor has an intrinsic spatial resolution of $5 \mu\text{m}$ with a minimum detection efficiency of 99 %. A reversed bias voltage is applied to the $p+$ substrate to increase the signal-to-noise ratio. The bias voltage increases the depletion volume around the n-well collection electrodes, ensuring that the movement of charge carriers is dominated by drift towards the collection electrode, and more charge carriers are read out. [57] [58]

4.3 ALICE ITS3

This thesis focuses on characterising one of the chips developed in the context of designing the successor of ALICE's ITS2, but with a view to applications at future vertex detectors, especially at an e^+e^- collider. In the third Long Shutdown (LS3) at LHC, starting in 2026, the whole LHC is planned to undergo a major upgrade, which represents an important phase in enhancing CERN's capabilities and is mainly connected to the transformation of the LHC into the High Luminosity LHC (HL-LHC). ALICE is replacing its innermost three tracking layers during LS3 with a new detector, the ITS3 [59]. It will again be based on MAPS, which are newly developed for the ITS3 to reduce the material budget and increase the tracking precision and efficiency, especially at low p_T . The installation of a new beam pipe during the shutdown is also planned. The reduction of the material budget in the vertex detector

happens through *stitching*, a technology which is newly used and applied in HEP. Stitching allows MAPS to be constructed with up to wafer-scale size (~ 12 inches), helping to avoid dead areas between the detectors. Moreover, the material budget of the sensors themselves can be reduced by thinning them out to values of about $50\text{ }\mu\text{m}$. This thinning allows the silicon to be mechanically flexible, enabling it to be curved to match the cylindrical geometry of the detector. As a result, the need for passive mechanical support structures is significantly reduced, minimising the overall material budget. The new vertex detector will consist of three cylindrical layers, which include curved wafer-scale stitched sensors and feature a material budget of 0.07% X_0 per layer, instead of the former 0.35% per layer. Furthermore, the first layer in ITS3 can be positioned at a radial distance of 19 mm from the IP, where before it was at $\sim 24\text{ mm}$. The spatial resolution, radius and material budget determine the impact parameter resolution, as discussed in Section 3.2. For a summary of the requirements for ITS3 vertex detector chips compared to the requirements for FCC-ee vertex detectors, see Table 4.1. [59–61]

Requirements	ALICE ITS3	FCC-ee vertex
Sensor spatial resolution	$5\text{ }\mu\text{m}$	$3\text{ }\mu\text{m}$
Material budget per layer $[X_0]$	0.07%	$<0.3\%$
Radiation tolerance $[1\text{MeV neq/cm}^2]$	10^{13}	$\sim 10^{14}$ per year
First layer radius r_{min}	19 mm	13.7 mm
Power density	40 mW cm^{-2}	$\sim 50\text{ mW cm}^{-2}$
Particle hit density	8.5 MHz cm^{-2}	$\sim 250\text{ MHz cm}^{-2}$

Table 4.1: Table summarising the requirements on pixel sensors for the ITS3 detector and a possible vertex detector for FCC-ee. Numbers from References [23, 59].

The requirements for the silicon sensors considered for ITS3 are closely aligned with those anticipated for the vertex detectors at FCC-ee. For this reason, we extend the characterisation of one of the chips developed in the context of ALICE ITS3 to enable comparative testing of various chip designs. This approach may also help guide the development of suitable sensor technologies for the FCC-ee vertex detector.

Different chips and designs: APTS, DPTS, CE-65, MOSS, MOST To achieve the ambitious requirements of ITS3, three types of 65 nm CMOS chips were developed and studied thoroughly for comparison. These chips are called Analogue Pixel Test Structure (APTS), Digital Pixel Test Structure (DPTS), and Circuit Exploratoire 65 nm (CE-65). During the characterisation, the performance of irradiated chips was also tested, but these results are not part of this thesis. During the development phase of the sensors, ALICE designed two kinds of wafer-scale chips: MONolithic Stitched Sensors (MOSS) and MONolithic Stitched sensors with Timing (MOST), see Figure 4.5.

The MOSS was developed for high-energy physics using stitching, while the MOST has a different stitching approach, allowing for timing measurement. The

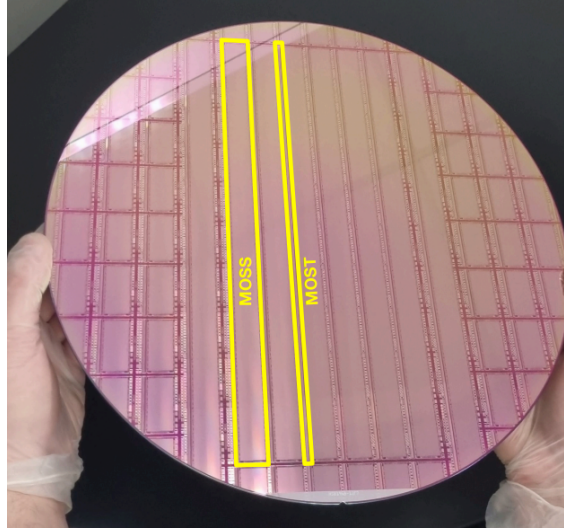


Figure 4.5: A 300 mm wafer containing six MOSS and MOST stitched sensors (indicated), as well as several small prototype chips. From Reference [59].

two sensors follow different approaches to preserve yield for a large stitched chip. Comparing and characterising both chips gives valuable information towards the final ITS3 chip design.

In the first tests, both sensor types work as expected. The interplay of different units of the same sensor yielded some insight into the coupling and requirements during powering on and configuration, which will be considered when designing the next stitched sensor type. [59]

In the scope of designing prototype structures for the ITS3, three different chips were designed: the APTS, the DPTS and the CE-65. The APTS is a pixel matrix prototype designed to test the sensor’s analogue response. The readout of the analogue pixel output allows direct evaluation of the pixel signal. The DPTS was designed to test the digital response. It contains a discriminator in the front end, which allows the qualification of the pixel cell. The complex structure of the front end can also be seen as a prototype for the final ITS3 sensor ASIC. The third type of chip is the CE-65. It is a commercial TowerJazz Panasonic Semiconductor Company (TPSCo) [62] 65 nm CMOS process, consisting of a large pixel matrix with a rolling shutter readout, where the matrix is read out row-by-row. Where the APTS has only a very small active area of 4×4 active pixels, the CE-65 provides analogue information for a matrix of 64×32 or 48×32 pixels for the first version of the chip (V1) and 48×24 pixels for the second version (V2), but at much more limited time resolution. The large pixel matrix size is interesting to study in-pixel effects, using the superimposition of the data measured by the pixels. APTS and CE-65 are complementary, while the DPTS implements a full asynchronous digital readout with time-over-threshold information. [59]

4.4 The CE-65 v2 prototype chip

At the beginning of 2023, a second version of the CE-65 chip was developed, the so-called CE-65v2. Both were explicitly designed to investigate the charge collection and the electrical properties of the 65 nm CMOS process through a selection of 15 configurations. The chips combine an analogue readout with a large pixel matrix using a slow readout. For the measurements, a resetting voltage in reverse bias of 4 V or 10 V was applied. The in-pixel circuitry consists of AC-coupled amplifiers, DC-separated from the input stage of the readout electronics. Therefore, the reverse bias is not limited by the power supply for the electronics. Unlike the CE-65v1, the second version of the chip is developed with exclusively AC in-pixel amplifiers. The 15 configurations of the CE-65v2 chip target the exploration of the following three main characteristics:

- Process variation, using the processes Standard, Modified and Modified with Gap
- Pitch variation, using 15 μm , 18 μm and 22.5 μm
- Matrix geometry, using squared and hexagonally stacked pixels.

Throughout this thesis, a comparison is made between the results with 10 V resetting voltage, which achieves full depletion of the pixel, and results with 4 V resetting voltage. [63]

The different pitch sizes allow the study of the improvement in spatial resolution when using smaller pitches. On the other side, smaller pitch sizes cause difficulties during manufacturing and generate a higher power dissipation, making it essential to explore at which size the desired spatial resolution can be achieved. [63]

For MAPS to be used in high-energy physics experiments, the most crucial development was a process modification which increased the extent of the depletion volume. Using this technology, the charge collection in a considerable part of the pixel volume is dominated by drift velocity instead of just diffusion, leading to less charge loss and more radiation hardness. A drift field following the depletion of the entire sensitive layer further improves radiation hardness for more demanding applications. The high electric field would push the charge carriers to their destination and reduce the collection time, as well as the probability for them to be captured by radiation-induced defects or radiation traps, leading them to be lost for the readout. The fully depleted sensor layer has been obtained with two process modifications, “Modified” and “Modified with gap”, compared to the standard process, which was the process already used in the ALPIDE pixel, where the epitaxial layer is only partially depleted, see Figure 4.6a. In the Standard process, the movements of charges outside the depleted region will be dominated by diffusion, making it the slowest and least radiation-tolerant of the three processes.

However, the “Standard” process is expected to have the most significant charge sharing. The charge sharing delivers information about where the hit has happened inside the pixel, when calculating the position by charge weighing techniques, and it could improve its spatial resolution to a range significantly below pixel pitch. For the “Modified” process, see Figure 4.6b, a low-dose n-type implant is added across

the whole pixel length. This implant causes the epitaxial layer to be fully depleted and the charge carriers to move by drift to the collection electrode. In the third process, “Modified with Gap” shown in Figure 4.6c, this lateral electric field is further increased with a gap, introduced at the edges of the low-dose n-implant. The gaps ensure that the charge collection is dominated by drift, even at the edges of the pixel.

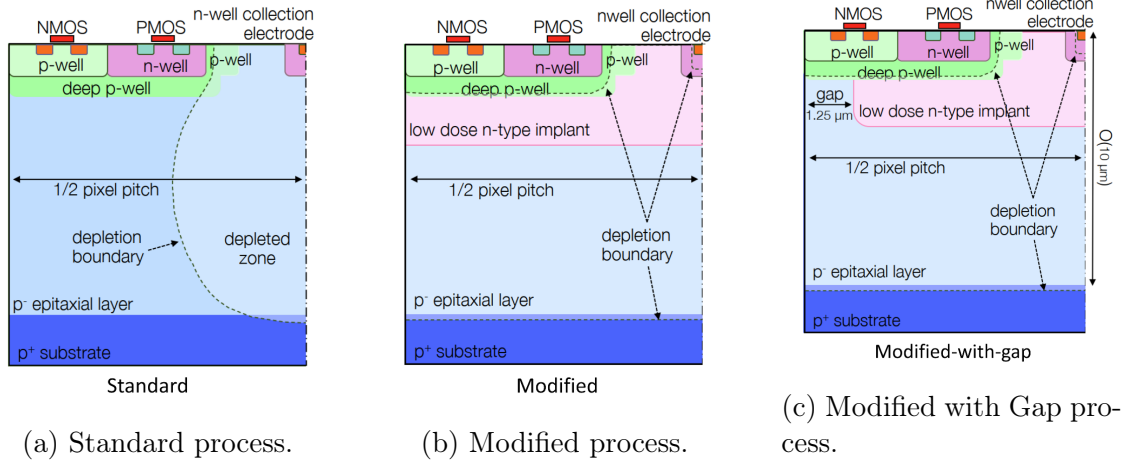


Figure 4.6: The three process options implemented in CE-65. From Reference [64].

The Modified and Modified with Gap processes have lower charge sharing, but they are expected to be more radiation-hard and possibly have a more efficient charge collection. For an overview of the characteristics of the Standard and Modified with gap processes, see Table 4.2. [64] [65] [63]

	Standard process	Modified with Gap process
Charge collection process	Diffusion dominated	Drift dominated
Charge sharing between neighbouring pixels	High	Low
Charge collection speed	Slow	Fast even at the edges
Radiation tolerance	Subject to charge trapping, less radiation tolerant	more radiation tolerant
Expected performance	Better resolution	Better efficiency

Table 4.2: Comparison between two of the three process variants, the CE-65 sensor comes in. These two variants are studied in this thesis.

In the next two chapters of this thesis, the characteristics of the standard and the modified with gap process are studied, for pixel cell sizes of $15\mu\text{m}$ as well as of $22.5\mu\text{m}$. For all four chip variants, a comparison is made between measurements with an applied resetting voltage of 4V compared to a resetting voltage of 10V . The effects are studied globally over the whole chip as well as in-pixel, to be able

to see which regions inside a pixel perform best and where efficiency or resolution losses occur. Determining the calibration factor is a vital first step in comparing the different chip variants. It enables the conversion of the readout analogue information to charge expressed in number of electrons. This is done in the analogue-to-digital converter (ADC).

In this thesis, the process variation between the Standard and Modified with gap processes and the difference between $15\mu\text{m}$ and $22.5\mu\text{m}$ pitch sizes are studied. These measurements, discussed in Chapter 5, are a necessary preparation for the test beam measurements discussed in Chapter 6.

Chapter 5

Lab measurements

Energy calibration is an essential first step in characterising a semiconductor sensor with an analogue readout. The spectrum from a radioactive source can be measured to calibrate sensors, as it is known very precisely. This measurement gives insight into the charge collection properties and the depletion of a sensor. In the sensor, the particles passing through the sensitive material react with it through ionisation, generating charge carriers, which are collected by the sensor. While inside the depleted material, the charge carriers drift towards the collection electrode; outside, they move by diffusion. This causes some of the charge carriers to be lost for the readout if, for example, the charge is shared between different pixels; hence, it falls below the threshold. By comparing the characteristic spectrum of the source to its measured spectrum, the conversion from analogue to digital counts can be calculated and used afterwards to analyse the test beam results shown in Chapter 6. By measuring the spectrum, it can also be determined whether all the charge generated within the sensor is measured.

5.1 Setup

To calibrate the CE-65v2 chip, the spectrum of an ^{55}Fe source was used. The ^{55}Fe isotope undergoes beta decay, where an electron is captured and the ^{55}Fe decays to ^{55}Mn with a half-life of 2.737 years. This effect is accompanied by X-ray emission where the most prominent peak is at an energy of 5.9 keV (K- α). A secondary peak (K- β) is at an energy of 6.5 keV, see Figure 5.1 for the whole spectrum of ^{55}Fe , including also two additional peaks. Only two peaks are expected to be observed, as the photons from the other radioactive transitions carry too little energy to be recorded. Matching the measured peak position known in Arbitrary Digital Units (ADU) of the K- α to the given energy value makes it possible to determine the conversion factor between ADU and energy. However, the conversion factor, or calibration factor, is often not expressed in eV/ADU, but it is usually given in terms of electrons corresponding to the number of electron-hole pairs produced in the ionisation process in silicon [66]. On average, the energy of 3.6 eV is required to produce an e-h pair. For the peaks of 5.9 and 6.5 keV, this leads to an average of \sim

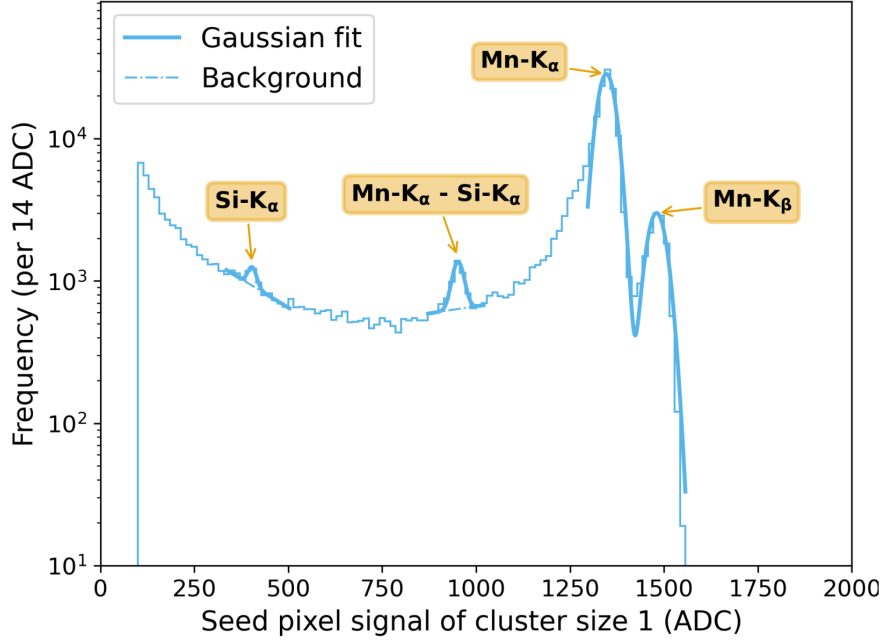


Figure 5.1: ^{55}Fe energy spectrum for events with cluster size 1. From Reference [66].

1640 and ~ 1800 e-h pairs, respectively [67].

The different chip versions of the CE-65 were calibrated using the setup shown in Figure 5.2. The Device Under Test (DUT) is mounted on a carrier board, transmitting the measured and amplified signal to the proximity board. The proximity board hosts the ADCs and provides the chip with power and reversed bias voltage. The digitised signal is then transmitted to the data acquisition (DAQ) board, which features a Field-Programmable Gate Array (FPGA). The FPGA handles the read-out, processes the incoming data, and transmits it to a connected laptop for storage and further analysis. The radiation source is mounted on a movable holder equipped with a tube supplying dry air to maintain a low-humidity environment. The chip under test is cooled via pipes integrated into the aluminium mount of the Device Under Test (DUT), which are connected to a chiller operating at 20°C . These measures, dry air supply and active cooling, ensure the sensor operates under stable and controlled conditions, enabling reproducible and comparable measurements. The complete setup also includes a power supply that powers the DAQ board and applies the reverse bias voltage to the sensor.

5.2 Method

The raw data in the form of 32-bit words is passed from the DAQ board to the EventBuilder, which packs them into CE-65 frames. Like this, the energy measured in every pixel is recorded within a very short time. If one of the pixels measures an energy above the seed threshold, the four frames before and the four consecutive frames are read out. The analogue signal in the main frame is computed offline by

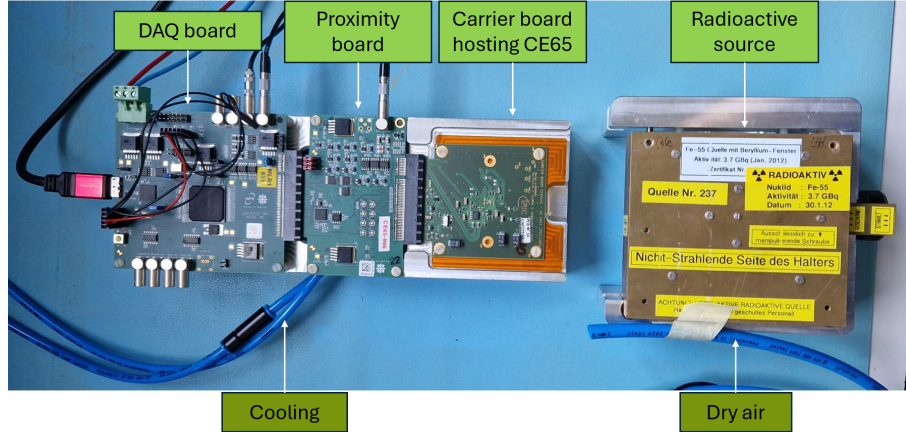


Figure 5.2: Measurement setup as used for the energy calibration. From left to right, the setup components include a DAQ board connected to the proximity board, which is connected to the carrier board, where the sensor is glued on and connected via wire bonds. At the bottom of the picture, the cage for the radioactive source is visible, which can then be placed on top of the sensors. The blue tube attached to it brings dry air, while the two blue tubes which run under the proximity boards are connected to the chiller, bringing the cooling water.

subtracting the average signal in the successive frames. In this way, the baseline noise can be minimised. An online cut ensures that the amount of data recorded is not unnecessarily large and that the recorded frames include pixels above a specific threshold value. This threshold value is set to 800 ADUs. In the offline analysis, a pixel surpassing a threshold of 900 ADUs is regarded as a seed pixel for the cluster reconstruction. The 3×3 matrix surrounding this pixel is considered in the reconstruction. Each pixel must surpass a threshold of 300 ADUs, corresponding to approximately 2 times the Root Mean Square (RMS) noise, to be regarded as a neighbouring pixel and thus as belonging to the cluster. The raw data, where only the online cut and the cuts of the offline pre-processing were applied, is shown in Figure 5.3 for the Standard and Modified with Gap processes, respectively. A clear distinction in the charge-sharing behaviour can be observed between the two. For the Modified with Gap process variant (Figure 5.3a), charge sharing is reduced. This is reflected in the plot being narrower on the left-hand side and more heavily populated on the right-hand side, indicating that a larger fraction of the deposited charge is collected in the seed pixel. Furthermore, a diagonal border of the population, going through the plot origin, can be seen for this process variant, indicating that a significant fraction of clusters with multiple pixels have cluster size 2. In contrast, the Standard process chip (Figure 5.3b) shows more frequent charge sharing, with energy more often distributed across neighbouring pixels, leading to a broader spread on the left-hand side of the distribution. The diagonal band present in both plots corresponds to the total energy deposition of a $K\text{-}\alpha$ X-ray event, where the combined energy of the seed and neighbouring pixels sums to a constant value.

In the following, the four different chip variants are compared based on their ^{55}Fe

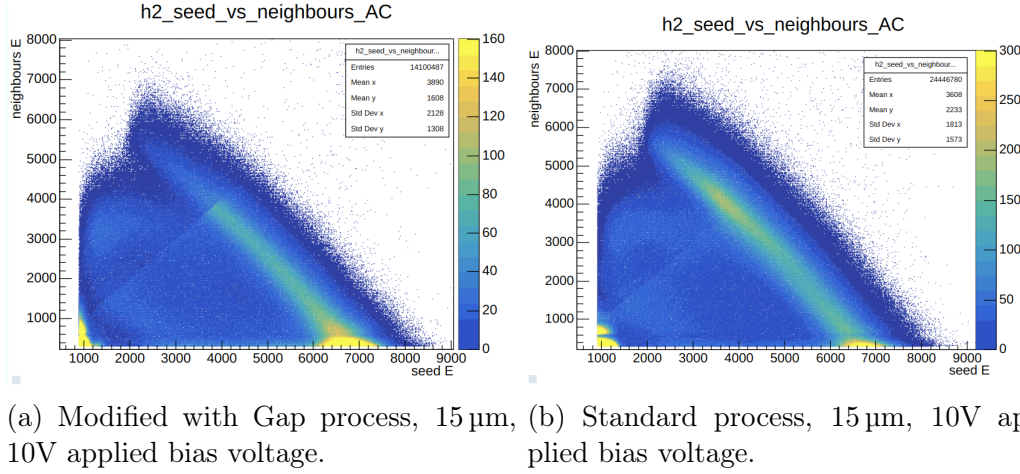


Figure 5.3: Seed pixel energy versus sum of neighbour pixel energies in a raw data file.

spectrum measurements. The calibration factors were evaluated using the Gaussian fitted mean of the K- α peaks, for reversed bias voltages of 4 V and 10 V respectively. The comparisons are performed using the entire sensor matrix except the outermost rows and columns of pixels, which were left out, so there are no edge effects.

A file, expressed in ADU, was saved for the analysis of the calibration factor and the pixel-by-pixel analysis in such a way that all the charge of the K-peaks is recorded by a single pixel. If the clusters evaluated for these analyses were larger, the charge would be shared between multiple pixels. When analysing the data with cluster size = 1, the information from the neighbouring pixels is not evaluated, enabling a clearer picture of the performance of the pixel in question. To have enough data to do pixel-by-pixel measurements without overlaying each pixel inside the matrix, six-day measurements were taken to analyse. These measurements usually result in ~ 4000 events per pixel, enabling smooth energy spectra analyses.

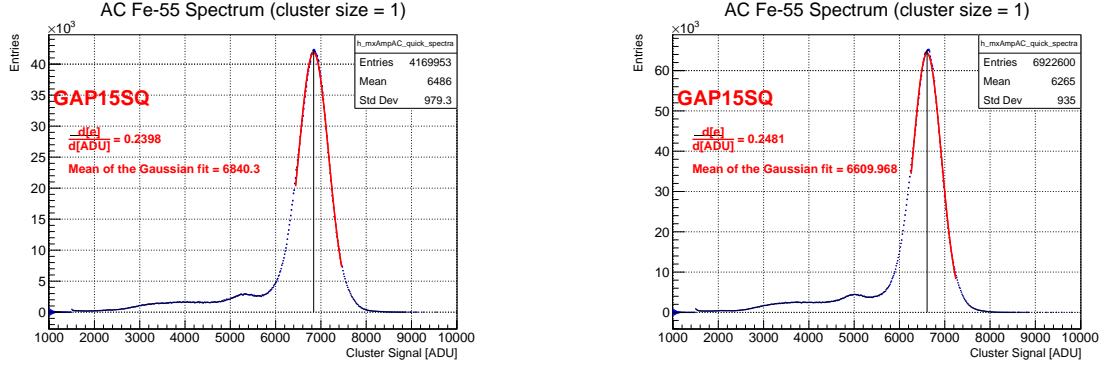
5.3 Results

5.3.1 Global spectrum measurements

The global energy spectrum measurements of the X-rays coming from the ^{55}Fe source, measured by the Modified with Gap process sensor, are shown in Figure 5.4. These spectra are measured using the smaller pitch size of $15\ \mu\text{m}$. Figure 5.4a shows the spectrum measured with an applied reversed bias voltage of 10 V. The mean of the Gaussian fit (indicated in red) of the K- α peak lies at 7063 ADU, corresponding to 1640 electrons. This leads to the conversion factor indicated in red of 0.232 electrons/ADU. Figure 5.4b shows the spectrum measured by the same sensor with an applied voltage of 4 V. The mean of the Gaussian fit of the K- α peak lies at 6610 ADU, leading to a conversion factor of 0.248 electrons/ADU, as indicated on the plot.

The difference in the fitted peaks leads to a difference in the conversion factors.

Given that the same chip was used for these measurements, we can assume that the variance is due to the applied bias voltage.



(a) Modified with Gap process, pitch size 15 μm , at 10 V.

(b) Modified with Gap process, pitch size 15 μm , at 4 V.

Figure 5.4: ^{55}Fe spectrum for single pixel clusters of the entire matrix. The Gaussian fit is marked in red.

The calibration factor measured with 4 V bias voltage is higher for all four chip variants. With an applied bias voltage of 10 V, the $k\text{-}\alpha$ peak is si

For a comparison of the different pitches, Figure 5.5 shows the global spectrum measurements of the two Standard process chips, while Figure 5.6 shows the global spectrum measurements of the two Modified with Gap process chips. The DAQ and proximity boards used at the test beams were utilised for all four measurements. For both processes, the fitted mean values of the smaller pitch sizes lie slightly below the mean evaluated for the larger ones. This leads the conversion factors to be a bit larger for the 15 μm pitched sensors. In the Standard process variant, the mean of the fitted Gaussian of the smaller (larger) pitch is evaluated to be 6836 ADU (6989 ADU), leading to a conversion factor, as indicated, of 0.240 electrons/ADU (0.235 electrons/ADU). For the Modified with Gap process variant, the mean values of the fitted Gaussian are slightly higher than for the Standard process variant. This effect comes from charge-sharing effects in the Standard process chips. If the charge from the seed pixel is shared with neighbouring pixels not reaching the threshold of 300 ADUs, the cluster size for the event is still 1, and it contributes to this analysis. The effect is small, as this can only happen with minimal charge sharing. For the smaller (larger) pitch, they correspond to 6951 ADU (7063 ADU), leading to a conversion factor of 0.236 electrons/ADU (0.232 electrons/ADU).

For an overview of all calibration factors evaluated in the scope of this thesis, please check Table 5.1.

5.3.2 Comparison of calibration factors

The calibration factor was initially calculated using a proximity board and a DAQ board, which were not used in the test beams. As there was a different proximity board to transform the sensor signal from analogue to digital (ADC), the conversion factor of the two setups has to be determined. To accomplish this, one of the

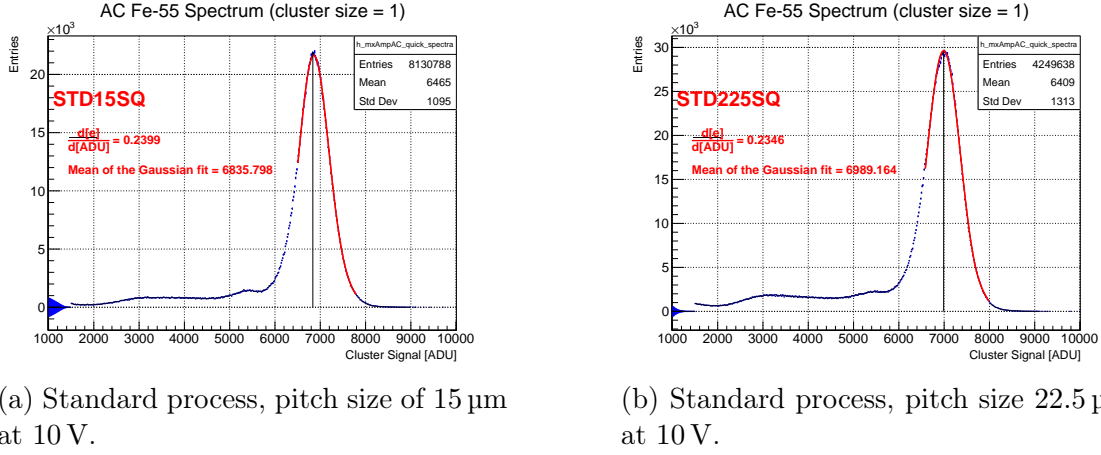


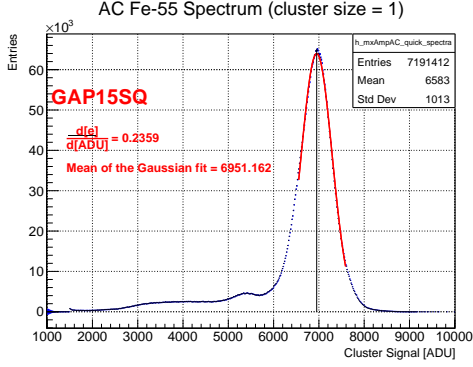
Figure 5.5: ^{55}Fe spectrum for single pixel clusters of the entire matrix. The Gaussian fit is marked in red. Comparison of Standard process chips with different pixel pitches.

	Gap 15	Gap 22.5	STD 15	STD 22.5
4 V	0.248	0.253	0.250	0.246
10 V	0.236	0.232	0.240	0.235

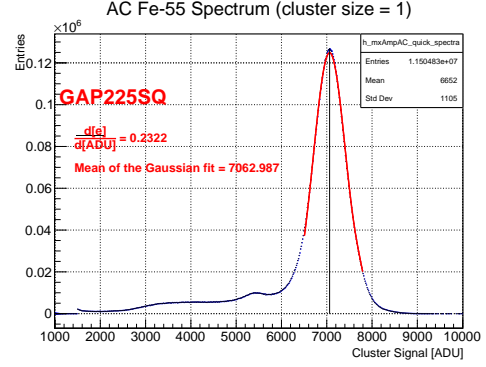
Table 5.1: Overview of the calibration factors calculated in the analysis. GAP represents the Modified with Gap chip variants, while STD stands for Standard variants. The subsequent number 15 or 22.5 indicates the pixel pitch. All calibration factors are given in electrons/ADU.

calibration measurements was repeated using a board from Strasbourg, which was used at the test beams. The conversion of the calibration measurements with these two setups is compared in the following. In Figure 5.7, the global energy spectrum measurements using the DAQ and proximity boards used at the test beams (Figure 5.7a) and those originally used at the UZH setup (Figure 5.7b) are shown. The comparison uses the Modified with Gap chips of 15 μm of pitch. The difference in the calibration factors evaluated in these measurements is 0.038 electrons/ADU. Although this is not a big difference, it will shift the threshold values for test beam measurements, as these are given in electrons and converted for the analysis to ADU.

The calibration factor was calculated with the DAQ and proximity boards used in the SPS test beam, and the test beam analysis procedure was performed again for one single measurement with the updated calibration, resulting in minor changes in the results. In Figure 5.8, the deviation is shown for the Modified with Gap chip of 15 μm of pitch, as an example. The shift in the x-axis is only marginally visible for high Seed Threshold values, and for the other chips, the test beam analysis was not retaken.



(a) Modified with Gap process, pitch size of $15\ \mu\text{m}$ at 10 V.



(b) Modified with Gap process, pitch size $22.5\ \mu\text{m}$ at 10 V.

Figure 5.6: ^{55}Fe spectrum for single pixel clusters of the entire matrix. The Gaussian fit is marked in red. Comparison of Modified with Gap process chips with different pixel pitches.

5.3.3 K-beta peak fitting

Due to the pixel-to-pixel gain variation, the K- β peak can not be seen in the global plots. The gain variations can be minimised by calculating the calibration factor for each pixel separately. Pixel-by-pixel studies are also done to confirm the linearity of the calibration factor, as it should be the same when evaluated at the K- α peak as at the K- β peak. In the pixel-by-pixel studies of the different chip variants, another difficulty with the K- β peak becomes apparent.

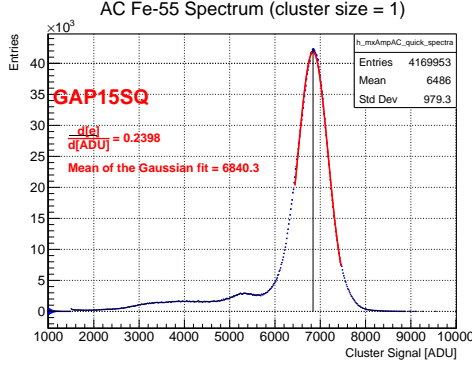
All the plots in this subsection are evaluated using data taken with the Modified with Gap process chip featuring a pitch size of $15\ \mu\text{m}$. For coherence, all the arguments are made on the same measurement, which was taken using the DAQ and proximity boards from the UZH and applying a reversed bias voltage of 4 V. Note, however, that the problems in fitting the K- β peak arise with all four tested chips at both bias voltages. For these analyses, a double Gaussian fit was performed.

While the K- α mean values are distributed approximately Gaussian, as expected, the K- β values are smeared out to the left. In Figure 5.9, the distributions of the mean values are shown.

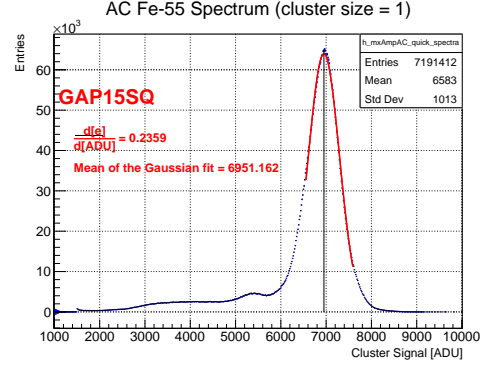
Figure 5.10 shows the pixel-by-pixel evaluation of the K- β mean value, divided by the K- α mean value. The ratio is calculated from the data in ADU. As the calibration factor is constant within the pixel, the ratio is expected to be 1.1017 (ratio of the peaks at 5.9 and 6.5 keV). However, the peak in Figure 5.10 is clearly below this value at 1.06 with the right-hand side tail smeared out towards ~ 1.070 .

Corresponding to this smaller ratio, the fitted Gaussians of the measured K- α and K- β peaks must be closer than expected. Pixel-by-pixel energy spectrum measurement plots can roughly be divided into three categories.

Pixels, of which the measured spectra are similar to the one shown in Figure 5.11, contain a shifted, but steep K- β peak, leading to interferences with the K- α peak. In these cases, the two fitted Gaussians have means very close together, leading to the



(a) Modified with Gap process, pitch size of 15 μm at 10 V. Measurement taken with the test beam DAQ and proximity board.



(b) Modified with Gap process, pitch size 15 μm at 10 V. Measurement taken with the UZH DAQ and proximity board.

Figure 5.7: ^{55}Fe spectrum for single pixel clusters of the entire matrix. The Gaussian fit is marked in red. Comparison of the different measurement setups.

ratio of the peaks to be close to 1. Such distributions are observed in most pixels, leading to the peak in Figure 5.10.

Pixels with measured spectra similar to the one shown in Figure 5.12 have a clearly visible peak, where the fit does not interfere with the fit from the K- α peak. For such pixels, the mean of the K- β peak has a significant distance to the mean of the K- α peak, enabling the ratio of the two peaks to be higher, corresponding to the data smearing out the Gaussian in Figure 5.10 at ~ 1.070 . It could be that the sensor is not completely linear; however, the reason why this ratio is not closer to 1.1017 is not clear.

In some rare cases, the energy spectrum measurement features a K- α peak with a flat K- β peak. In these cases, the second Gaussian fit is observable only in the right-hand side tail of the K- α peak, which is smeared out. See Figure 5.13 for an example of such a distribution. In comparison to the first case, where the two peaks are also interfering, the amplitude of the second peak is fitted to be smaller in these cases, which is why the two mean values are further apart. In Figure 5.10, these cases are the rarely occurring entries to the right of the peak.

Different ways of fitting the two Gaussians for the single pixel spectra exist. Even though the K- β peak is visible and well fitted in some of the pixels, the ratio of the two peaks usually does not come close to the expected 1.1017. The reason for this behaviour could be a non-linearity of the CE-65 in the high end of the energy spectrum, as the analysis was done with enough data to ensure good visibility of a peak in lower energy, even on a pixel-by-pixel basis. Cross-checking with measurements of the APTS sensor [66] shows that they did not have this problem in the pixel-by-pixel analysis.

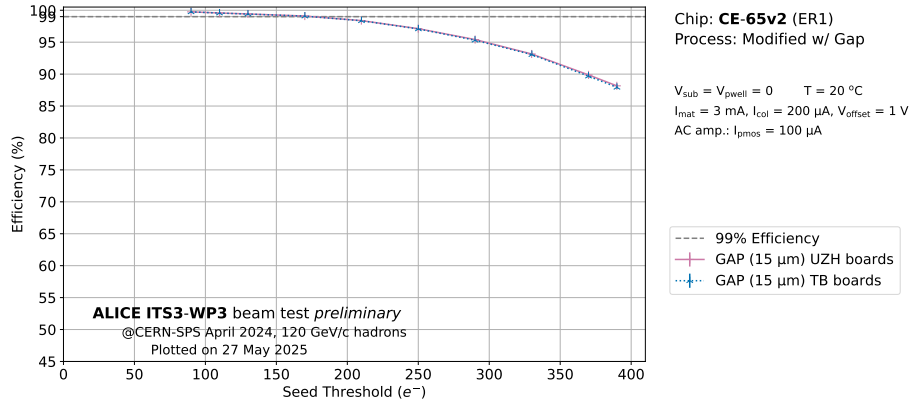
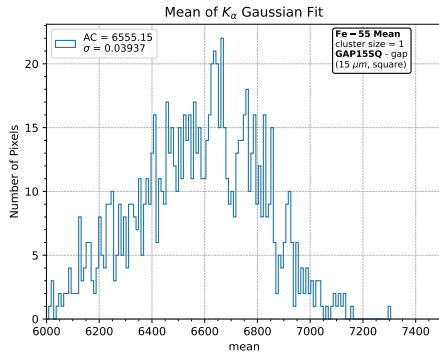
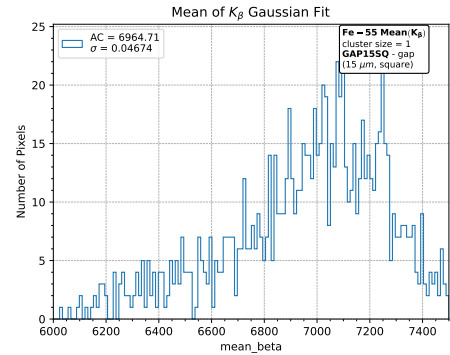


Figure 5.8: Comparison of the global efficiency analysed with the calibration factor determined with the test beam PCBs to an analysis, where the calibration factor was calculated from measurements taken with the UZH PCBs.

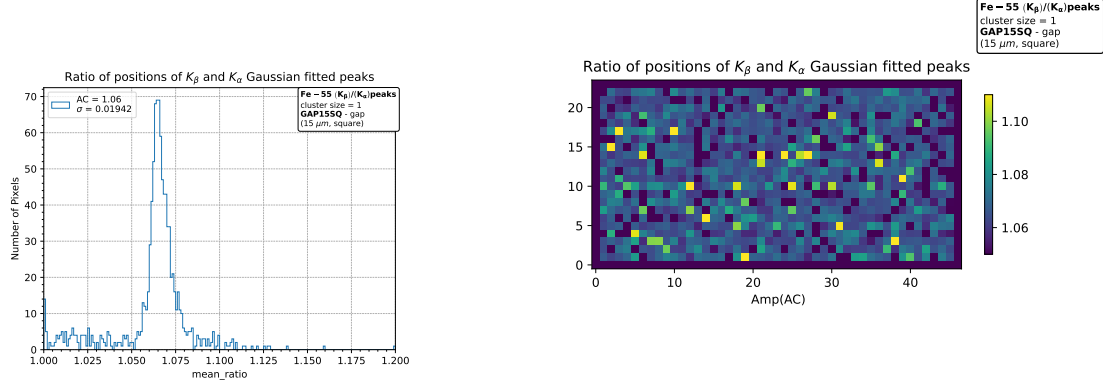


(a) Modified with Gap process, pitch size of 15 μm at 4 V. Distribution of mean values of K- α peak.



(b) Modified with Gap process, pitch size 15 μm at 4 V. Distribution of mean values of K- β peak.

Figure 5.9: Distributions of pixel-by-pixel mean values for K- α and K- β peaks.



(a) One-dimensional distribution of ratio values.

(b) Two-dimensional distribution of ratio values.

Figure 5.10: Pixel-by-pixel ratio of K_β/K_α peak mean values.

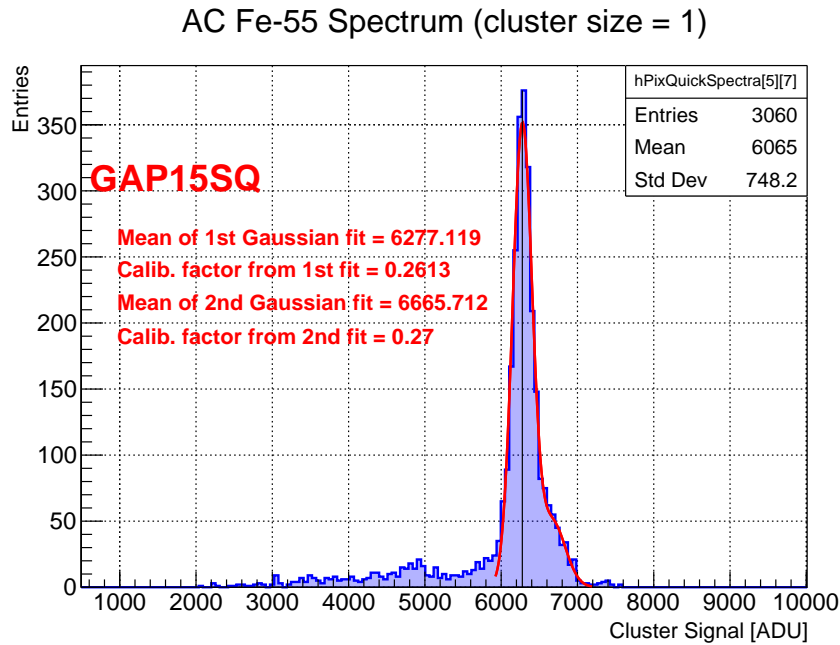


Figure 5.11: Measured energy spectrum of pixel [5][7]. The red line indicates the double Gaussian fit. The fit of the steep K_β peak is shifted towards the K_α peak.

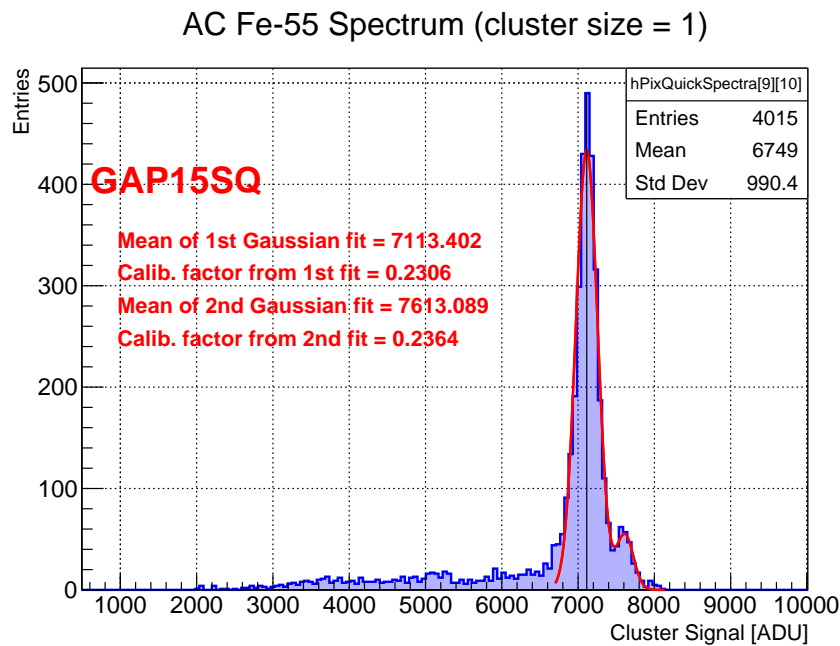


Figure 5.12: Measured energy spectrum of pixel [9][10]. The red line indicates the double Gaussian fit. K- β peak is fitted as expected.

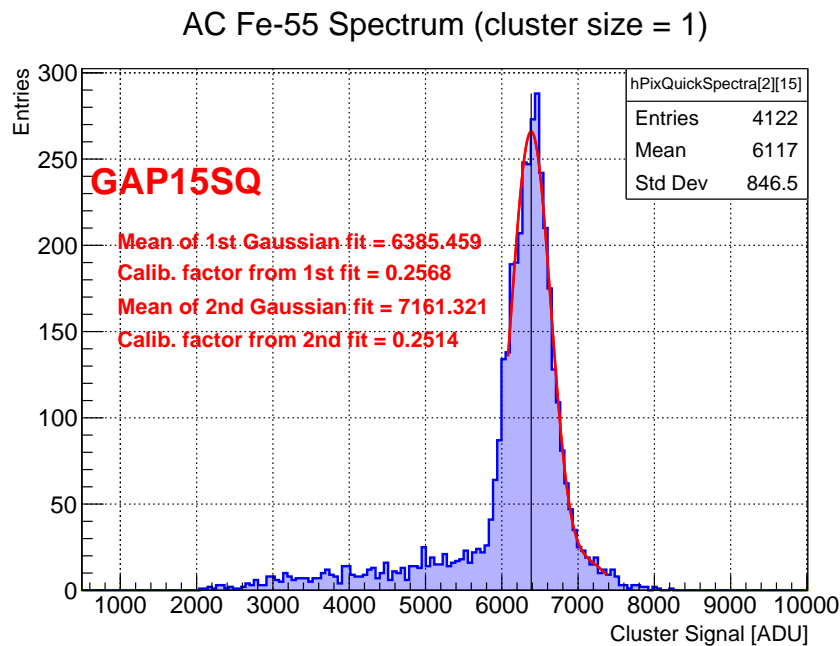


Figure 5.13: Measured energy spectrum of pixel [2][15]. The red line indicates the double Gaussian fit. The fit of the flat K- β peak is shifted towards the K- α peak.

Chapter 6

Test beam measurements

Measurements were taken at a test beam to compare the performance of the different chip variants in an environment with real but controlled conditions. There, a beam of accelerated particles is deviated towards an experimental site, where the sensor can be mounted in the beamline to take measurements. To see how the device under testing (DUT) performs, it is placed within a telescope, an array of multiple sensors. This array of silicon detectors is placed one after another along the direction of the beam. These planes, built with a well-proven technology, reconstruct the direction of each incoming particle. The track path is then extrapolated to the DUT plane, in such a way that the DUT spatial resolution and efficiency can be reconstructed. During the last year, two test beams were conducted to test CE-65 sensors. In April 2024, a test beam was conducted at CERN's SPS North Area test beam facility (H6 beamline) [68], using a beam of mixed hadrons of 120 GeV energy. In May 2024, a test beam was conducted at the DESY test beam facility at beamline 24 [69], where we used electrons of 3 GeV. These two experimental conditions are very different, reflecting the different research motivation of the two test beams. The CERN test beam was conducted to study non-irradiated sensors with better spatial resolution, while at DESY, the primary research motivation was to study the effects that irradiation has on the chips, for which the worse spatial resolution of the DESY TB facility was less problematic.

This thesis focuses on analysing the data collected at the SPS test beam. The measurements taken at this test beam aim to study the global and in-pixel analysis of the resolution and the efficiency of the sensors. At the SPS test beam, different bias voltages of 4 V and 10 V were tested and compared.

6.1 Setup

The telescope was the same in both of these test beams. It consisted of six ALPIDE reference planes, a DPTS trigger and the DUT. The arrangement is shown in Figure 6.1.

The reference planes provide an estimated tracking resolution of the telescope of $2.2\text{ }\mu\text{m}$. The estimate was done using the telescope optimiser, a software optimising the position of DUT and telescope planes, for the given geometry [70]. The DUT and

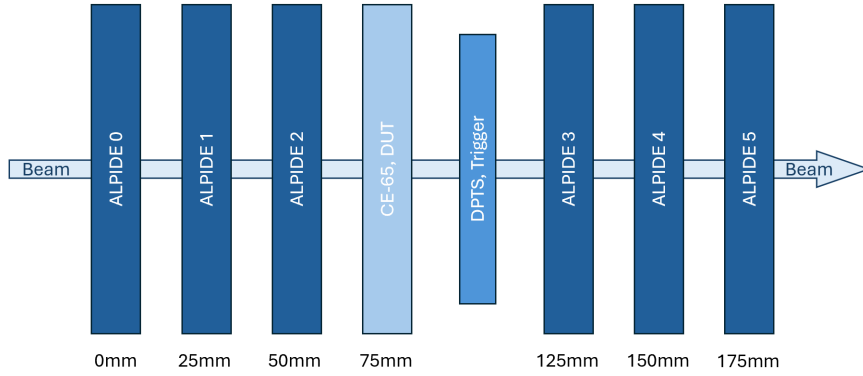


Figure 6.1: Schematic representation of the telescope components used at CE-65 test beams at CERN and DESY. The particle beam traverses from left to right, passing first three ALPIDE reference planes, next the DUT, followed by the DPTS trigger, before hitting again three reference planes. The reference planes and the DUT are equispaced with 25mm.

the trigger were placed between the first three and the last three reference planes. The trigger ensures that only events which pass through the DUT are recorded. This is vital, as the ALPIDE chip has a much larger sensitive area than the DUT. As a trigger, a DPTS [71] was mounted on a movable stage to be aligned by remote control with the DUT. During the measurements at CERN, the DUT was cooled to a steady temperature of 20°C, the same as in the lab. For the measurements with the irradiated sensors, the temperature was set lower, as these sensors perform much better in a cold environment. There, the chiller was set to 0°C, ensuring a chip temperature of 15°C. The sensors were mounted inside a metal box, which was covered with a black towel during the measurements to minimise background effects coming from the light in the experimental hall. This coverage caused some instabilities in the temperature of the ALPIDE planes, as they were not cooled directly. The complete experimental setup is shown in Figure 6.2. It also includes the connection to the power supplies and the computer from which measurements and the movable stage, as well as the power supplies, were controlled. The telescope is placed on a height-adjustable table, remotely controllable from the hut.

Before starting the first measurement, the experiment was mounted in the area. The telescope was brought into position with the height-adjustable table, and the cables were secured. Afterwards, a noise run was carried out, where the beam was kept off to measure the background noise. The trigger, which was initially adjusted inside the telescope by eye to align with the DUT, was then positioned with finer accuracy using the movable stage. The measurement started when the beam was seen in the recorded frames of the DUT. This adjustment of the trigger had to be repeated each time the DUT was changed, as this changed the position of the device by up to a few hundred μm .

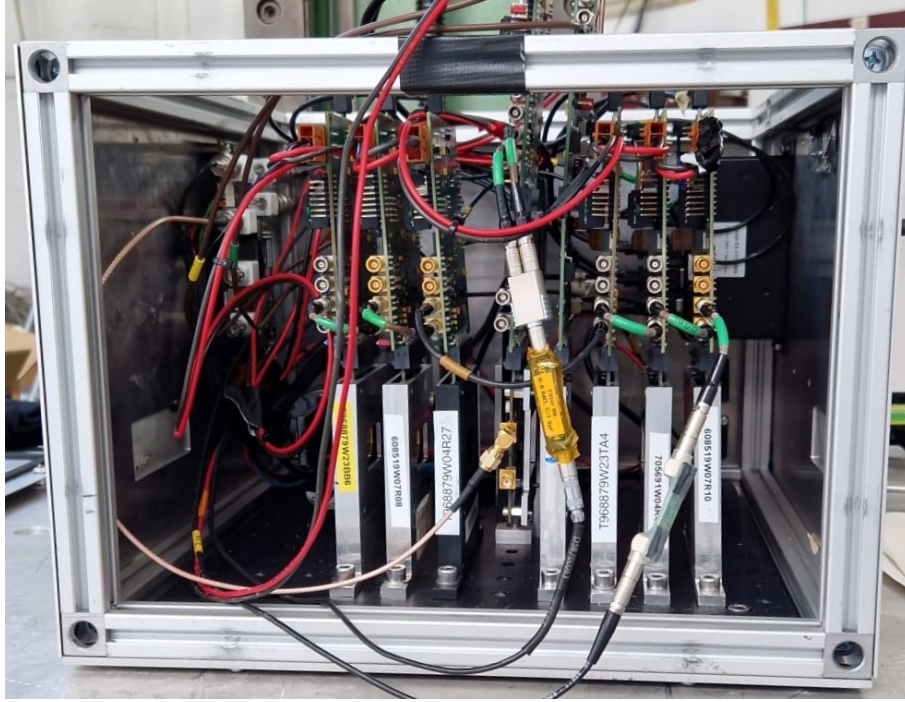


Figure 6.2: Picture of the telescope used at DESY. The order of the planes is mirrored with respect to the scheme shown in Figure 6.1.

6.2 Collected datasets

The data presented in this chapter was taken from test beam measurements performed using the following sensors:

- PCB 19, Modified with Gap process, $15\mu\text{m}$ pitch size. Measurements taken with 4 V and 10 V bias voltage.
- PCB 10, Modified with Gap process, $22.5\mu\text{m}$ pitch size. Measurements taken with 10 V bias voltage.
- PCB 7 from Prague, Modified with Gap process, $22.5\mu\text{m}$ pitch size. Measurements taken with 4 V bias voltage were used for this analysis, as there were no measurements with 4 V bias voltage taken with the PCB 10.
- PCB 6, Standard process, $15\mu\text{m}$ pitch size. Measurements taken with 4 V and 10 V bias voltage.
- PCB 18, Standard process, $22.5\mu\text{m}$ pitch size. Measurements taken with 4 V and 10 V bias voltage.

For the global characterisation, a single beam run with approximately 50'000 trigger hits was analysed. For an overview of how many trigger hits this corresponds to per sensor and applied voltage, see Table 6.1 for the global analysis.

From these trigger hits, usually between a third and half of them can be used for the analysis. In Table 6.2, the number of tracks used for the global study is shown per sensor and applied voltage.

	Gap 15	Gap 22.5	STD 15	STD22.5
4 V	50 132	50 126	50 074	50 050
10 V	50 151	50 189	50 236	50 066

Table 6.1: Number of trigger hits per file used to perform the analysis shown in this chapter.

	Gap 15	Gap 22.5	STD 15	STD22.5
4 V	18 837	19 914	21 075	29 068
10 V	20 013	27 289	19 664	30 208

Table 6.2: Number of good tracks reconstructed from the trigger hits and used to analyse global efficiency and resolution.

For the in-pixel studies, the data from different runs was merged. For the Modified with Gap process variant with 15 μm pitch size, 10 beam runs were used, corresponding to 478'065 trigger hits. For the Standard process variant with 15 μm pitch size, the data of 7 beam runs was used, totalling 400'814 trigger hits. Of these trigger hits, 190'151 (163'960) tracks were used for the Modified with Gap (Standard) process in the analysis.

6.3 Analysis

The analysis of the test beam data was done using the Corryvreckan analysis and reconstruction framework [72]. It has been designed especially to simplify the reconstruction of data recorded at test beams. Written in C++, the framework features a modular design in which the separate modules implement the individual steps of the reconstruction process. The flexibility of the framework allows the reconstruction chain to be adapted to different analysis requirements. Also, it enables the direct processing of simulated detector responses in the same way as the reconstruction of the experimental data in the analysis. As described before, the planes of the telescope are used to reconstruct particle tracks. From a reconstructed track on the reference planes, the hit on the DUT can be extrapolated, and a window (region of interest or ROI) can be defined on the DUT, where the hit is expected to be. If the centre of mass of a pixel cluster associated to a hit is found to be inside this window on the DUT, this hit is associated to the track. For an overview of the analysis chain used here, see Figure 6.3.

The first step of the reconstruction chain consists of masking noisy pixels. These pixels return artificial hits, not generated by the interaction of charged particles inside their sensitive volume. If such a pixel is not masked on the reference planes of the telescope, it can falsify the alignment, resulting in a shift of the reconstructed traces of particles. Likewise, noisy pixels can occur on the DUT itself, where it is equally important to mask them for the clusters on the DUT to be reconstructed

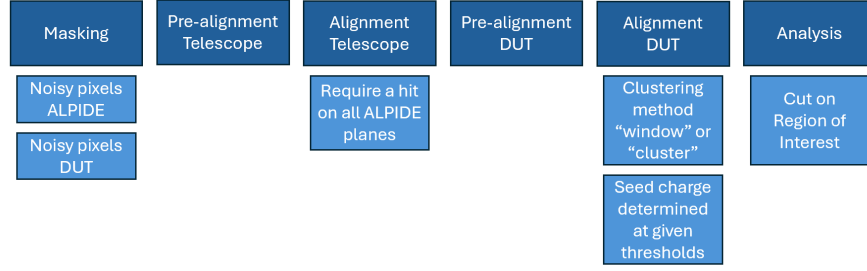


Figure 6.3: Flowchart of the analysis chain.

correctly. If the noisy pixels are not masked, the ROI is shifted accordingly, and the extrapolated track of the particle cannot be matched with a cluster on the DUT. In Figure 6.4b, an example of a shifted region of interest is shown. This shift follows the appearance of four noisy pixels on the DUT, shown in the hit map of Figure 6.4a. Following the shift of the ROI, the reconstruction algorithm could not match clusters correctly, leading to the cluster map in Figure 6.4c. Such a faulty reconstruction leads the analysis to fail completely for higher seed thresholds, which again causes the reconstructed efficiency to go below 1%. In the given example, the efficiency was reconstructed to be $0.1 \pm 0.0\%$. For comparison, Figure 6.5a shows the hitmap with masked pixels, from which an aligned ROI can be calculated as shown in Figure 6.5b. The effect of the mask can be observed in the clustermap of Figure 6.5c, where all the clusters that would contain the masked pixels are also omitted. This results in two holes in the upper right part of the cluster map. The masking leads to an efficiency of $93.9 \pm 0.2\%$.

The next step is the alignment of the reference planes to the beamline. The geometry of the telescope is defined beforehand in a geometry file, shown in Figure 6.6, which includes the benchmark measurement for the alignment, as this measurement can not be done precisely enough by hand. However, the X and Y positions of the single planes and the precise orientation angle strongly influence the track reconstruction. The telescope alignment consists of a separate pre-alignment and alignment step, which are both repeated multiple times. In these steps, the planes of the telescope are shifted and rotated iteratively with respect to a plane defined as the reference plane (in our case, plane three of the telescope was used). After the track is reconstructed, the position where the hit is expected to be on the DUT is calculated. Subsequently, the spatial distance between this expected hit position and the actually measured hit position of the DUT, the residual, is evaluated. An example of the residual determined in the analysis step for the Modified with Gap process chip with a pitch size of $22.5\text{ }\mu\text{m}$, is shown in Figure 6.7.

All the alignment steps target iteratively the improvement of the residual. In the pre-alignment of the telescope, the correlations between all detector planes of the setup and the plane beforehand defined as the reference plane are calculated. By shifting and rotating the positions saved in the geometry file, the other planes

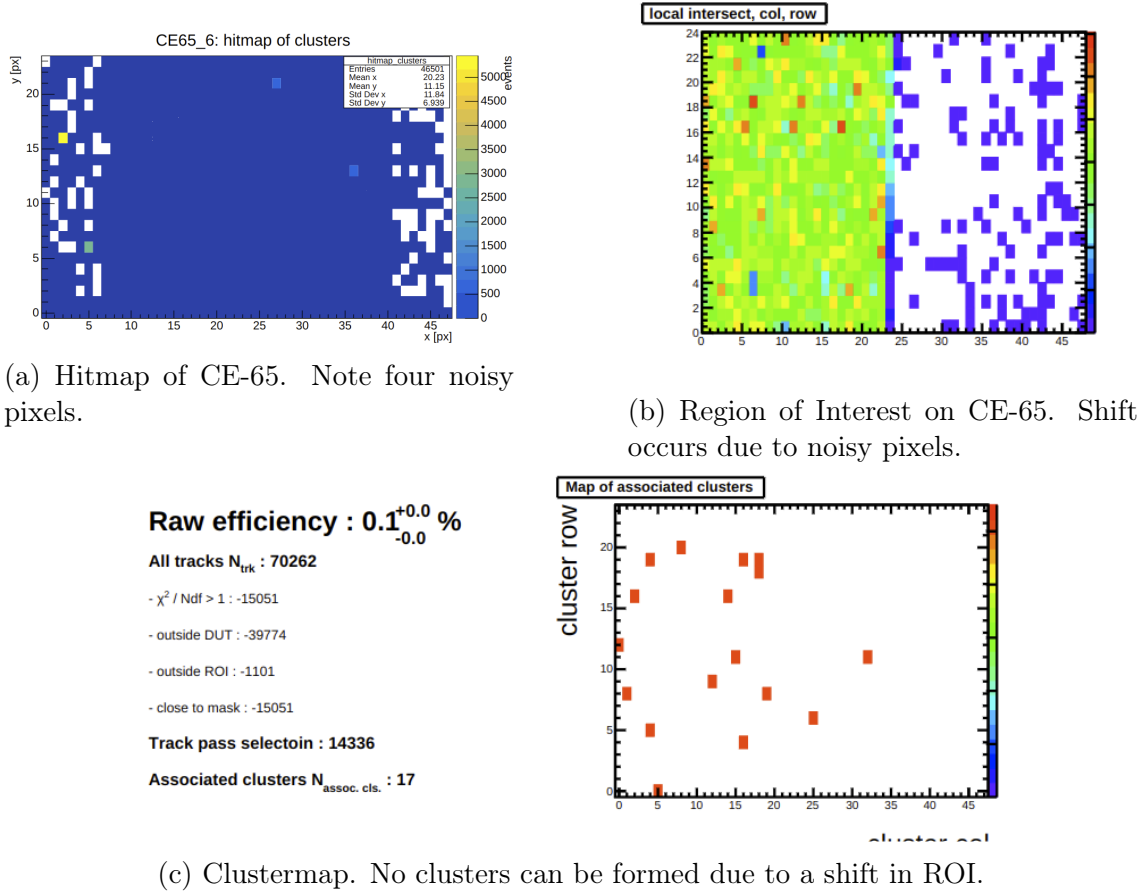


Figure 6.4: Analysis plots of a measurement without masking noisy DUT pixels.

of the telescope are aligned during multiple iterations. The improvement on the residual during the iterations is shown for the Standard process chip of $15\text{ }\mu\text{m}$ pitch size in Figure 6.8. These measurements were taken with an applied voltage of 10 V. After this relatively loose matching criteria, it is possible to perform tracking. The preliminary tracks are the input to the second step of the alignment. With the Millepede-II package [73], the simultaneous fit of all track candidates can be performed to determine the alignment corrections simultaneously. In the alignment step, events which include a hit in each reference plane are selected.

Next, the DUT is aligned to the rest of the telescope, following a repeatable two-step procedure, where in the second step, the clusterisation is done. There, clusters are calculated via a nearest neighbour search from all signals of a specific chip, followed by determining the hit position (seed pixel) using a charge-weighted centre-of-gravity algorithm. It can be done following either the “cluster” method or the “window” method. In the “cluster” method, the pixels, which form the cluster around a seed pixel, are chosen according to their own charge amplitude in the event. They are selected if their amplitude exceeds the same charge threshold as the seed pixel. In the “window” method, on the other hand, the threshold for the neighbouring pixels is effectively zero – all eight direct neighbour pixels to the seed

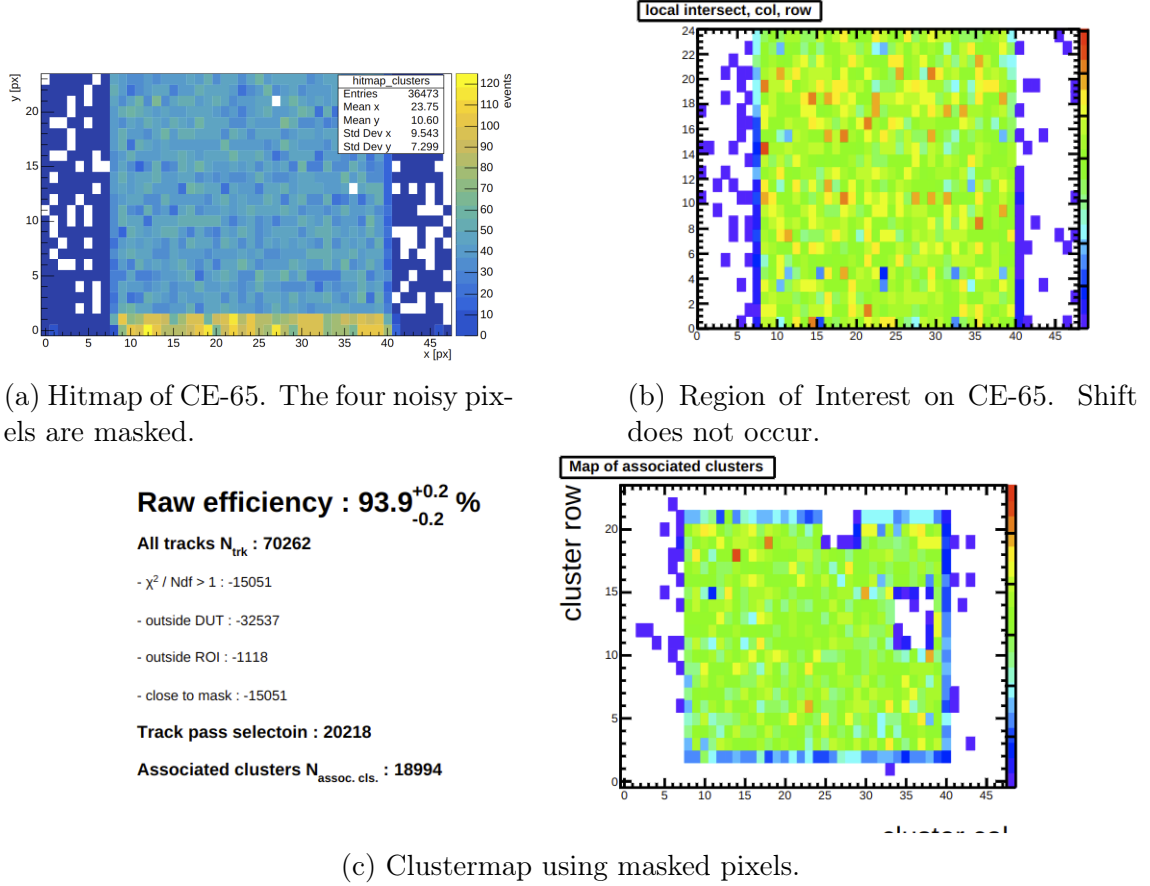


Figure 6.5: Analysis plots of the same measurement as in Figure 6.4, but with masked noisy pixels on DUT.

will be contained in the cluster. The “cluster” method is used in the global plots as efficiency is represented more accurately by this method. In contrast, in the “window” method, the efficiency is biased, as all neighbouring pixels are read out, even if the charge they measured is low. However, the “window” method is useful for showing the improvement of the resolution coming from charge sharing effects in standard chips. There, the charge of the neighbouring pixels is low, and thus, it’s difficult for them to pass the neighbour threshold cut using the “cluster” method. In the alignment of the DUT, the seed charge thresholds are altered so that the seed charge can be analysed at different thresholds. [72]

6.4 Results

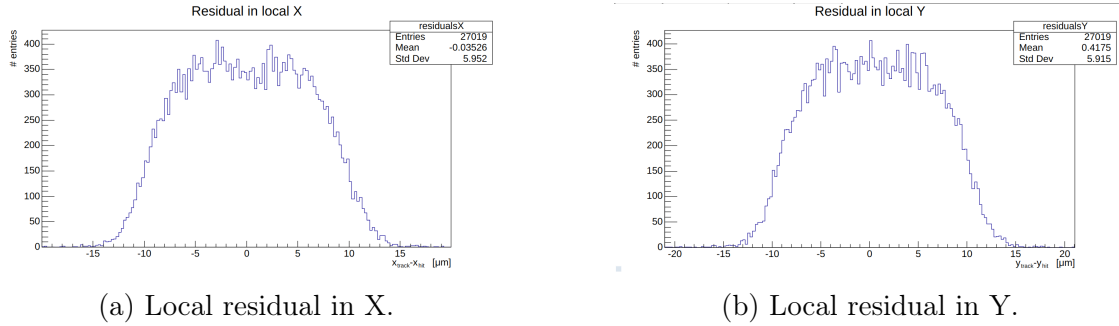
To characterise the CE-65 sensors in test beams, the detection efficiency and the spatial resolution were evaluated for the whole sensor, averaging over each pixel. Likewise, measurements were taken for the spatial resolution and the detection efficiency to be evaluated inside one pixel. The performance of different regions inside the pixel can be studied by superimposing the measurements taken in every pixel of the large matrix.

```

45
46 [ALPIDE_3]
47 type = "ALPIDE"
48 position = 0um,0um,125mm
49 number_of_pixels = 1024,512
50 pixel_pitch = 29.24um, 26.88um
51 spatial_resolution = 5.00um, 5.00um
52 time_resolution = 2us
53 material_budget = 0.0005
54 coordinates = "cartesian"
55 orientation_mode = "xyz"
56 # orientation = 180deg, 180deg, 0deg
57 mask_file="/local/ITS3utils/SPS202404/masks/GAP155Q/ref-plane3_HV10.txt"
58 orientation = 0deg, 0deg, 0deg
59 role = "reference"
60

```

Figure 6.6: Extract from geometry file. Initial parameters of reference plane 3.



(a) Local residual in X.

(b) Local residual in Y.

Figure 6.7: Residuals of DUT after the alignments of the telescope and the DUT.

6.4.1 Global efficiency and spatial resolution

For the global studies, charge sharing behaviour is very important, as it significantly impacts both the efficiency and the spatial resolution. In Figure 6.9, the accumulated charge ratio is shown as a function of the number of pixels in a cluster to study the extent of charge sharing for the two process variants. As a 3×3 matrix around the seed pixel was considered candidates for a cluster, 9 pixels were also considered for this analysis. The pixels were ordered by the amount of charge they carry, normalised by the total charge, defined as the sum of the charge of all pixels in the 3×3 matrix. For more details on how the analysis was performed, see [63]. Comparing the two plots, the different charge-sharing properties become apparent. As the accumulated charge ratio for the seed pixel (pixel no. 1) for the Standard process is much smaller than for the Modified with Gap process, the charge is much more distributed to the neighbouring pixels in the Standard process. The uniform distribution for the Modified with Gap process variant shows that charge sharing is not as significant in this process variant.

To study the performance of the CE-65 in efficiency and spatial resolution, the “cluster” method was used to reconstruct the DUT hits. To determine and compare these two parameters of all four different chip variants at both bias voltages of 4 V and 10 V, they were evaluated at ten seed threshold values ranging from 90 to 390 electrons, with the lowest set to approximately three times the noise RMS, as for

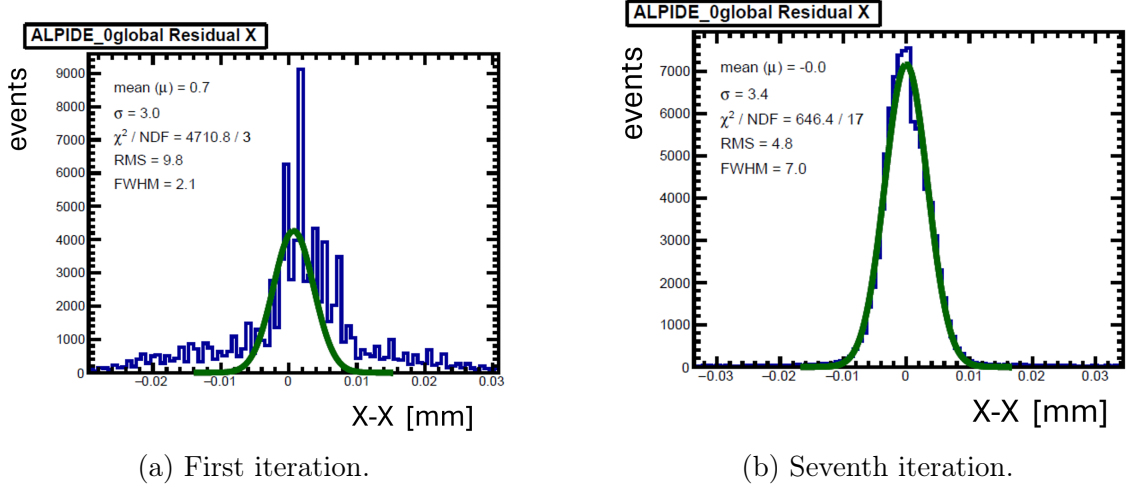


Figure 6.8: Residuals of the reference planes during the alignment of the telescope.

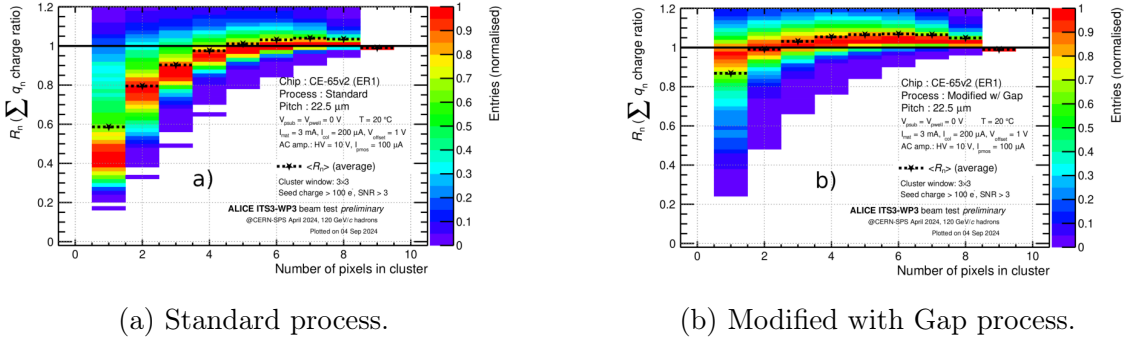


Figure 6.9: Accumulated charge ratio as a function of the number of pixels in a 3 \times 3 matrix around a seed pixel. From Reference [63].

lower thresholds, the signal-to-noise ratio would be very low. For an example of the noise distribution for the Modified with Gap process chip of 15 μm with 4 V applied bias voltage, see Figure 6.10. The thresholds were converted from ADC to electrons using the calibration factors determined in Chapter 5.

Shown in Figure 6.11a is the study of the global efficiency as a function of electron thresholds for the Standard process. All four pitch and reverse bias combinations yield efficiencies greater than 99% for thresholds up to $\sim 150e^-$ and $\sim 130e^-$ for the 15 μm and 22.5 μm respectively. In Figure 6.11b, the global efficiency as a function of electron thresholds for the Modified with Gap process is shown. An efficiency of over 99% is achieved up to much higher thresholds for all four pitch and reverse bias combinations in this process. For both pitch sizes, this efficiency is achieved up to $\sim 180e^-$. The drop in efficiency in the Standard process variants is steeper than in the Modified with Gap variants, which is as expected, as the Standard process loses seed charge through charge sharing, making it harder for an event to surpass the seed charge threshold. In the Standard process variant, the sensor performs better when a reverse bias voltage of 10 V is applied compared to 4 V, indicating an increased

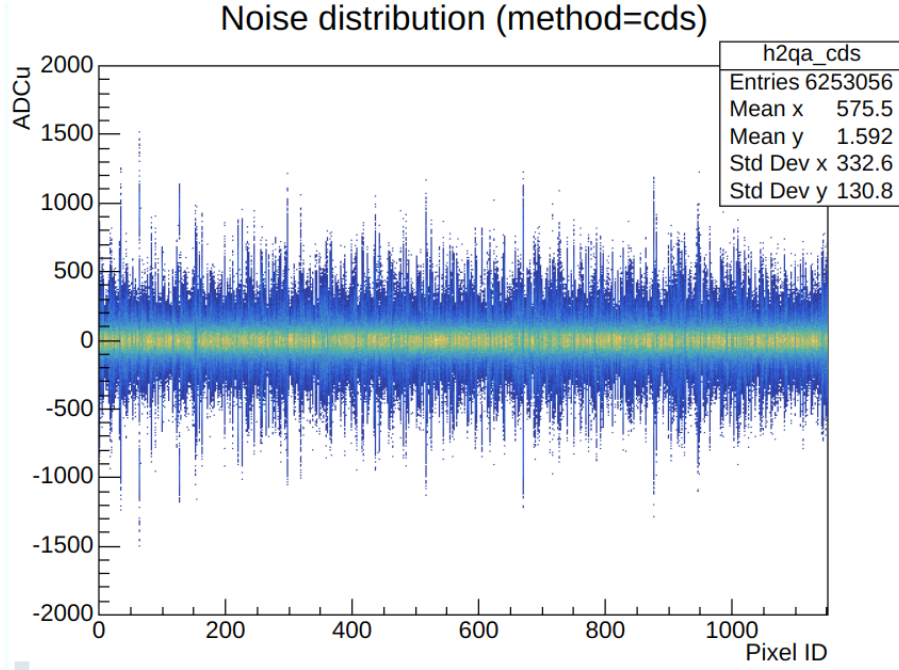
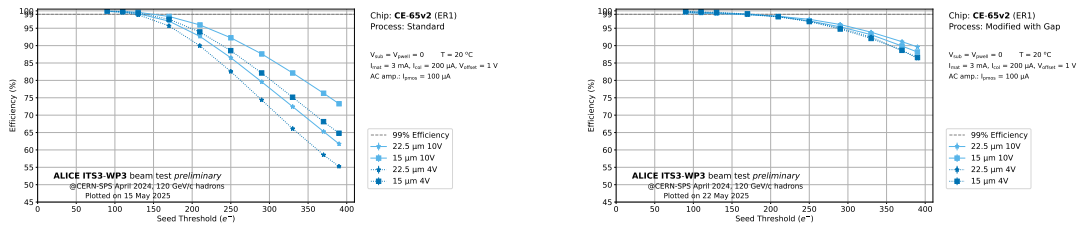


Figure 6.10: Noise distribution of Modified with Gap process chip of $15\mu\text{m}$ with 4 V applied bias voltage. The standard deviation of the noise in ADU is given in the right-hand box. This was the baseline value used to calculate the first threshold evaluated per measurement.

depleted zone. While in the Modified with Gap process, the different pixel pitches perform nearly equally well, in the Standard process, a significant improvement of the $15\mu\text{m}$ compared to the $22.5\mu\text{m}$ pitch size can be observed. This is expected, as the undepleted region at the pixel boundaries is greater for the larger pitch size. In the Modified with Gap process, the depleted zone ranges over the whole pixel pitch in both cases. Accordingly, the $22.5\mu\text{m}$ pitch sensors perform slightly better than their smaller-pitched counterparts.



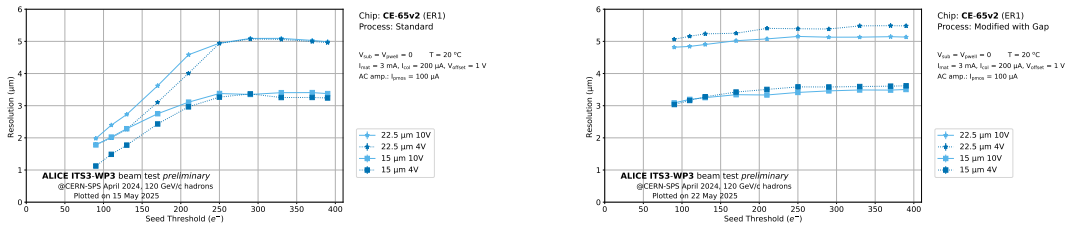
(a) global efficiency for the Standard process. (b) global efficiency for the Modified with Gap process.

Figure 6.11: Detection efficiencies.

The spatial resolution of the chip variants was likewise studied for the CE-65 sensors at different bias voltages with respect to increasing electron threshold, while subtracting in quadrature the value of the telescope resolution. In Figure 6.12a, the spatial resolutions for the Standard process chips are shown for all four combinations

of pitch sizes and reverse bias voltages. For all combinations, excellent resolutions can be achieved. For the larger pitch size of $22.5\text{ }\mu\text{m}$, the requirement of $3\text{ }\mu\text{m}$ is undercut up to a limit of $\sim 140e^-$ or $\sim 150e^-$ for a reverse bias voltage of 4 V or 10 V respectively. For the smaller counterpart, the requirement is undercut up to even higher limits of $\sim 200e^-$ for both bias voltages. The performance degrades quickly below $250e^-$ as the cluster size decreases. At this level, it plateaus at $\sim 5\text{ }\mu\text{m}$ and below $3.5\text{ }\mu\text{m}$ for the larger and the smaller pitch size, respectively. The binary resolution of pitch size / $\sqrt{12}$ lies at $6.5\text{ }\mu\text{m}$ for the larger pitch size and $4.3\text{ }\mu\text{m}$ for the smaller sensor and is surpassed in both cases for all tested thresholds.

In Figure 6.12b, the global spatial resolution of all four combinations of pitch size and reverse bias voltage for the Modified with Gap process chips is shown. This process variant achieves a worse resolution than the Standard process, as charge-sharing effects are reduced. However, as charge sharing is not completely negligible, also for this process, the binary resolution is surpassed in all four combinations for all thresholds, as the $22.5\text{ }\mu\text{m}$ chip displays resolutions of just above $5\text{ }\mu\text{m}$, while the $15\text{ }\mu\text{m}$ chip plateaus at $\sim 3.5\text{ }\mu\text{m}$ for see charge thresholds above $\sim 150e^-$. The Modified with Gap process variant displays less variation with increasing thresholds, but both chip variants perform comparably well at high thresholds. Comparing the reverse bias voltages, the Standard process shows a significant improvement when a reverse bias of 4 V is applied. This effect probably comes from the depletion depth being influenced by the applied bias voltage. As the Modified with Gap process chip features full depletion in any case, it might not be significantly influenced by a change in the bias voltage. In contrast, the balloon-shaped depleted region in the Standard process might be adjusted according to the applied voltage. The bias voltage does not significantly influence the performance of this process variant.



(a) global spatial resolution of Standard process. (b) global spatial resolution of Modified with Gap process.

Figure 6.12: Global spatial resolution studies.

The global efficiency for the Modified with Gap process falls below 99% for seed charge thresholds of 165 ADU (168 ADU) for a pitch size of $22.5\text{ }\mu\text{m}$ ($15\text{ }\mu\text{m}$), applying a reversed bias of 4 V and 156 ADU (170 ADU) for the larger (smaller) pitch size with a reversed bias of 10 V.

The global efficiency for the Standard process variant falls below the threshold of 99 % at 120 ADU (138 ADU) for a pitch size of $22.5\text{ }\mu\text{m}$ ($15\text{ }\mu\text{m}$), when a reversed bias of 4 V is applied. With a reversed bias of 10 V, it falls below 99% at 136 ADU (152 ADU) for the larger (smaller) pitch size.

6.4.2 In-pixel efficiency and spatial resolution

The CE-65 features a large pixel matrix, which can be utilised to perform in-pixel studies. From the large number of collected and reconstructed tracks, the hit information of every pixel, not belonging to the two outermost columns/rows, is superimposed and analysed. For the in-pixel studies, the “cluster” method with a seed and neighbour threshold of $170e^-$ is used to compare the in-pixel with the global studies. Additionally, to see the effect of the charge sharing in the Standard process variants, the “window” method was applied for the spatial resolution studies. Studying the efficiency inside the pixels, we see areas within the pixel where detection efficiency losses occur. The spatial resolution measured inside a pixel can give insights into charge sharing properties of a process variant and, as such, is expected to reflect the excellent resolution of the Standard process chips. For both processes, data from the smaller $15\mu\text{m}$ pitch size sensor is used, and a reverse bias voltage of 10 V was selected. The left-hand side plots of the in-pixel study figures in this subsection represent the averaged pixel divided into multiple bins. For each bin, the detection efficiency/ spatial resolution is determined and represented by the colour shade. The right-hand side of the plot illustrates the variation in detection efficiency, resp. spatial resolution along different paths. The blue line represents the straight path from the middle of the pixel to the (upper) edge, the orange path leads along the edge of the pixel from the middle to the upper right corner, and the green line is the path from this corner again to the middle of the pixel. The resolution and distance along the path are given in μm while the detection efficiency is given in percent. The diagonal path in the in-pixel efficiency plots marks the corresponding global efficiency, according to the results shown in the previous subsection. The in-pixel efficiency study of the Standard process, analysed using the “cluster” method, is shown in Figure 6.13. The performance shows a significant dip at the corners, which comes from charge-sharing effects. For a hit, recorded at the edge of a Standard process pixel, the hit information is shared between the closest neighbour pixels and, therefore, often does not exceed the seed threshold.

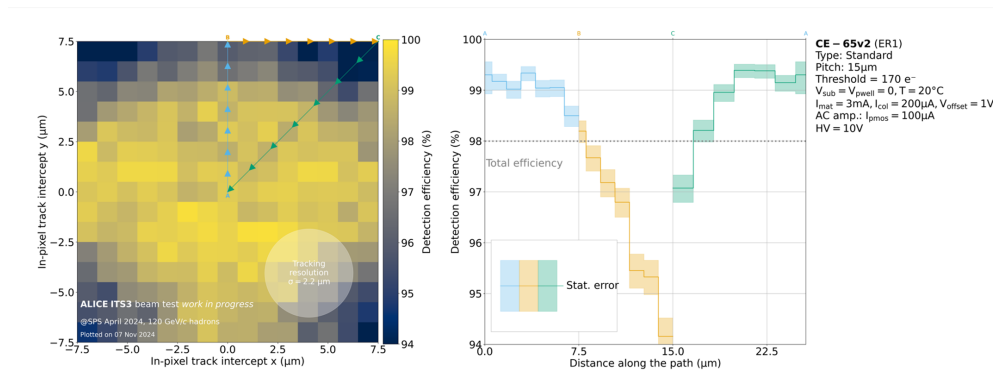


Figure 6.13: In-Pixel efficiency study for the Standard process variant. The clustering method “cluster” was used.

In figure Figure 6.14, the in-pixel efficiency study of the Modified with Gap pro-

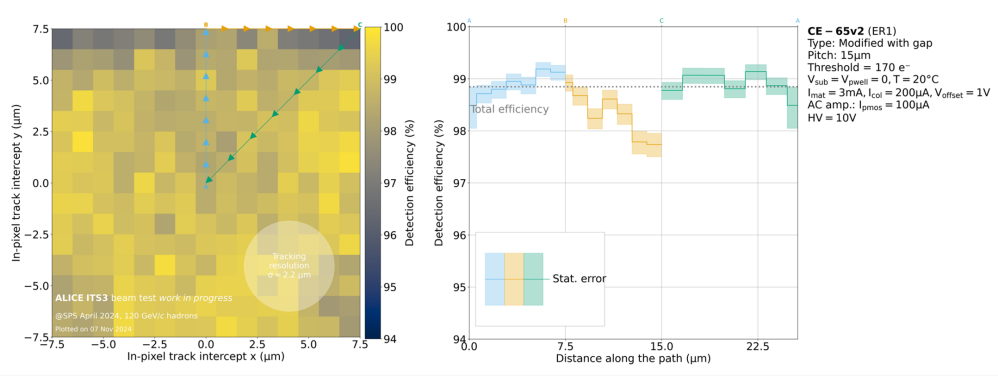
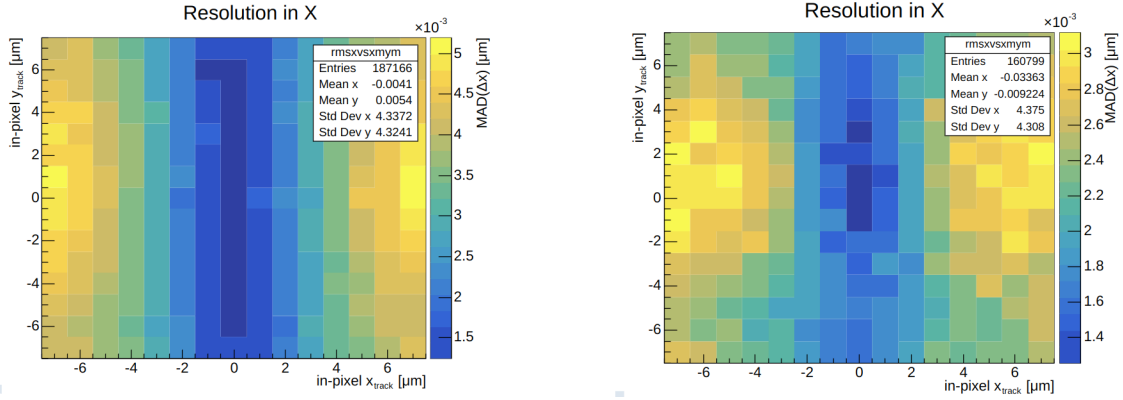


Figure 6.14: In-Pixel efficiency study for the Modified with Gap process variant. The clustering method “cluster” was used.

cess is shown. For the Modified with Gap process, the observed drop in the efficiency is only a minor effect compared to the Standard process. The detection efficiency is much more uniformly distributed over the pixel size, reflecting the better global efficiency of the Modified with Gap process. This distribution shows the effect of the depletion, which allows the charge collection to reach the edges and corners of the pixel.

For the in-pixel study of the spatial resolution, the mean absolute deviation between the reconstructed telescope and DUT cluster position ($\sqrt{\Delta x^2 + \Delta y^2}$) is shown. This differs from the previously stated global resolution, which was the average standard deviation of the residuals in the x and y directions. This way to calculate the resolution is the Taylor expansion of $\sqrt{\Delta x^2 + \Delta y^2}$. However, the resolution per bin in X and Y is very different for the in-pixel studies. To get a reliable quantity, the Taylor expansion is not suitable in this context. This is why the precise deviation is calculated in the in-pixel study to get the resolution. In Figure 6.15, the resolutions in X are shown. Note that per bin, these resolutions are significantly different. Another effect, which can be observed, comes from the different process variants. While the Modified with Gap process variant performs uniformly well over the whole pixel pitch, the resolution at the edges of the Standard process pixel is smaller than for the Modified with Gap process variant. This effect is supported by the use of the “window” clustering method.

Figure 6.16 shows the in-pixel spatial resolution study of the Standard process, where the “cluster” method was used in the analysis. Starting on the right-hand side plot with an excellent resolution in the centre of the pixel, the performance drops rapidly following the path towards the upper edge of the pixel. The highest resolution value slightly above $\sim 6 \mu\text{m}$ is measured at the corner. This resolution outranges the binary resolution of $\sim 4.3 \mu\text{m}$ for a pitch size of $15 \mu\text{m}$ and is influenced mainly by the missing hit information due to charge sharing and a high neighbour threshold. This influence can be minimised by applying the “window” method. Figure 6.17 shows the in-pixel spatial resolution of the Standard process, using the “window” method in the analysis. Here, the tendency of better resolution in the centre than the edges is also visible, but the resolution in the pixel corner only rises



(a) Resolution in X for the Modified with Gap process variant.

(b) Resolution in X for the Standard process variant.

Figure 6.15: Resolution in X for the Standard and the Modified with Gap process variant with $15\mu\text{m}$ pitch size. The analysis was made using the clusterisation method “window”. Note the significant standard deviations for both processes.

to $\sim 3.5\mu\text{m}$ and therefore does not improve upon the binary resolution. Also, the distribution of the performance throughout the chip is much more uniform than in Figure 6.16.

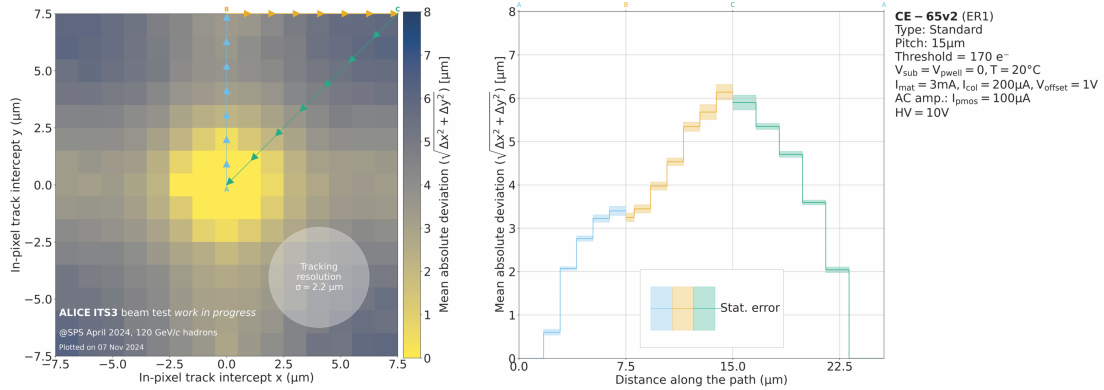


Figure 6.16: In-Pixel resolution study for the Standard process variant. The clustering method “cluster” was used.

For the Modified with Gap process, the in-pixel spatial resolution, analysed using the “cluster” method, is shown in Figure 6.18. Starting again in the middle of the pixel, the resolution is also excellent, but it rises even more sharply, peaking at a resolution of over $7.5\mu\text{m}$ at the corner. This resolution overshoots the binary resolution even more than the Standard process, mainly because the Modified with Gap process has nearly no charge-sharing opportunity. Therefore, applying the “window” method for this process is not expected to improve the resolution as much as in the Standard process. This is also reflected in the overall worse spatial resolution observed before. In Figure 6.19, the results of using the window method in the analysis are shown. The performance at the edges and corners has slightly improved using

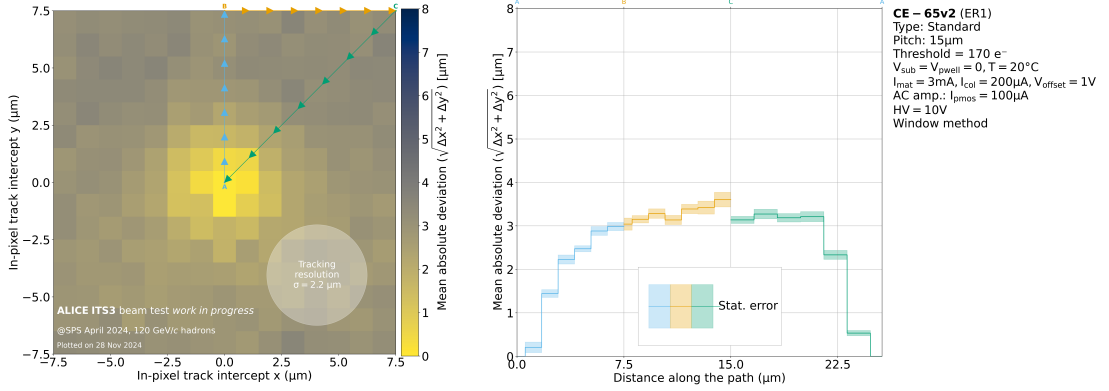


Figure 6.17: In-Pixel resolution study for the Standard process variant. The clustering method “window” was used.

the window method and does not exceed a spatial resolution of $\sim 6.5\mu\text{m}$, however, this is still worse than the binary resolution.

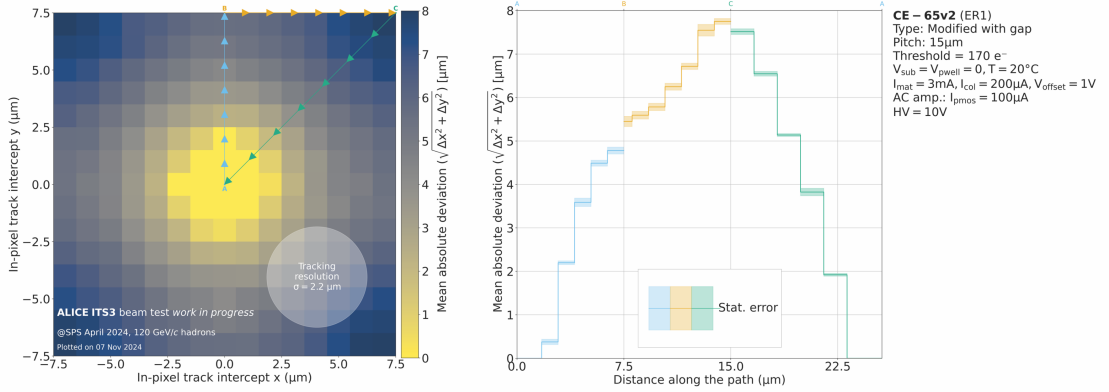


Figure 6.18: In-Pixel resolution study for the Modified with Gap process variant. The clustering method “cluster” was used.

The “window” method shows clearly the advantage of the Standard process over the Modified with Gap process. Charge sharing from the seed to the neighbouring pixels strongly helps reconstruct the precise hit position inside the pixel and reach resolutions much below the binary resolution.

In the **in-pixel** study, the reason for these differences between the process variants can be confirmed, as the Standard process variant performs much better than the Modified with Gap variant in the spatial resolution, especially when allowing the 3×3 neighbouring pixels to be read out with a neighbouring threshold of zero. The charge sharing in the Standard process makes it possible to have a very good spatial resolution throughout the pixel, especially at the edges and corners, compared to the Modified with Gap variant. For the in-pixel study of the detection efficiency, the performance of the Modified with Gap process variant is significantly more uniformly distributed over the pixel than for the Standard process. This comes mainly

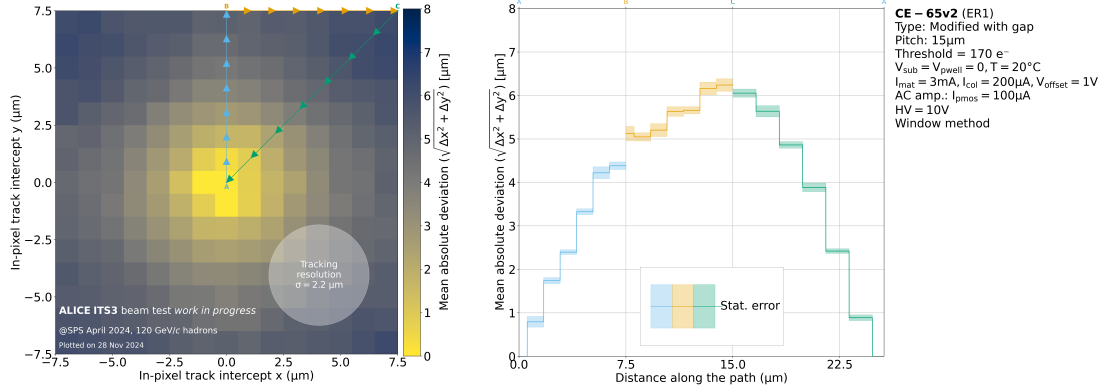


Figure 6.19: In-Pixel resolution study for the Modified with Gap process variant. The clustering method “window” was used.

from the depletion of the sensors, which reach the edges and corners of the Modified with Gap process sensors. In case of the Standard process sensors, the depletion doesn’t reach the edges of the pixel, leading to a significant drop in the performance of the Standard process sensors at the edges, which is also reflected in the worse global performance for this variant.

For completeness reasons, the in-pixel detection efficiency study was performed using the “window” clusterisation method to detect the efficiency. Furthermore, the analysis was also conducted for the larger pixel pitch sizes of 22.5 μm. The effects and tendencies shown in this chapter are also applicable to these results, which is why they are not discussed here. These results can be found in the Appendix.

6.5 Summary

The characterisation in the test beam at SPS showed the very good performance of the Standard process variant, yielding global spatial resolutions of below 2.5 μm, after the telescope resolution was subtracted. This resolution is achieved using the smaller pitch size of 15 μm, still operating with over 99 % efficiency and at thresholds above 130 electrons. For the larger pitch size of 22.5 μm, a global spatial resolution of < 3 μm was achieved, operating with over 99 % efficiency at thresholds above 130 electrons. For the global efficiency, the larger pitch size performs better, and the chip performs better when a reversed bias of 10 V is applied.

The Modified with Gap process, featuring faster charge collection but less charge sharing, enables resolutions of ~3.3 μm. A future reduction of the pixel pitch size for this process could also allow the Modified with Gap process variant to undercut the required 3 μm. For the global efficiency, the sensor achieves slightly better results for the larger pitch size of 22.5 μm and performs better when a reversed bias of 10 V is applied.

Studying the in-pixel performance of the chip variants, the results of the global studies are extended. The Standard process variant, performing much better in the global spatial resolution, allows for charge sharing between neighbouring pixels.

This makes it possible to have a very good spatial resolution, especially at the edges and corners of the pixel. However, the detection efficiency at the edges and corners is limited due to the partial depletion of the Standard sensor. The full depletion of the Modified with Gap sensor allows for a very good charge collection at the edges and in the corners, making detection more efficient.

Conclusions

The Standard Model, while being an elegant model to describe matter and most of the forces in our Universe, leaves many questions unanswered. A new particle collider is needed to study these, focusing on the high-precision study of the Higgs boson. As a successor of the LHC at CERN, many different future collider projects are proposed, one of them being the FCC. This versatile project makes it possible to study in the first phase already much more than solely the Higgs boson, as it offers the possibility to inspect, for example, the electroweak interaction as well as flavour physics parameters in great detail. Until the first collisions can be recorded in the FCC-ee, many steps still have to be taken, as shown in Figure 6.20. This March, the FCC feasibility study report was finished and published. After the potential approval of the FCC in ~ 2028 , the focus will shift more and more towards developing and building accelerator and detector prototype components. The anticipated start of the detector installation will be in ~ 2041 , with the detector commissioning starting in ~ 2045 to enable the start of the FCC-ee physics programme soon after.

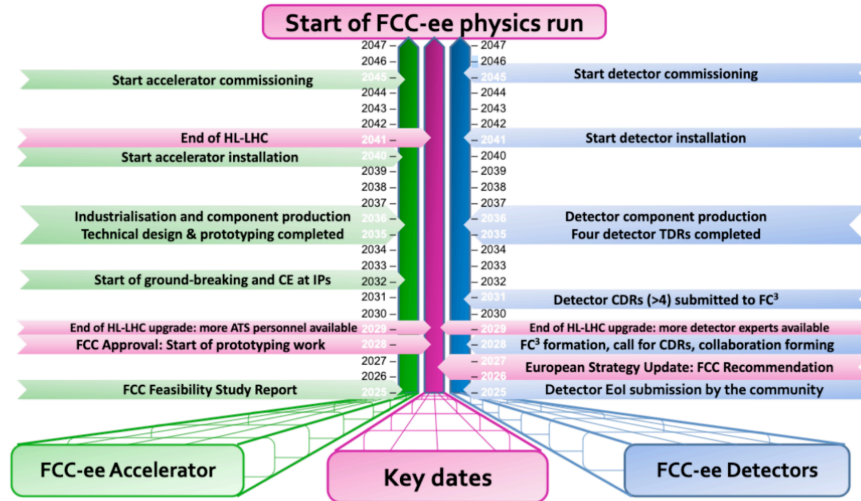


Figure 6.20: Preliminary FCC-ee timeline. From Reference [74].

These endeavours follow a long timeline, which already benefits from ongoing research in detector developments. The optimal prerequisite for this is to have an already existing experiment with similar requirements to one of their detector parts. For the sensors which could be used in the vertex detector, such an experiment

is the ALICE experiment at CERN. The developments on MAPS, which they are advancing for the update of their inner tracking system (ITS3), are very interesting for the R&D for FCC-ee vertex detectors. In the scope of the research for the ALICE ITS3, small-scale test structures were developed. Among them was the CE-65 sensor and its evolution, the CE-65v2.

This thesis evaluated the feasibility of reaching the FCC-ee vertex detector requirements using a 65 nm CMOS process sensor deployed in the CE-65v2 prototype chip. A special focus lay on the spatial resolution requirement of $3\text{ }\mu\text{m}$ while the chip still runs with a detection efficiency of at least 99%. The results shown here built on studies of the CE-65v1 and CE-65v2, found in Reference [63]. Within the scope of this thesis, four variants of the CE-65v2 were characterised, investigating the impact of different pixel pitches and manufacturing processes on the performance of the sensors. Furthermore, the sensors were operated at reverse bias voltages of 4 V and 10 V, adding a third exploration axis. The characterisation consisted of measurements of the calibration factor with a radioactive source in the lab at the University of Zurich and of tests in a real but controlled environment at the CERN SPS and at DESY II test beam facilities.

The test beam characterisation of the Standard process variant yielded resolutions of below $2.5\text{ }\mu\text{m}$ (below $3\text{ }\mu\text{m}$) for the pitch size of $15\text{ }\mu\text{m}$ ($22.5\text{ }\mu\text{m}$), after the telescope resolution was subtracted. These resolutions were achieved while still operating with over 99% efficiency and above a seed charge threshold of 130 electrons. The GAP process, featuring faster charge collection but less charge sharing, enables resolutions of $\sim 3.3\text{ }\mu\text{m}$. This value could be reduced when reducing the pitch size of the GAP process. In-pixel performance studies extended the results obtained in global studies. In the Standard process variant, the charge-sharing effect could be observed. In the spatial resolution, this allowed for very good performance, especially at the edges and corners of the pixel, while the detection efficiency performance decreased in these regions. In the Modified with Gap process variant, the contrary effect was visible by having a very good detection efficiency in the edges and corners, but a significant dip in the resolution in these areas.

In summary, it was concluded that the challenges in achieving the required resolution in semiconductor sensors with an analogue readout, while maintaining a good efficiency at reasonable noise levels, differ between the two chip process variants. In the Standard process, the challenges include the complex design of the analogue-to-digital conversion scheme to fully benefit from the charge sharing information. In a real detector environment, it is impossible to read out all the neighbouring pixels with a zero threshold. The main challenge for the Modified with Gap process is integrating all the necessary logic into the pixels while minimising the pitch size to reach the required $3\text{ }\mu\text{m}$ resolution. The results obtained in the scope of this thesis were presented at the Eleventh International Workshop for Semiconductor Pixel Detectors for Particles and Imaging 2024 (link to the contribution on indico¹) and were published as a conference proceeding [75].

To complete the characterisation of the CE-65v2 chip, a test beam is planned for June 2025, in which the impact of a staggered pixel arrangement, as well as the

¹<https://indico.in2p3.fr/event/32425/contributions/142771/>

intermediate process variant “Modified” will be tested. In the Modified process variant, there are no gaps in the n-type implant, while the depletion still reaches the edges of the pixel. The full analysis of the CE-65v2 chips also include studies of the 18 μm pitch size and the analysis of the data taken at the test beam in DESY, studying the effect of irradiation on the different chip variants.

The studies of the CE-65v2 chip has supplemented the APTS [66] and DPTS [71] studies, validating the 65 nm TPSCo CMOS process as a candidate technology for future particle detection applications.

Guided by the ECFA R&D roadmap [76], eight detector R&D collaborations have formed to develop detector technologies towards fulfilling all the requirements of future collider physics experiments. One of the collaborations is the Solid State Detectors R&D Collaboration (DRD3 [77]). This collaboration aims to improve, among others, the monolithic sensing technology, aiming to advance the performance of monolithic CMOS. The OCTOPUS² project within DRD3 is concerned with developing MAPS, from the ASIC design to simulation, and characterisation. The goal is to target the general vertex-detector requirements of future lepton colliders, as outlined in the ECFA detector R&D roadmap [78, 79].

The results in this thesis mark a promising step towards developing sensors for FCC-ee vertex detectors and are a starting point for projects like OCTOPUS.

²<https://octopus.web.cern.ch/>

Bibliography

- ¹G. Aad et al., “Observation of a new particle in the search for the standard model higgs boson with the ATLAS detector at the LHC”, *Physics Letters B* **716**, 1–29 (2012).
- ²S. Chatrchyan et al., “Observation of a new boson at a mass of 125 GeV with the CMS experiment at the LHC”, *Physics Letters B* **716**, 30–61 (2012).
- ³Burgard, *Standard model of physics – TeXample.net*, (Dec. 31, 2016) <https://texample.net/model-physics/> (visited on 04/07/2025).
- ⁴S. L. Glashow, “The renormalizability of vector meson interactions”, *Nuclear Physics* **10**, 107–117 (1959).
- ⁵S. L. Glashow, “Partial-symmetries of weak interactions”, *Nuclear Physics* **22**, 579–588 (1961).
- ⁶A. Salam and J. C. Ward, “Weak and electromagnetic interactions”, *Il Nuovo Cimento* (1955-1965) **11**, 568–577 (1959).
- ⁷S. Weinberg, “A model of leptons”, *Physical Review Letters* **19**, 1264–1266 (1967).
- ⁸P. W. Higgs, “Broken symmetries, massless particles and gauge fields”, *Physics Letters* **12**, 132–133 (1964).
- ⁹P. W. Higgs, “Broken symmetries and the masses of gauge bosons”, *Physical Review Letters* **13**, 508–509 (1964).
- ¹⁰P. W. Higgs, “Spontaneous symmetry breakdown without massless bosons”, *Phys. Rev.* **145**, 1156–1163 (1966).
- ¹¹F. Englert and R. Brout, “Broken symmetry and the mass of gauge vector mesons”, *Physical Review Letters* **13**, 321–323 (1964).
- ¹²G. S. Guralnik, C. R. Hagen, and T. W. B. Kibble, “Global conservation laws and massless particles”, *Physical Review Letters* **13**, 585–587 (1964).
- ¹³T. W. B. Kibble, “Symmetry breaking in nonAbelian gauge theories”, *Phys. Rev.* **155**, edited by J. C. Taylor, 1554–1561 (1967).
- ¹⁴V. Ciochia, G. Dissertori, and T. Gehrmann, *Phenomenology of particle physics*, Nov. 14, 2010.
- ¹⁵E. Locci, “Precision electroweak measurements at FCC-ee”, *PoS EPS-HEP2019*, 638 (2020).
- ¹⁶N. Cabibbo, “Unitary symmetry and leptonic decays”, *Phys. Rev. Lett.* **10**, 531–533 (1963).

- ¹⁷M. Kobayashi and T. Maskawa, “CP-violation in the renormalizable theory of weak interaction”, *Progress of Theoretical Physics* **49**, 652–657 (1973).
- ¹⁸A. Ceccucci, Z. Ligeti, and Y. Sakai, *Particle data group*, Particle Data Group, <https://pdg.lbl.gov/2023/> (visited on 02/20/2025).
- ¹⁹P. Azzi, “Physics requirements on vertex detectors performance”, (2024).
- ²⁰P. Azzi, *MAPS detectors technologies for the FCC-ee vertex detector*, Indico, (July 1, 2024) <https://indico.cern.ch/event/1417976/timetable/> (visited on 08/15/2024).
- ²¹O. Brüning, P. Collier, P. Lebrun, S. Myers, R. Ostojic, J. Poole, and P. Proudlock, *LHC design report*, CERN Document Server, (2004) <https://cds.cern.ch/record/782076> (visited on 04/08/2025).
- ²²CERN, *And they’re off! the 2025 LHC physics season gets underway*, CERN, (June 6, 2025) <https://home.cern/news/news/accelerators/and-theyre-2025-lhc-physics-season-gets-underway> (visited on 06/20/2025).
- ²³M. Benedikt et al., *Future circular collider feasibility study report volume 1: physics and experiments*, edited by M. Benedikt, 2025.
- ²⁴A. bibinitperiod C. Collaboration, *Input to the european strategy for particle physics - 2026 update*, Indico, <https://indico.cern.ch/event/1439855/contributions/6461580/> (visited on 05/12/2025).
- ²⁵S. Navas et al., “Review of particle physics”, *Physical Review D* **110**, 030001 (2024).
- ²⁶R. Aaij et al., “Measurement of CP violation and the B_s^0 meson decay width difference with $B_s^0 \rightarrow J/\psi K^+ K^-$ and $B_s^0 \rightarrow J/\psi \pi^+ \pi^-$ decays”, *Physical Review D* **87**, 112010 (2013).
- ²⁷X. Zuo, “Measurement of top quark CKM elements at FCC-ee 2025.04.01”,
- ²⁸X. Zuo, S. Alshamaily, M. Klute, and M. Presilla, “Top quark CKM and EWK couplings 2024.10.09”,
- ²⁹S. Monteil, “|vcb|: the WW threshold to fix at FCC-ee a longstanding question”, (2024).
- ³⁰S. Monteil and G. Wilkinson, “Heavy-quark opportunities and challenges at FCC-ee”, *The European Physical Journal Plus* **136**, 837 (2021).
- ³¹L. LHCb Collaboration et al., *Physics case for an LHCb upgrade II - opportunities in flavour physics, and beyond, in the HL-LHC era*, Apr. 5, 2019.
- ³²J. Charles, A. Hocker, H. Lacker, S. Laplace, F. R. L. Diberder, J. Malcles, J. Ocariz, M. Pivk, and L. Roos, “CP violation and the CKM matrix: assessing the impact of the asymmetric b factories”, *The European Physical Journal C* **41**, 1–131 (2005).
- ³³J. Kamenik, *5th FCC physics workshop*, Indico, <https://indico.cern.ch/event/1066234/contributions/4721138/> (visited on 04/16/2025).
- ³⁴C. Adolphsen et al., *The international linear collider technical design report - volume 3.II: accelerator baseline design*, June 26, 2013.

- ³⁵L. Linssen, A. Miyamoto, M. Stanitzki, H. Weerts, and L. Linssen, *Physics and detectors at CLIC: CLIC conceptual design report* (CERN, Geneva, 2012).
- ³⁶P. Lebrun, L. Linssen, A. Lucaci-Timoce, D. Schulte, F. Simon, S. Stapnes, N. Toge, H. Weerts, and J. Wells, “The CLIC programme: towards a staged e+e- linear collider exploring the terascale : CLIC conceptual design report”, [10.5170/CERN-2012-005](https://cds.cern.ch/record/1305170/files/CLIC-CDR-2012-005.pdf) (2012).
- ³⁷M. Benedikt et al., *Future circular collider feasibility study report volume 2: accelerators, technical infrastructure and safety*, edited by M. Benedikt, 2025.
- ³⁸CERN, *FCC study media kit 2024*, CERN, (Jan. 30, 2025) <https://home.cern/science/cern/fcc-study-media-kit-2024> (visited on 02/21/2025).
- ³⁹I. Agapov et al., *Future circular lepton collider FCC-ee: overview and status*, Mar. 15, 2022.
- ⁴⁰K. Jakobs and M. Vos, “L international meeting on fundamental physics and XV CPAN days”, in (Oct. 6, 2023).
- ⁴¹T. I. S. The IDEA Study Group, *The IDEA detector concept for FCC-ee*, Mar. 10, 2025.
- ⁴²J. Pekkanen, “ALLEGRO FCC-ee detector concept & noble liquid calorimetry”, *Nuclear Instruments and Methods in Physics Research Section A: Accelerators, Spectrometers, Detectors and Associated Equipment* **1069**, 169921 (2024).
- ⁴³N. Bacchetta et al., *CLD – a detector concept for the FCC-ee*, Dec. 12, 2019.
- ⁴⁴U. Einhaus, *The international large detector (ILD) for a future electron-positron collider: status and plans*, Nov. 15, 2023.
- ⁴⁵A. Ilg, A. Macchiolo, and F. Palla, *The vertexing challenge at FCC-ee*, Feb. 7, 2025.
- ⁴⁶A. Besson and J. Baudot, “The ILC vertex project and general requirements for future e+e- colliders”, in (2024).
- ⁴⁷M. Thomson, *Modern particle physics*, 7th printing (2021) (Cambridge university press, Cambridge, 2013).
- ⁴⁸D. E. Groom and S. R. Klein, “Passage of particles through matter”, *The European Physical Journal C* **15**, 163–173 (2000).
- ⁴⁹S. Tavernier, *Experimental techniques in nuclear and particle physics* (Springer, Heidelberg ; New York, 2010).
- ⁵⁰C. Adler, “Radiation length of the ALICE TRD”, (2006).
- ⁵¹G. Pellegrini et al., “Technology developments and first measurements of low gain avalanche detectors (LGAD) for high energy physics applications”, *Nuclear Instruments and Methods in Physics Research Section A: Accelerators, Spectrometers, Detectors and Associated Equipment*, HSTD-9 2013 - Proceedings of the 9th International "Hiroshima" Symposium on Development and Application of Semiconductor Tracking Detectors **765**, 12–16 (2014).
- ⁵²H. Kolanoski and N. Wermes, *Teilchendetektoren: Grundlagen und Anwendungen*, 1. Aufl. 2016 (Springer Berlin Heidelberg, Berlin, Heidelberg, 2016).

- ⁵³D. Barney, *CMS detector slice - CMS collection*, (2016) <https://cds.cern.ch/record/2120661/> (visited on 03/27/2025).
- ⁵⁴M. Moll, “Radiation damage in silicon particle detectors: microscopic defects and macroscopic properties”, PhD thesis (Hamburg U., 1999).
- ⁵⁵The Noise, *P-n junction*, in *Wikipedia* (Dec. 23, 2024).
- ⁵⁶M. Mager, “ALPIDE, the monolithic active pixel sensor for the ALICE ITS upgrade”, *Nuclear Instruments and Methods in Physics Research Section A: Accelerators, Spectrometers, Detectors and Associated Equipment, Frontier Detectors for Frontier Physics: Proceedings of the 13th Pisa Meeting on Advanced Detectors* **824**, 434–438 (2016).
- ⁵⁷A. S. Triolo, *Calibration and performance of the upgraded ALICE inner tracking system*, Sept. 29, 2024.
- ⁵⁸A. Collaboration, “ALICE upgrades during the LHC long shutdown 2”, *Journal of Instrumentation* **19**, P05062 (2024).
- ⁵⁹A. collaboration, *Technical design report for the ALICE inner tracking system 3 - ITS3 ; a bent wafer-scale monolithic pixel detector*, 2024.
- ⁶⁰M. Lamont, *Updated schedule for CERN’s accelerators*, CERN, (Feb. 26, 2025) <https://home.cern/news/opinion/accelerators/updated-schedule-cerns-accelerators> (visited on 03/04/2025).
- ⁶¹C.-Z. Wang, *The ITS3 detector and physics reach of the LS3 ALICE upgrade*, Sept. 3, 2024.
- ⁶²Tower Partners Semiconductor Co., Ltd., *TPSCo overview and history - tower semiconductor*, (Apr. 7, 2021) <https://towersemi.com/tpsco/> (visited on 05/21/2025).
- ⁶³E. Ploerer et al., “Characterisation of analogue MAPS produced in the 65 nm TPSCo process”, *Journal of Instrumentation* **20**, C01019 (2025).
- ⁶⁴M. Buckland, “First measurements with monolithic active pixel test structures produced in a 65 nm CMOS process”, *Journal of Instrumentation* **19**, C02017 (2024).
- ⁶⁵W. Snoeys et al., “A process modification for CMOS monolithic active pixel sensors for enhanced depletion, timing performance and radiation tolerance”, *Nuclear Instruments and Methods in Physics Research Section A: Accelerators, Spectrometers, Detectors and Associated Equipment* **871**, 90–96 (2017).
- ⁶⁶G. A. Rinella et al., *Characterisation of analogue monolithic active pixel sensor test structures implemented in a 65 nm CMOS imaging process*, Mar. 13, 2024.
- ⁶⁷M. Suljic, “Study of monolithic active pixel sensors for the upgrade of the ALICE inner tracking system”, PhD thesis (Trieste U., 2017).
- ⁶⁸D. Banerjee, J. Bernhard, M. Brugger, N. Charitonidis, N. Doble, L. Gatignon, and A. Gerbershagen, *The north experimental area at the cern super proton synchrotron*, 2021.

- ⁶⁹R. Diener et al., “The DESY II test beam facility”, *Nuclear Instruments and Methods in Physics Research Section A: Accelerators, Spectrometers, Detectors and Associated Equipment* **922**, 265–286 (2019).
- ⁷⁰M. Mager, *The telescope optimiser*, <https://mmager.web.cern.ch/telescope/tracking.html> (visited on 04/23/2025).
- ⁷¹G. Rinella et al., “Digital pixel test structures implemented in a 65 nm CMOS process”, *Nuclear Instruments and Methods in Physics Research Section A: Accelerators, Spectrometers, Detectors and Associated Equipment* **1056**, 168589 (2023).
- ⁷²D. Dannheim et al., “Corryvreckan: a modular 4d track reconstruction and analysis software for test beam data”, *Journal of Instrumentation* **16**, P03008 (2021).
- ⁷³V. Blobel, “Software alignment for tracking detectors”, *Nuclear Instruments and Methods in Physics Research Section A: Accelerators, Spectrometers, Detectors and Associated Equipment*, TIME 2005 **566**, 5–13 (2006).
- ⁷⁴F. Sefkow, *Third annual US higgs factory future circular collider workshop*, INDICO-FNAL (Indico), (Apr. 15, 2025) <https://indico.fnal.gov/event/67484/contributions/310850/> (visited on 04/17/2025).
- ⁷⁵A. Lorenzetti et al., “Performance studies of the CE-65v2 MAPS prototype structure”, [10.1088/1748-0221/20/03/C03033](https://doi.org/10.1088/1748-0221/20/03/C03033) (2025).
- ⁷⁶A. Robson and C. Leonidopoulos, “ECFA higgs/electroweak/top factory study”, <https://doi.org/10.23731/CYRM-2025-005> (2025).
- ⁷⁷CERN, *Experiment’s detail*, <https://greybook.cern.ch/experiment/detail?id=DRD3> (visited on 05/13/2025).
- ⁷⁸CERN, *DRD3 WG1 OCTOPUS*, <https://octopus.web.cern.ch/> (visited on 02/21/2025).
- ⁷⁹E. Vilella, *The 2024 international workshop on the high energy circular electron positron collider*, Indico of IHEP (Indico), (Oct. 24, 2024) <https://indico.ihep.ac.cn/event/22089/contributions/168821/> (visited on 02/21/2025).

Appendix

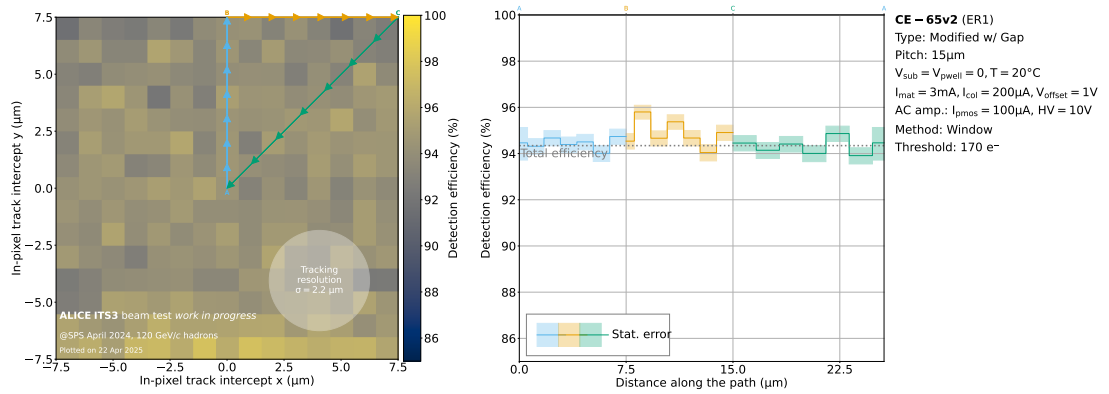


Figure 6.21: In-pixel efficiency of Modified with Gap process sensor with 15 μm pitch size. Analysis made using the “window” clusterisation method.

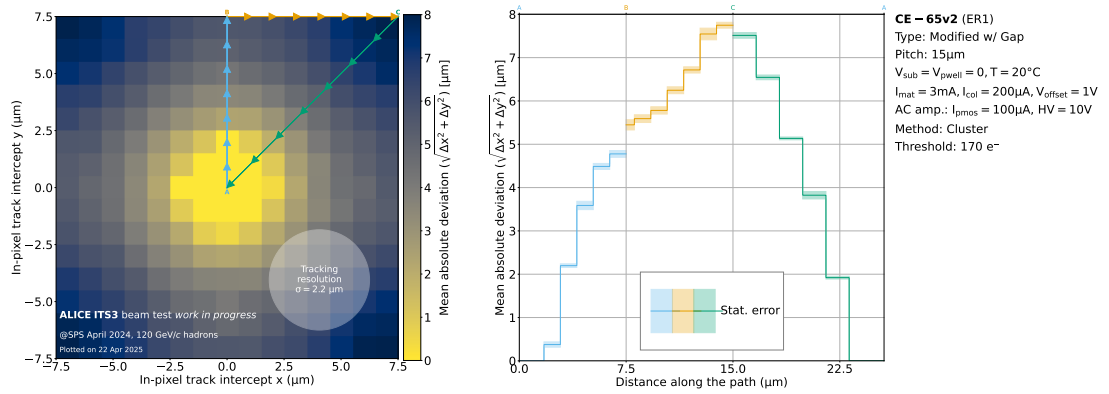


Figure 6.22: In-pixel resolution of Modified with Gap process sensor with 15 μm pitch size. Analysis made using the “cluster” clusterisation method.

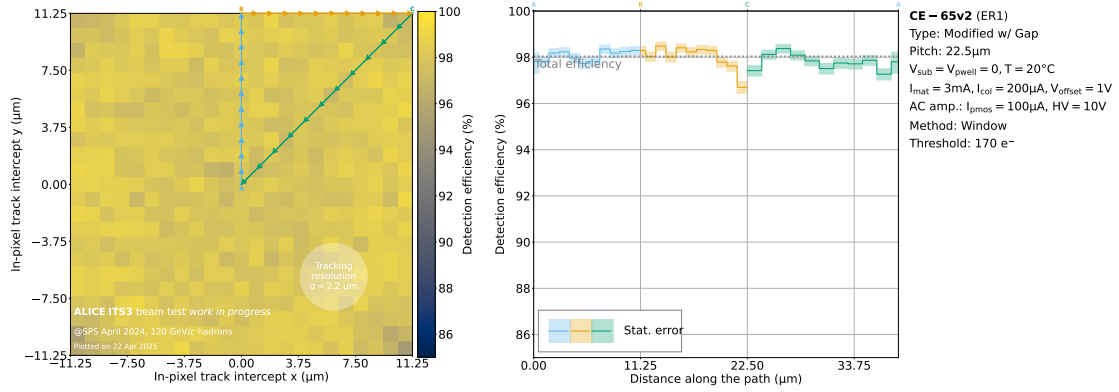


Figure 6.23: In-pixel efficiency of Modified with Gap process sensor with 22.5 μm pitch size. Analysis made using the “window” clusterisation method.

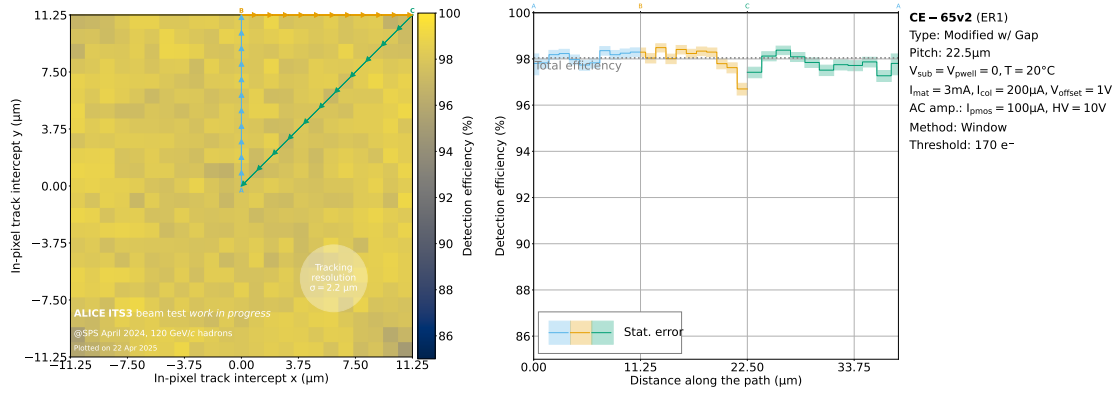


Figure 6.24: In-pixel efficiency of Modified with Gap process sensor with 22.5 μm pitch size. Analysis made using the “cluster” clusterisation method.

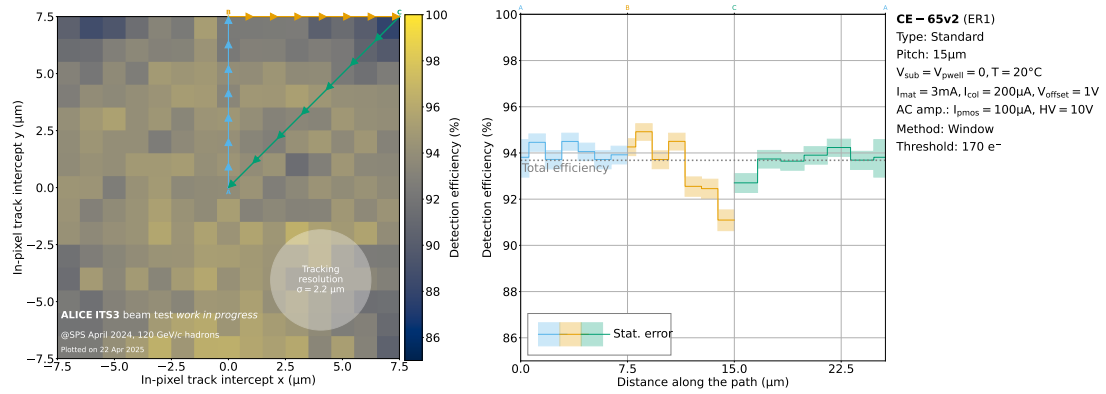


Figure 6.25: In-pixel efficiency of Standard process sensor with 15 μm pitch size. Analysis made using the “window” clusterisation method.

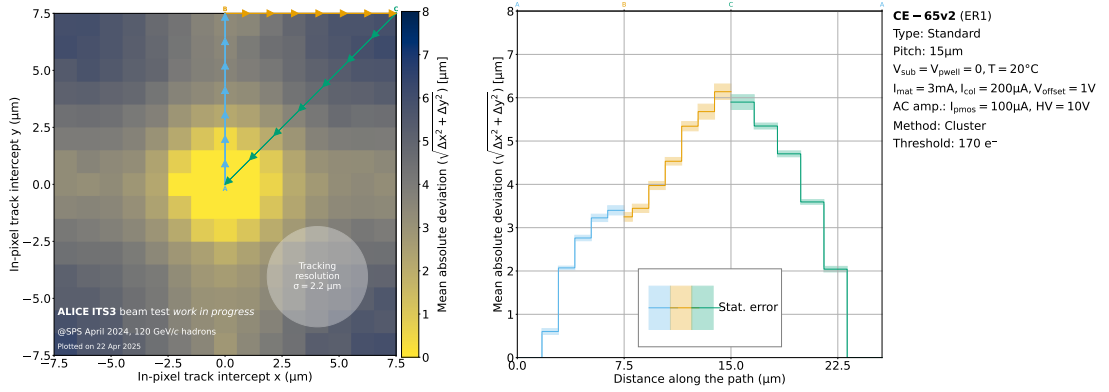


Figure 6.26: In-pixel resolution of Standard process sensor with 15 μm pitch size. Analysis made using the “cluster” clusterisation method.

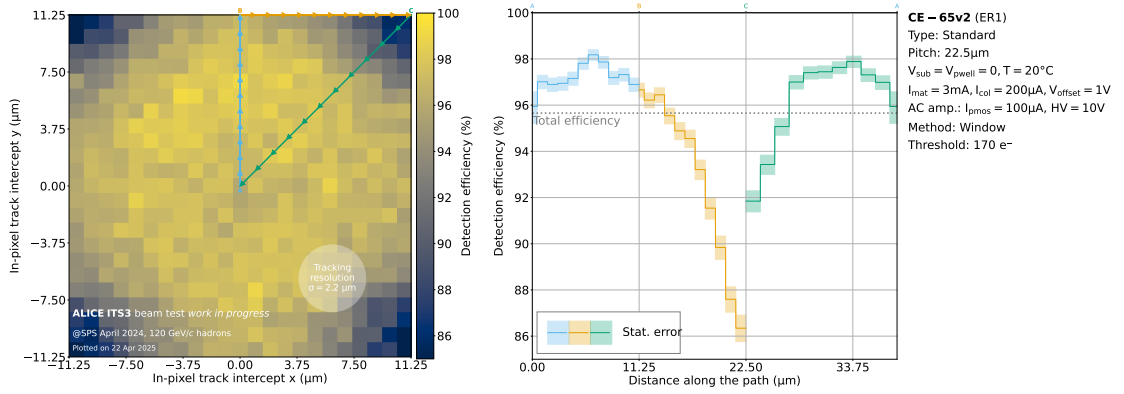


Figure 6.27: In-pixel efficiency of Standard process sensor with 22.5 μm pitch size. Analysis made using the “window” clusterisation method.

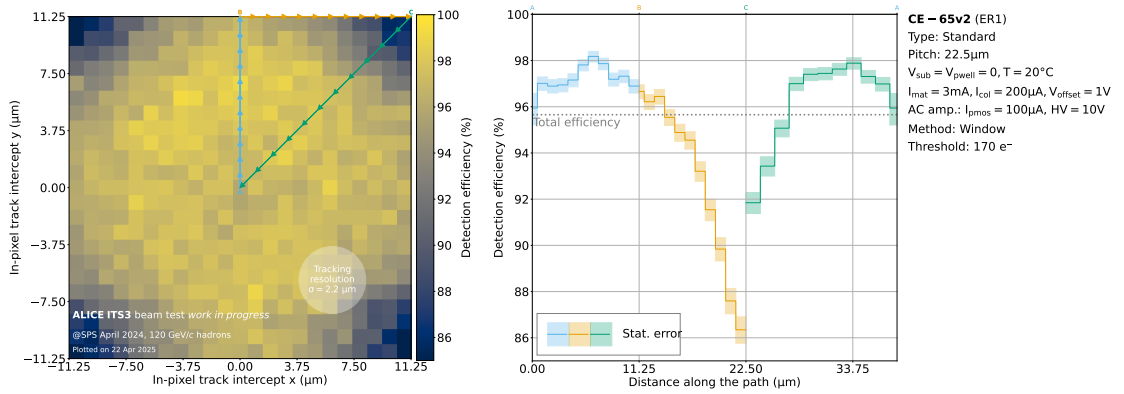


Figure 6.28: In-pixel efficiency of Standard process sensor with 22.5 μm pitch size. Analysis made using the “cluster” clusterisation method.